HU ISSN 2063-6792

MATERIALS SCIENCE AND ENGINEERING

A Publication of the University of Miskolc

Volume 40, Number 1 (2015)

Miskolc University Press
2015

Editor Board:

Chair: Prof. Dr. Árpád Bence Palotás

Secretary: Dr. Ágnes Wopera

Members:

Prof. Dr. Eric G. Eddings
Dr. György Fegyverneki
Prof. Dr. Zoltán Gácsi
Dr. László Gömze
Prof. Dr. C. Hakan Gür
Prof. Dr. Tamás Kékesi
Dr. János Lakatos
Dr. Valéria Mertinger
Prof. Dr. András Roósz
Dr. Judit Sóvágó
Dr. Tamás Szabó
Dr. Katalin Szemmelveisz

Editors: Dr. Ágnes Wopera
Gábor Nagy

CONTENTS

Materials Science and Engineering, Volume 40, No. 1 (2015) pp. 5–16.

FORMATION OF TARS IN THE TDA-TDI SYNTHESIS AND EXPERIMENTAL STUDY OF ITS REMOVAL IN THE TDI RECOVERY PROCESSES

JÓZSEF ÁBRAHÁM[1]–MIKLÓS MAGYARI[2]–JÁNOS LAKATOS[3]

Based on experimental investigations of toluene-diamine (TDA) and toluene-diisocyanate (TDI) synthesis as well as TDI distillation in the TDI recovery processes theoretical study of chemical reactions of tar formation was considered. Summarizing our theoretical study, we conclude that tars formation chemical reactions in TDA and TDI synthesis are unavoidable by-product formation reactions, which have large influence on realization of industrial technology of TDA and TDI manufacturing. Vacuum distillation was used for the TDI recovery from the TDI-TAR mixture and the chemical reactions, the complex process of decomposition and phase transformation of TAR-TDI mixture were tested. The effect of different factors as presence of residues of catalyst in the feed material, ingress of oxygen and water into the process chamber of TDI recovery equipment also were considered.

Keywords:formation of tars, chemical reactions, removal of tars, phase transformation, oligomer formation, polymerization, decomposition

Introduction

In our former investigations we have investigated recovery technology of toluene-diamine (TDA) content of TDA-tar mixture and metod of disposal of TDA-tar [1], as well as mixability of TDA-tar and ortho-toluene-diamin (OTDA) liquid streams [2]. In the present study based on experimental investigations of TDA-tars formation as byproduct of TDA synthesis and phosgenation reactions of TDA with formation of toluene diisocyanate (TDI) in the synthesis and TDI recovery processes, theoretical study of chemical reactions of tar formation, and tars removal as well as study of physical-chemical processes were performed. We describe the TDA-tars formation reactions during TDA synthesis, as well as TDI-tars formation during TDA phosgenation step of TDI synthesis in the present study.

1. TDA tars formation as byproduct of TDA synthesis

1.1.Formation of pre-tars

During toluene-diamine(TDA) synthesis by hydrogenation of dinitro toluene (DNT) TDA is produced, but simultaneously side reactions take place with formation of so-called pre-tars [1]:

[1] University of Miskolc, Institute of Chemistry
Miskolc-Egyetemváros 3515, Hungary
abraham.jozsef@upcmail.hu
[2] BorsodChem Zrt.
Kazincbarcika 3700, Hungary
miklos.magyari@borsodchem.eu
[3] University of Miskolc, Institute of Chemistry
Miskolc-Egyetemváros 3515, Hungary
mtasotak@uni-miskolc.hu

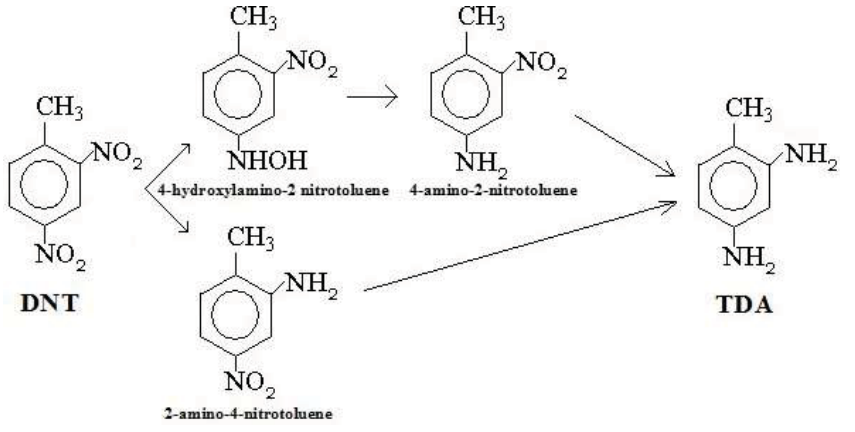

(1)

Figure 1. TDA pre TAR-s formation during the TDA productions

Components yet unconverted to TDA can be considered as the so-called pre-tars. If these components remain adsorbed on the surface of hydrogenation catalyst for too long time they can react to each other to form dimers. During dimerization reactions azoxy-, azo-, and hydrazo-benzene derivatives are formed. Approx. 20% of tar components are produced by these reactions. Different combination of pre-tars will produce TDA-tars as it is illustrated below:

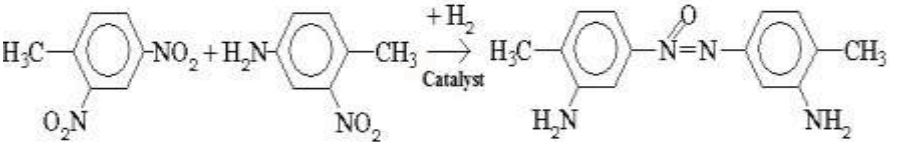

(2)

Pre-tars TDA-tar (2,2'-diamino-4,4'azoxytoluene)

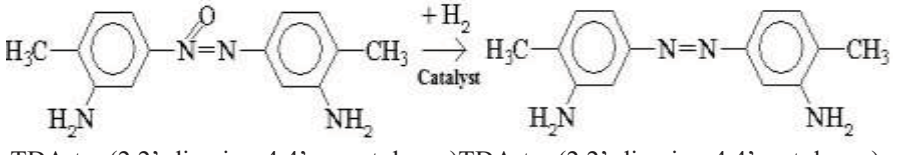

(3)

TDA-tar (2,2'-diamino-4,4'azoxytoluene)TDA-tar (2,2'-diamino-4,4'azotoluene)

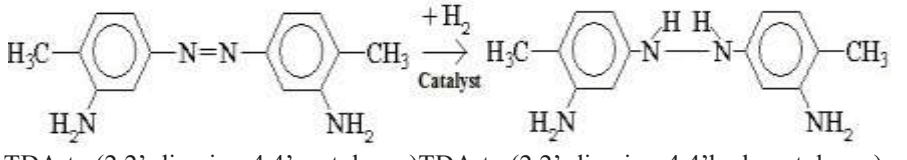

(4)

TDA-tar(2,2'-diamino-4,4'azotoluene)TDA-tar(2,2'-diamino-4,4'hydrazotoluene)

Figure 2. TDA TAR formation reactions

1.2. TDA-tar formation from ortho-isomers

Micro zones of DNT saturated catalyst surface provide oxidative environment so the ortho isomers can react to form diamino-dimethyl-phenazin derivatives giving 80% of TDA-tar components (the aromatic ring can also be hydrogenated) [1]:

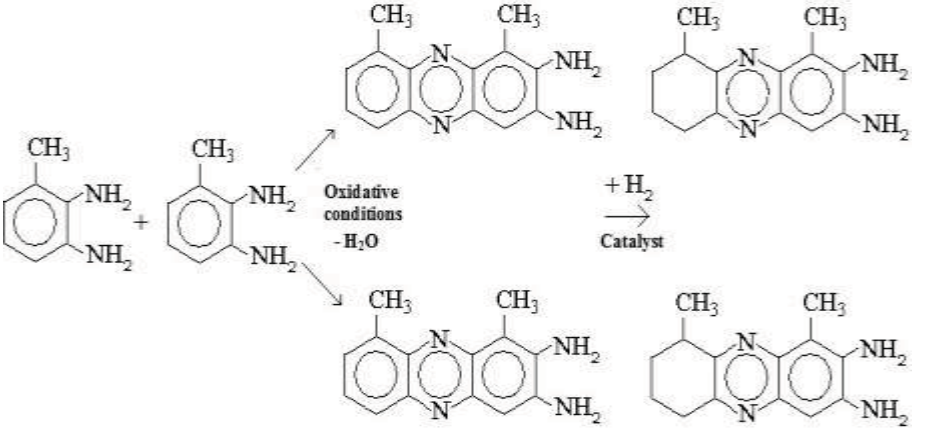

(5)

2,3 toluene-diamin (ortho-isomer) diamino-dimethyl-phenazin TAR components

Figure 3. TDA TAR formation from orto isomers of TDA

2. Phosgenation reactions of TDA with formation of TDI

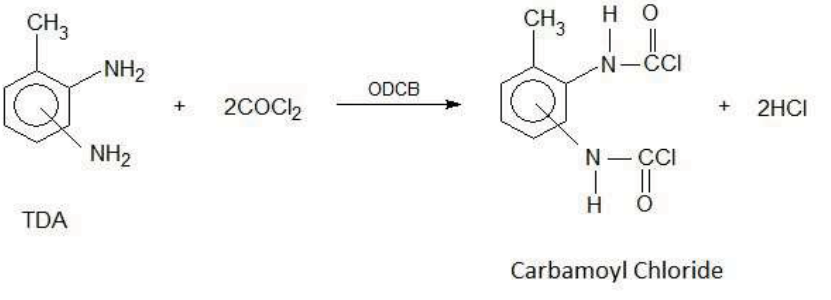

(6)

TDA – 2,4- and 2,6- toluene-diamine (metha-isomers)

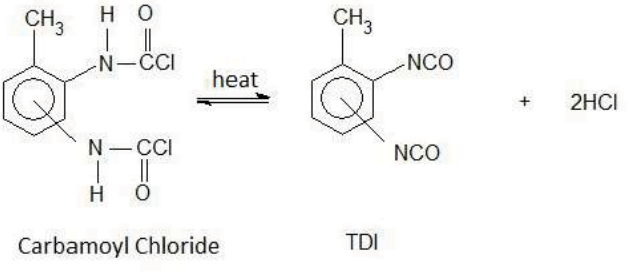

(7)

TDI – 2,4- and 2,6- toluene diisocyanate

Figure 4. TDI formation in the phosgenation reaction

3. Reactions of formation of TDI-tar byproducts

During the phosgenation of toluenediamine to toluene diisocyanate followed by distillation of TDI, there are formed relatively high molecular weight by-products containing uretdione, isocyanurate, carbodiimide, uretone imine, urea and/or biuret groups, which will remain in distillation residue as tar byproducts [3,4].

Uretdione (TDI-dimer) formation:

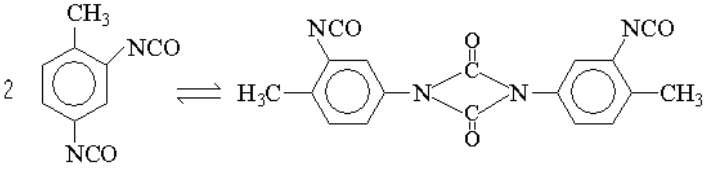

TDI Uretdione (TDI-dimer) (8)

Carbodiimide formation:

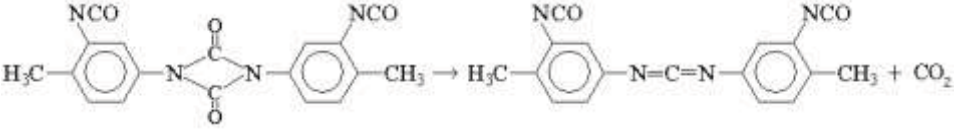

Uretdione (TDI-dimer) Carbodiimide (9)

Urea formation:

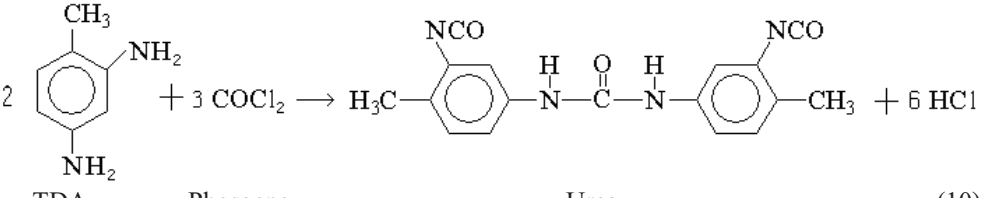

TDA Phosgene Urea (10)

During the phosgenation traces of water in the TDA can result in urea derivatives in two steps:

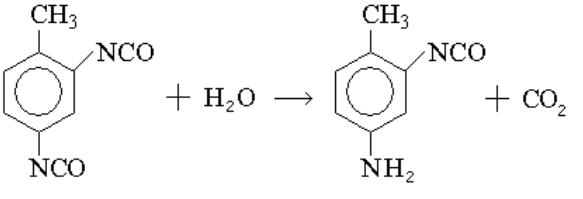

TDI Toluene-amino-isocyanate (TAI) (11)

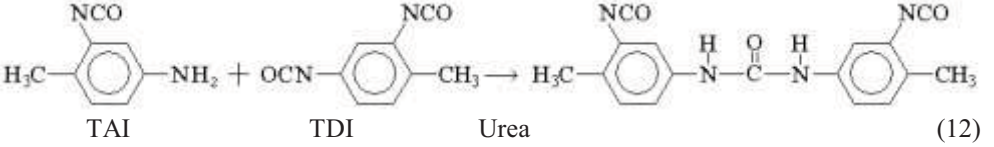

TAI TDI Urea (12)

Uretonimine formation:

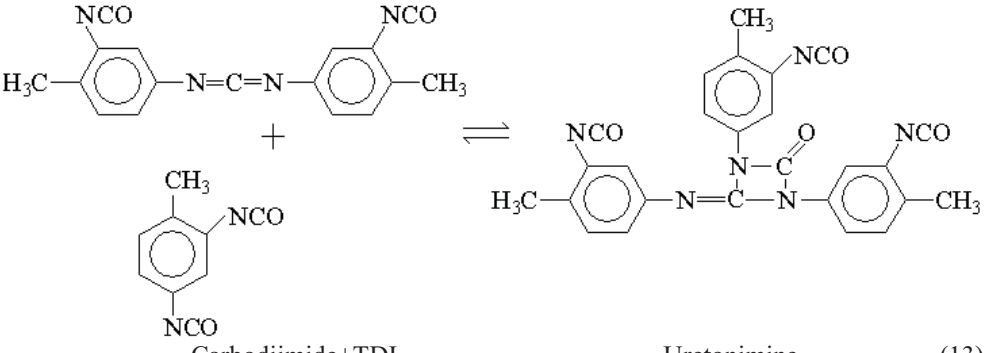

Carbodiimide+TDI Uretonimine (13)

Biuret formation:

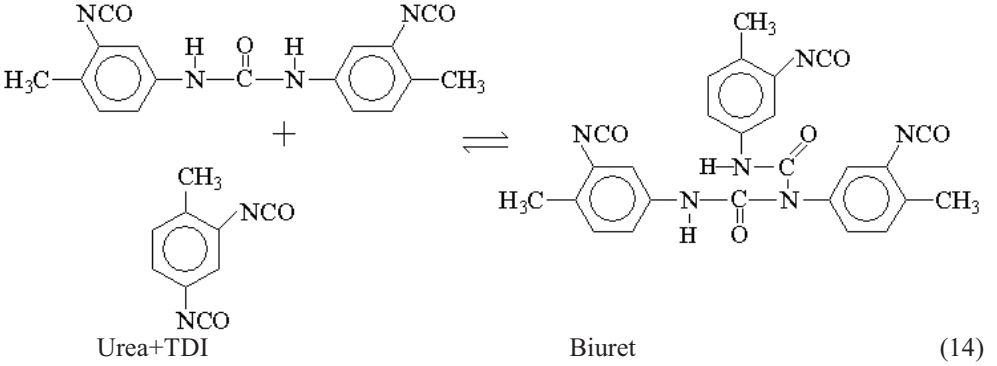

Urea+TDI Biuret (14)

Isocyanurate formation:

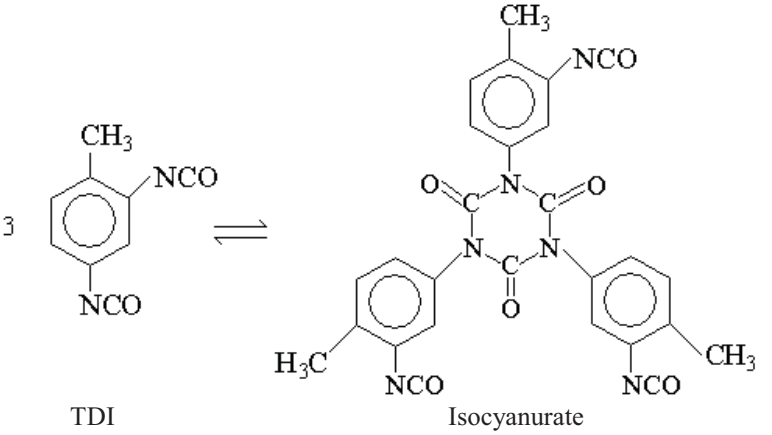

TDI Isocyanurate (15)

Figure 5. TDI TAR-s as byproduct formation in the phosgenation reaction

Depending upon the ortho-toluene-diamin (OTDA) content of the meta-toluene-diamin (MTDA) starting material, there can also be formed methylbenzimidazoles during phosgenation and with time, they are biuretized with the free isocyanate groups present, with an accompanying formation of cross-linked products.

Methyl-benzimidazole formation:

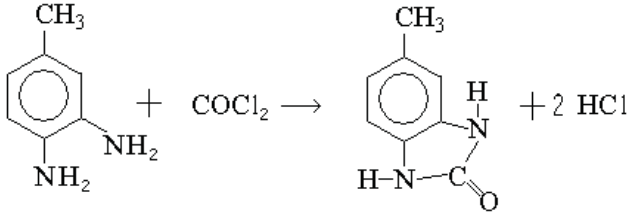

Ortho-TDA Methyl-benzimidazole (16)

Biuret formation:

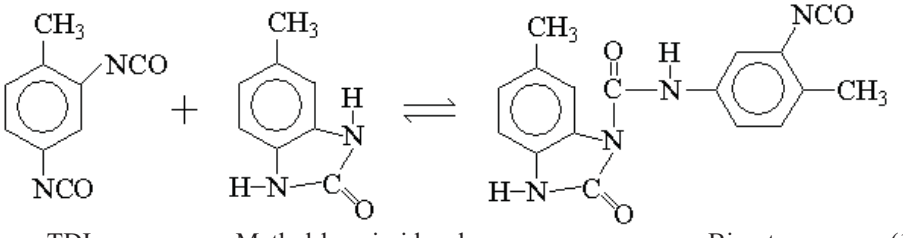

TDI Methyl-benzimidazole Biuret (17)

Figure 6. Reaction scheme of biuret formation

During phosgenation the TDA-tar components as azoxy-, azo-, hydroazo-benzene and diamino-dimethyl-phenazine derivatives (2), (3), (4) and (5) form two- or three ringed "heavy" diisocyanates which will remain in distillation residue as tar byproducts.

$$H_2N\text{-}R\text{-}NH_2 + 2\ COCl_2 \rightarrow \quad OCN\text{-}R\text{-}NCO + 4\ HCl \tag{18}$$

Where "R" is the azoxy-, azo-, hydroazo-benzene and diamino-dimethyl-phenazine radical.

4. Main tar formation reactions of isocyanates

According to studies performed by L. Cotarca, H. Eckert main phosgenation reactions and functional groups that can be formed were summarized [4], which we further developed with formation of tars by-products as it is shown in the scheme, presented in Figure 5.

In our investigations, we were studyingformation of relatively high molecular weight by-products in the TDI synthesis, containing uretdione, isocyanurate, carbodiimide, uretone-imine, urea and/or biuret groups, which will remain in distillation residue as tar byproducts, and furthermore we investigated reactions taking place in the TDI-tar removal and TDI-recovery process from distillation residues.

4.1. Reaction of isocyanates with urea groups

Similarly to allophanate formation, the –NH groups of urea react with isocyanates, to generate biuret, see reaction equation (14).

Also similarly to allophanate formation, the reaction between urea and isocyanates is an equilibrium reaction and needs higher temperatures too (> 110 ºC).

The formation of allophenates and biurets in the TDI recovery process, where excess of isocyanate is available, is in fact a source of crosslinking of TDI-tars.

4.2. Reactions of isocyanates with urethanes

Urethane groups may be considered hydrogen active compounds, due to the hydrogen atom linked to the nitrogen atom. By reaction of an isocyanate with urethane group an allophanate is formed:

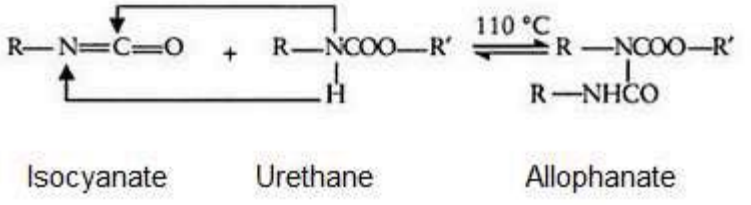

(19)

Figure 7. Reaction scheme of allophanate formation

Due to the electron withdrawing effect of the carbonyl groups, the urethane group has a much lower reactivity than the aminic –N-H groups; and in order to promote the allophanate formation higher temperatures are necessary: greater than 110 ºC. Figure 7. It is important to mention that the allophanate formation is a reversible reaction [6].

4.3. Reactions of Carbodiimid formations

Carbodiimide can react with another TDI or CDI to form bigger CDI molecule (carbodiimide oligomer / polymer /p-CDI/) while CO_2 is released.

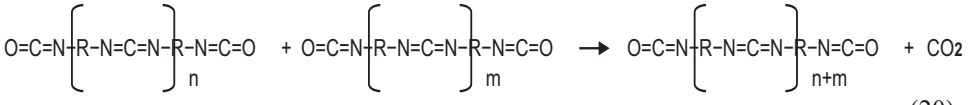

(20)

where: n, m = 0, 1, 2,…."∞"

R = toluylene radical: 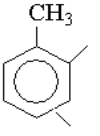

Figure 8. Reaction scheme of carbodiimide formation

This reaction Figure 8 is the main process resulting in the final solid tar powder in the TDI recovery process.

Summarizing our theoretical study, we conclude that tars formation chemical reactions in TDA and TDI synthesis are unavoidable by-product formation reactions, which have large influence on realization of industrial technology of TDA and TDI manufacturing.

The main TDI tar formation process in TDI synthesis is the phosgenation of TDA-tar components: as nitroso-, azo-, hydroazo- and diamino-dimethyl-phenazine derivatives (2), (3), (4) and (5) form two- or three ringed "heavy" diisocyanates. This is followed by

formation of relatively highmolecular weightby-products in the TDI synthesis, containing uretdione, isocyanurate, carbodiimide, uretone-imine, urea and/or biuret groups, which will remain in distillation residue as tar byproducts.

5. Experimental Part

In our investigations, we focused on the TDI-tar removal during the TDI-recovery process from TDI distillation residues.

5.1. TDI-tar concentrating and removal by evaporation of TDI with Continuous Vacuum Evaporation/Drying system

The experimental study has been performed on LIST AP6300 and AP4000 Type Continuous Vacuum Evaporation/Drying equipment of BorsodChem's TDI Plants.

The feed stream of the TDI distillation residue has usually a temperature of 150–160 °C and composition of 45–55 m/m% TDI and 55–45 m/m% tar. The operating pressure in continuous vacuum evaporator/dryer lies in the 20–25 mbar abs range. The operating temperatures of five zones of vacuum evaporator/dryer increases continuously from 170 °C up to 230–245 °C. Under these operating conditions, a flash evaporation takes place as soon as the stream of the distillation residue enters into the process chamber of the vacuum evaporator/dryer. Further TDI evaporation and subsequent drying take place along the vacuum evaporator/dryer. During the course of the evaporation/drying process the consistency of the distillation residue changes from liquid, through a highly viscous, paste phase to a final free flowing granular residue material. This change of phase consistency is shown in Figure 10. The vacuum evaporator/dryer is heated by thermal oil at the temperature of 240–250 °C. The TDI vapor is withdrawn through the heated dome, which is mounted on top of the vacuum evaporator/dryer. The final free flowing granular dry TAR residue is continuously discharged into a vacuum tight lock system.

The free-flowing granular final residue remaining after TDI evaporation has a TDI content less than or equal to 0.5 m/m%. Main processes taking place along with the continuous vacuum evaporation/drying equipment are shown in Figure 9, the equipment characteristics are given at Table1.

TDI Recovery by continuous vacuum evaporation/drying

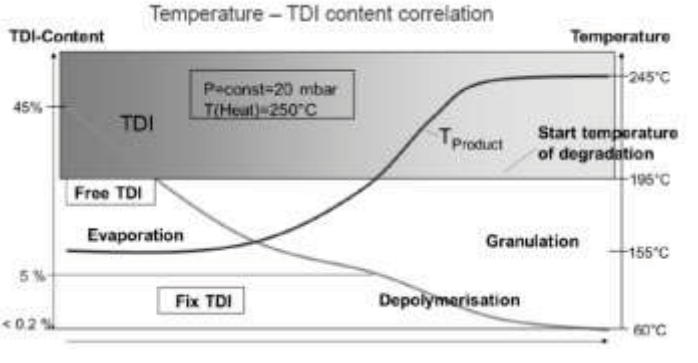

Processes taking place along with the continuous vacuum evaporation/ drying equipment

Figure 9. Main processes of TDI-tar concentrating and removal by evaporation of TDI with Continuous Vacuum Evaporation/Drying system

The blue curvein Figure 9 shows change of TDI content of product as result of evaporation from 45m/m% to less than 0.2m/m% and formation of final free flowing granular dry tar residue.

The red curve shows change of product temperature from 160 °C to 245 °C along with the continuous vacuum evaporation/drying equipment at constant pressure of 20 mbar (abs) and constant heating oil temperature of 250 °C.

Table 1

Process requirements and equipment characteristics for TDI Recovery by continuous vacuum evaporation/drying

Process requirement	Equipment characteristics
During evaporation, the liquid distillation residue passes through a rubbery, viscous, pasty phase with a tendency to foam.	Robust construction, high torque to overcome the viscous phase, large vapor volume, effective foam breaking by agitator action with droplet disengagement space above the surface.
If the final TDI content is less than 17%, then the residue solidifies, and forms a hard crust.	Good self-cleaning of heating surfaces and efficient grinding action.
High level of containment and safety due to toxicity of TDI.	Enclosed, contained construction.
Low personnel requirement.	Continuous automated operation.
Prevention of decomposition reactions.	Operation in vacuum and narrow residence time distribution.

LIST AP6300 and AP4000 Type Continuous Vacuum Evaporation/Drying equipment are well fulfilling process requirements summarized in Table 1.

5.2. Chemical reactions and phase transformation, decomposition complex processes of tar removal in the TDI recovery process

5.2.1. Phase transformation of TDI tars in TDI recovery equipment

Transformation of liquid tars into viscose phase (see Figure 10) and then into free flowing solid granular phase takes place as result of evaporation of free TDI content of liquid tars. Simultaneously, reactions of isocyanate with TDI-tar components occur with formation of viscous, cross-linked products,which contain high molecular weight by-products, such as uretdione, isocyanurate, carbodiimide, uretone imine, urea and/or biuret groups (see former reactions Figures 7–8).However, these condensation reactions take place at moderated temperature (between 100–200ºC) in the liquid phase.

In the final step of the TDI recovery process at the temperature above 200 ºC under vacuum, the evaporation (free TDI and small tar molecules evaporate) and gas releasing decomposition reactions are dominating. Uretdione-, uretonimine- and biuret molecules decompose releasing TDI and even the carbodiimide polymerization is going on releasing CO_2 and resulting in the final solid tar powder (see equation Figure 8).

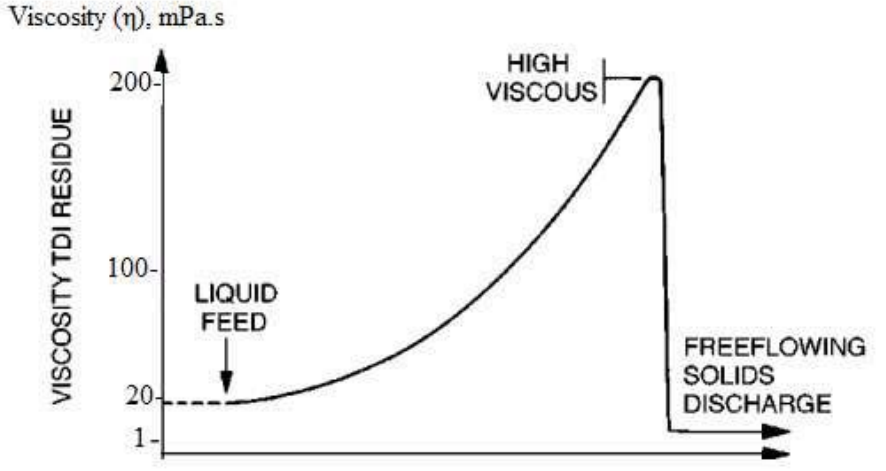

Viscosity profile of TDI distillation residue vs. evaporator-dryer length

Figure 10. Phase transformation of TDI tars in TDI recovery equipment

TDI-dimer decomposes and evaporates as "pure TDI", however the molecule "remembers" that it was a "dimer" so it immediately forms a new dimer when condensates in the recovered TDI. Figure 11.

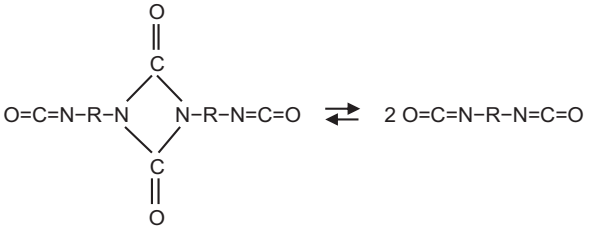

(21)

TDI-dimer **TDI**

Where:

R = toluylene radical: 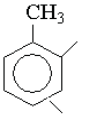

Figure 11. Dimerization of TDI

Uretonimines decompose releasing TDI.

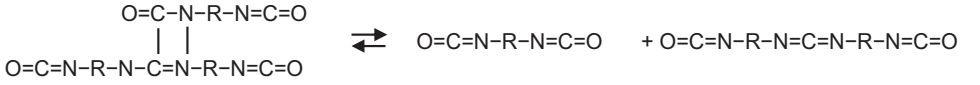

(22)

Uretonimine **TDI** Carbodiimide (CDI)

Figure 12. Decomposition of TAR- components during distillation process

Carbodiimide can react with another TDI or CDI to form bigger CDI molecule (carbodiimideolygomer / polymer /p-CDI/) while CO_2 is released, as shown in equation (21). According to our experiences, this reaction is the main process resulting in the final solid tar powder in TDI recovery process.

Biurets also decompose releasing TDI.

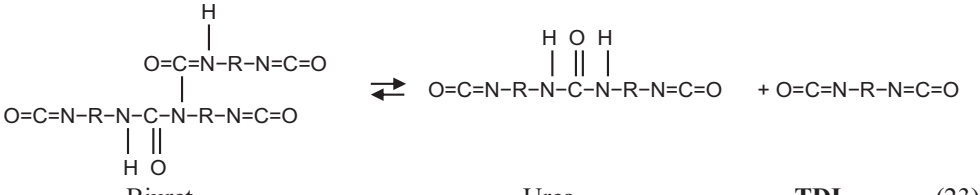

Biuret Urea **TDI** (23)

Figure 13. Decomposition of TAR-components during distillation process

5.2.2. Effects of residues of catalyst, oxygen and water on TDI recovery process

In our investigations, we were studying based on experiences gained in operation of continuous vacuum evaporation/drying TDI recovery process, effect of various process disturbance factors, such as presence of residues of catalyst in the feed material, or ingress of oxygen and water to the process chamber of TDI recovery equipment and arrived to the following conclusions:

- Residues of catalyst can cause polymerization reaction, with generation of heat, which will result in increase of zone temperatures of TDI recovery equipment.
- Ingress of oxygen can cause decomposition reaction with generation of CO_2, which will cause foaming problem in the TDI recovery equipment.
- Ingress of water can cause decomposition reaction with generation of CO_2, which will cause foaming problem in the TDI recovery equipment.

Conclusions

Summarizing our theoretical study, we conclude that tars formation chemical reactions in TDA and TDI synthesis are unavoidable by-product formation reactions, which have large influence on realization of industrial technology of TDA and TDI manufacturing. In this study, we systematically reviewed most important chemical reaction steps of formation of pre-tars, TDA-tar formation from ortho-isomers, phosgenation reactions of TDA with formation of TDI, reactions of formation of TDI-tar byproducts and further developed main

phosgenation reactions with formation of tar by-products, discussed reaction of isocyanates with urea groups, and reactions of carbodiimid formation.

Furthermore we studied chemical reactions and phase transformation, decomposition complex processes of tar removal in the TDI recovery process. It was discussed the effect of various process disturbance factors, such as presence of residues of catalyst in the feed material, ingress of oxygen and water into the process chamber of TDI recovery equipment, with analysis of background chemical processes of phase transformation of TDI-tars in TDI recovery equipment.

Acknowledgement

The research work presented in this paper based on the results achieved within the TÁMOP-4.2.1.B-10/2/KONV-2010-0001 project and carried out as part of the TÁMOP-4.2.2.A-11/1/KONV-2012-0019 project in the framework of the New Széchenyi Plan. The realization of this project is supported by the European Union, and co-financed by the European Social Fund.

References

[1] Ábrahám József–Magyari Miklós–Rácz Lajos–Hutkainé Göndör Zsuzsanna–Lakatos János: Laboratóriumi és félüzemi kísérletek TDA-TAR-elegyTDA-tartalma visszanyerési technológiájának és a TAR ártalmatlanítási módszerének kifejlesztéséhez. *Miskolci Egyetem Közleményei. Anyagmérnöki Tudományok,* Vol. 38, 1, 2013, 7–18.

[2] Hutkainé Göndör Zsuzsanna–Ábrahám József–Rácz Lajos–Magyari Miklós–Lakatos János: TDA-TAR és OTDA folyadékáramok elegyíthetőségének vizsgálata. *Miskolci Egyetem Közleményei. Anyagmérnöki Tudományok,* Vol. 37, 1, 2012, 147–152.

[3] Lengyel Attila–Mogyoródy Ferenc–Ábrahám József–Magyari Miklós–Fehér Tamás: Meta-toluilén-diamin (TDA)-kátrány (TAR) koncentrátum előállítása vákuum desztillációval, a koncentrátum viszkozitás hőmérséklet és koncentráció függésének modellezése. *Miskolci Egyetem Közleményei – 2. sorozat, Anyag- és Kohómérnöki Tudományok,* Vol. 35, 1, 2010, 27–38.

[4] Cotarca, L.–Eckert, H.: *A Phosgenations – Handbook.* WILEY-VCH Verlag GmbH & Co. KGaA, Weinheim, 2003.

[5] Ulrich, Henri: *Chemistry and Technology of Carbodiimides.* WILEY-VCH Verlag GmbH & Co. KGaA, Weinheim, 2007.

[6] Ionescu, Mihail: *Chemistry and Technology of Polyols for Polyurethanes, Rapra Technology*. 2005.

[7] *ASTM D3432-89: Standard Test Method for Unreacted Toluene Diisocyanates in Urethane Prepolymers and Coating Solutions by Gas Chromatography.* ASTM International, West Conshohocken, PA, 1996.

Materials Science and Engineering, Volume 40, No. 1 (2015) pp. 17–25.

DETERMINATION OF TDA-TAR AND TDI-TAR CONTENT AND QUANTITY IN TDI SYNTHESIS

MAGYARI MIKLÓS[1]–ÁBRAHÁM JÓZSEF[2]–LAKATOS JÁNOS[3]

Based on experimental investigations into toluene-diamine (TDA) and toluene-diisocyanate (TDI) synthesis and on theoretical considerations about the chemical reactions of tar formation, a gas chromatographic method is described in the way it was used for the determination of TDA-tar and TDI-tar content produced from the synthesis process. Some practical remarks and suggestions are provided for the modification of the ASTM Standard Test Method' for unreacted Toluene diisocyanates inprepolymers and coating solutions', using gas chromatography to quantify TDA- and TDI-tars.
Keywords: formation of tars, chemical reactions, oligomer formation, polymerization, decomposition, gas chromatography

Introduction

In our former publications [1–3], the potential recovery of toluene-diamine (TDA) from TDA-tar mixtures and the method of tar disposal has been discussed, as well as the miscibility of TDA-tar with ortho-toluene-diamine (OTDA) liquid streams. TDA-tars are obtained as a byproduct of TDA synthesis. In this paper, first the reaction scheme of the TDA-tar formation process is analyzed. In the subsequent steps, the phosgenation reactions of TDA are considered, leading to the formation of toluene diisocyanate (TDI). The aim of this study is to establish a reliable and applicable method for the determination of tar contentin the reaction mixtures.

Besides the main product that can be TDA or TDI, the byproduct in the reaction mixture is considered as tar. The principle of analysis is based on the determination of the TDA or TDI content of the reacted sample, with the tar content obtained as the difference. In order to better understand the chemistry of tars, the reaction schemes below help defining the chemical forms of the molecules that are formed stepwise in a series of complex reactions and appear as byproducts by the end of the synthesis process. Using these reaction schemes, it is possible to identify those different compounds the cumulative data of which can be quantified as the total amount of tar.

[1] BorsodChem Zrt.
Kazincbarcika 3700, Hungary
miklos.magyari@borsodchem.eu
[2] University of Miskolc, Institute of Chemistry
Miskolc-Egyetemváros 3515, Hungary
abraham.jozsef@upcmail.hu
[3] University of Miskolc, Institute of Chemistry
Miskolc-Egyetemváros 3515, Hungary
mtasotak@uni-miskolc.hu

1. TDA tars formation reactions

1.1. TDA tars formation as byproduct of TDA synthesis

During dimerization reactions**,**azoxy-, azo-, and hydrazo-benzene derivatives are formed. Approximately 20% of the tar components are produced by these reactions. Different combinations of pre-tars will produce TDA-tars as it is illustrated in Figure 1 below:

1.1. TDA-tar formation from Pre-tars

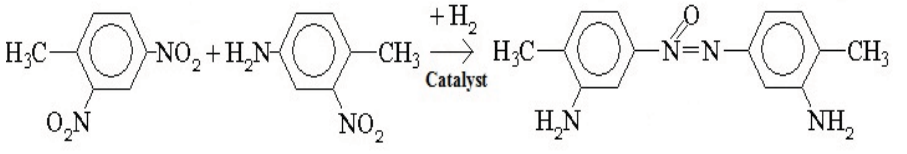

(1)

Pre-tars TDA-tar (2,2'-diamino-4,4'azoxytoluene)

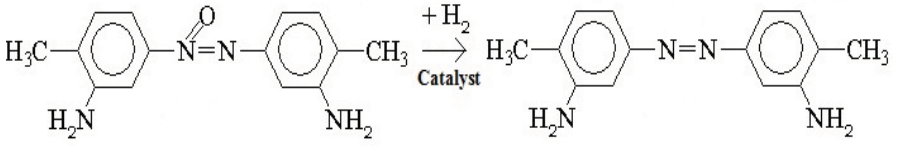

(2)

TDA-tar (2,2'-diamino-4,4'azoxytoluene) TDA-tar(2,2'-diamino-4,4'azotoluene)

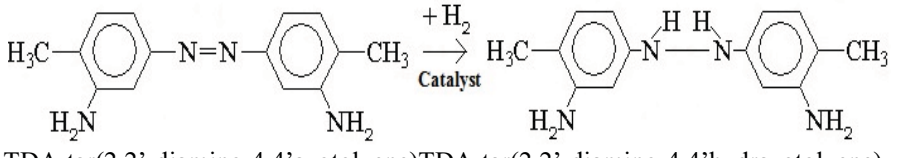

(3)

TDA-tar(2,2'-diamino-4,4'azotoluene)TDA-tar(2,2'-diamino-4,4'hydrazotoluene)

Figure 1. Reaction scheme of TDA-tar formations

1.2. TDA-tar formation from ortho-isomers

80% of the TDA-tar components are formed fromthe reactions of ortho-isomers, and the generated tar components are diamino- dimethyl- phenazin derivatives, respectively [1]:

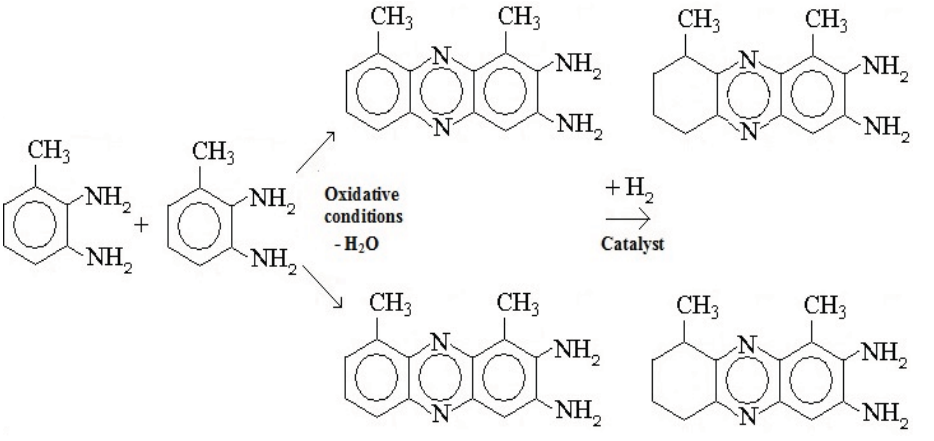

(4)

2,3 toluene-diamin (ortho-isomer) diamino-dimethyl-phenazin TAR components

Figure 2. TDA-tar formation from 2,3 toluene-diamine

1.3. Formation reactions of TDI-tar byproducts

- During the phosgenation of toluenediamine to toluene diisocyanate followed by the distillation of TDI, by-products of relatively high molecular weight are formed containing uretdione, isocyanurate, carbodiimide, uretone imine, urea and biuret groups, which will remain in the distillation residues as tar byproducts [3] [4].
- Depending upon the ortho-toluene-diamine (OTDA) content of the meta- toluene-diamin (MTDA) starting material, methylbenzimidazoles might as well be formed during phosgenation and with time, these are biuretized with the free isocyanate groups present, with an accompanying formation of cross-linked products.
- During phosgenation the TDA-tar components as azoxy-, azo-, hydrazo- and diamino-dimethyl-phenazine derivatives (1), (2), (3) and (4) form two- or three ringed “heavy” diisocyanates which will remain in the distillation residue as tar byproducts.

1.4. Main tar formation reactions of isocyanates

In a research performed by L. Cotarca, H. Eckert [4], the main phosgenation reactions were summarized, together with the description of the functional groups that might be formed during the process. Hereby we present an advanced version of their scheme, which we complementedwith the formation of tar by-products as it is shown in the following Figure (Figure 3).

As seen, the resulting high molecular weight reaction by-products contain uretdione, isocyanurate, carbodiimide, uretone-imine, urea and biuret groups, which will remain in distillation residue as tars.

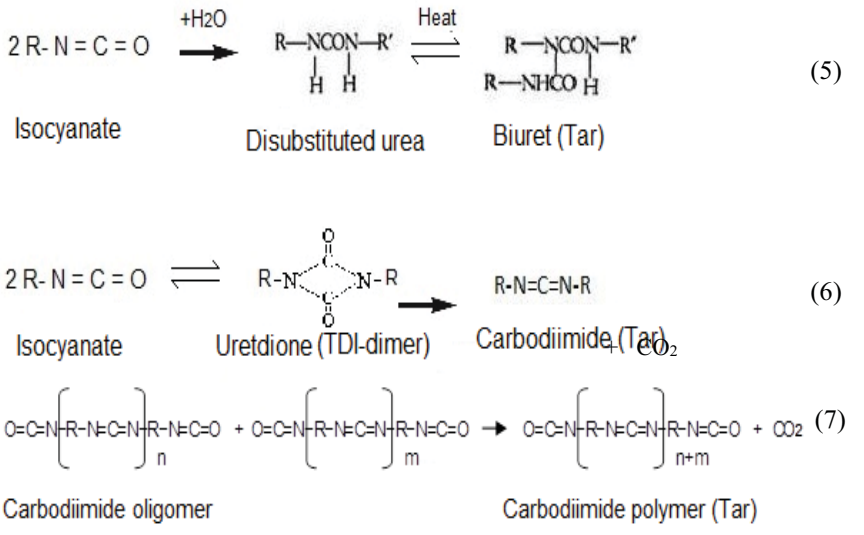

Figure 3. Main reactions of isocyanate-tar by-products formation

Summarizing our theoretical study, we conclude that the chemical reactions which lead to the formation of tar by-products inevitably occur in the TDA and TDI synthesis process and have aconsiderable influence on the large-scale application of TDA and TDI synthesis in industrial manufacturing.

The determination and quantification of TDA-tar and TDI-tar content produced from TDI synthesis was performed by gas chromatographic method, which is described below.

2. Experimental Part

2.1. Determination of TDA-tar and TDI-tar by gas chromatographic method

According to our experiences, the easiest and most reliable way to determine either TDA- or TDI-tars (in high tar-containing TDA or TDI) is the application of a capillary GC method using an internal standard technique.

In this method, we determine the exact concentration of the TDA and TDI isomers ("TDA%" in the case of TDA-TAR mixtures and "TDI%" in the case of TDI-TAR mixtures, respectively) by using an appropriate internal standard compound.

The concentration of the tar components is then calculated as follows: TAR% = 100%–TDA% (in case of TDA-TAR mixtures) and TAR% = 100%–TDI% (in case of TDI-TAR mixtures).

This is a widely used analytical method in gas chromatography in cases when there are "nondetectable" components in the mixtures.

Some TAR components constitutesuchlarge molecules (especially the polymeric carbodiimides in TDI-TAR mixtures) that they cannot be detected by GC (they do not even evaporate in the injector of the GC), therefore, the use of an internal standard method for the determination of componential tar concentration is justified.

With some modification, the international ASTM D3432-89 "Standard Test Method for Unreacted Toluene Diisocyanates in Prepolymers and Coating Solutions by Gas Chromatography" [7] seems suitable for that type of analysis.

Any modern capillary GC instrument with FID detector can be used for this method. Any capillary column that can withstand a final temperature of 300 °C and has the proper resolution range between the internal standard 1,2,4 trichlorobenzene (TCB) and the TDA or TDI peaks can also be used in this method.

High injector temperature (e.g. 300 °C) is rather important in the determination of both TDA-tarand TDI-tar. Given, for example, a crude TDI with high tar content, if the injector temperature is not high enough, part of the free TDI will not be able to evaporate, and the uretdione (TDI-dimer), uretonimines and biurets will not decompose to release TDI. In this case, the tar content will be overestimated (the so-called "recoverable TDI" will be underestimated).

In our investigations, the following gas chromatographic method was applied:

Apparatus:

- Capillary gas chromatograph with flame ionization detector (FID) and auto-injector
- Analytical column of medium polarity (100% dimethyl-polysiloxane stationary phase), dimensions: (30 m x 0.32 mm x 0.1 um),

Reagents:

- Gases for GC: He (4.6) as carrier gas, N_2 (5.0) as auxiliary gas, H_2 (3.8) fuel gas, synthetic air (N_2/O_2: 80/20% v/v) for the flame
- Dried acetone for TDI-tar analysis (analytical grade)
- Methanol for TDA-tar analysis (analytical grade)
- TCB as internal standard (analytical grade)
- TDI-80 product for TDI-tar analysis (analytical grade)
- 2,4 TDA for TDA-tar analysis (analytical grade)

GC operating conditions:

- *Injector*temperature: 300 °C
- Linear Velocity: 40 cm/s
- Split Ratio: 100:1
- *Detector*temperature: 310 °C

Table 1

The GC oven program

Program steps	**Rate [°C/min]**	**Temperature [°C]**	**Hold Time [min]**
0	–	90.0	0.0
1	20.0	220.0	0.0
2	5.0	300	10

Procedure:

For the chromatographic analysis of TDI-tar, 1.0 ± 0.1 g of the sample and 0.5 ± 0.05 g of TCB should be accurately weighed into the 10 ml standard flask and diluted to 10 ml with dried acetone. Proper mixing can be aided with an ultrasonic bath to enhance dissolution.

For TDA-tar analysis, 1.0 ± 0.1 g of the sample and 0.5 ± 0.05 g of TCB should be accurately weighed into the 10 ml standard flask and diluted to 10 ml with methanol. Proper mixing can be aided with an ultrasonic bath to enhance dissolution.

In both cases, about 1.5 ml solution should be poured into the vial with septa (using a syringe filter if the sample has solid impurities!), then put in the rack of the auto injector. Upon injection of 1.0 µl of the respective sample into the device, the gas chromatogram under the conditions given in "*GC operating conditions*" should be recorded.

Calculations:

Calibration: For the calibration of TDI-tar analysis, about 1.0 ± 0.05 g TDI-80 and 0.5 ± 0.05 g TCB should be accurately weighed into the 10 ml standard flask, diluted to 10 ml with dried acetone and mixed well.

For the calibration of TDA-tar, about 1.0 ± 0.05 g 2.4 TDA isomer and 0.5 ± 0.05 g TCB should be accurately weighed into the 10 ml standard flask and diluted to 10 ml with methanol, then mixed well.

About 1.5 ml of either solution should be poured in the vial with septa, then put in the rack of the auto injector.

Upon injection of 1.0 µl of the sample into the device, the gas chromatogram under the conditions given in "*GC operating conditions*" should be recorded.

The response factor (RF) is calculated as follows:

$$RF = (W_i \times A_{TCB}) / (W_{TCB} \times A_i)$$

where:

W_i = mass of TDI-80 (or 2,4 TDA)
W_{TCB} = mass of TCB
A_i = Area of TDI isomer peak(s) (or 2,4 TDA peak)
A_{TCB} = Area of TCB peak

Sample analysis result:

$$TDI\ (or\ TDA)\ (m/m\%) = 100 \times RF \times (W_{TCB} \times A_S) / (W_S \times A_{TCB})$$

where:

TDI (or TDA) (m/m%) = mass percent of the free TDI (or TDA) isomers in the sample
RF = Response factor calculated in the calibration
W_{TCB} = mass of TCB
A_S = Area of TDI (or TDA) isomer peak(s) of the sample
W_S = mass of the sample
A_{TCB} = Area of TCB peak

Although this method can be used either for TDI-tar analysis or TDA-tar analysis but not in the same time.

TDI and TDA are potential reaction partner to each other forming urea derivatives quickly in exothermic reaction. When we change from a TDI-tar to TDA-tar analysis (or vice versa) the syringe of the auto injector must be rinsed thoroughly otherwise traces of TDI will react with the TDA sample causing plugging in the injector. Frequent replacement of the silica wool in the injector liner is also needed in this case.

Example of the determination of TDA-tars by gas chromatographic method

The TDA-content of a high tar-containing TDA sample was determined with the described gas chromatographic method. In the first run, the mixture of a 2,4 TDA isomer and the TCB internal standard was analyzed (Table 2) and the TDA/TCB response factor (RF) was calculated. In the second run, the mixture of the TDA sample and the TCB internal standard was analyzed (Table 3 and Figure 4) and the TDA content of the sample (TDA)(m/m%) was determined.

Table 2

Determination of the TDA/TCB response factor (RF)

Component	**Retention Time (min.)**	**Peak area**	**Component mass (g)**	**Response factor (RF)**
TCB	1.733	3955986	0.4910	0.639534
2,4 TDA isomer	4.285	12439496	0.9874	

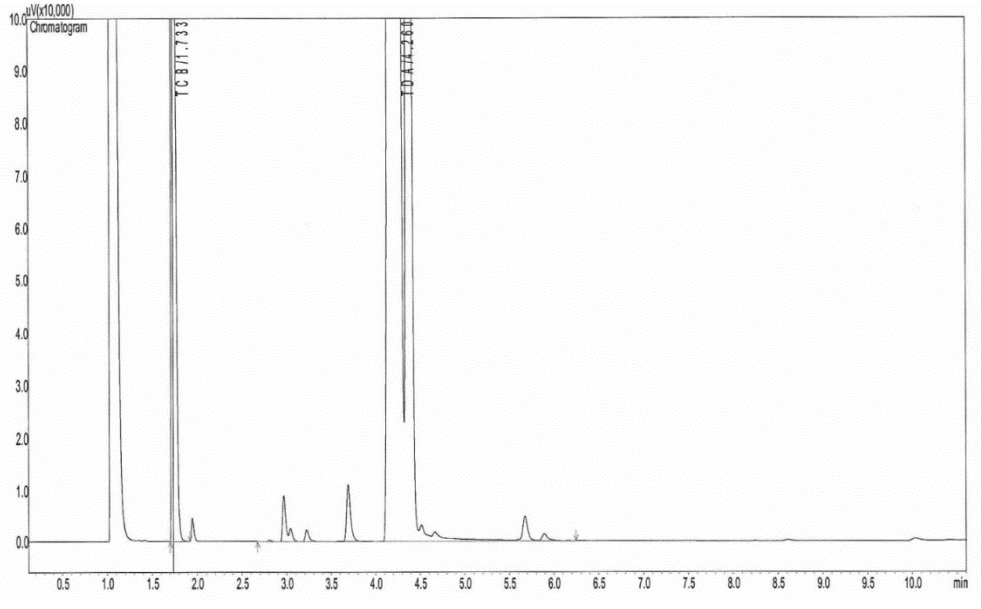

Figure 4. Chromatogram of the TDA sample

Table 3

Determination of the TDA content of the sample

Component	**Retention Time (min.)**	**Peak area**	**Component mass (g)**	**TDA content (m/m%)**
TCB	1.733	4292922	0.5146	71.03
TDA sample	4.260	9357698	1.0100	

Example of determination of TDI-tars by gas chromatographic methods

The TDI content of a crude-TDI sample with high tar-content was determined by this gas chromatographic method.

In the first run, the mixture of the TDI-80 standard and the TCB internal standard was analyzed (Table 4) and the TDI/TCB response factor (RF) was calculated.

Table 4

Determination of the TDI/TCB response factor (RF)

Component	Retention Time (min.)	Peak area	Component mass (g)	Response factor (RF)
TCB	4.58	2067903	0.5192	0.893005
TDI-80 standard	5.57	4656314	1.0440	

In the second run**,** the mixture of the crude-TDI sample and the TCB internal standard was analyzed (Table 5 and Figure 5) and the TDI content of the sample (TDI)(m/m%) was determined.

Table 5

Determination of the TDI content of the crude-TDI sample

Component	Retention Time (min.)	Peak area	Component mass (g)	TDI content (m/m%)
TCB	4.58	1884390	0.5175	39.31
Crude-TDI sample	5.56	1662117	1.0370	

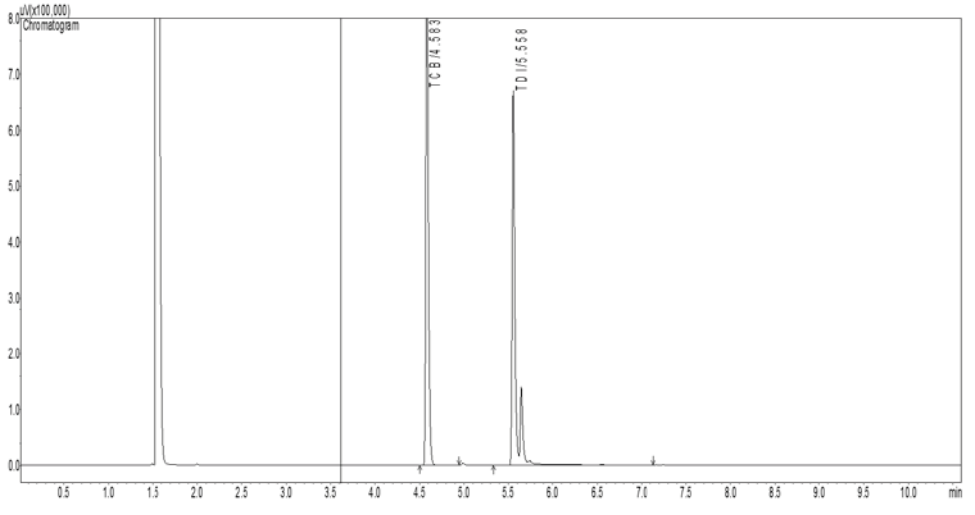

Figure 5. Chromatogram of TDI – TDI-tar mixture

Conclusions

Summarizing our theoretical study, we conclude that the chemical reactions that lead to the formation of tars as by-products in the TDA and TDI synthesis process is unavoidable and have a large influence on theimplementation of TDA and TDI manufacturing as an industrial technology. In this study we summarized the most important chemical reaction steps of TDA-tar formation from pre-tars and ortho-isomers, the formation reactions of TDI-tar byproducts and further developed the main phosgenation reactions by describing the formation of tar by-products.

In the study, we described the determination of TDA-tars and TDI-tars by experimentally validated gas chromatographic method, and suggested some practical modifications to the ASTM Standard Test Method for unreacted Toluene diisocyanates in prepolymers and coating solutions by gas chromatography, to make it applicable for the determination of TDA-tars and TDI-tars.

Acknowledgement

The research work presented in this paper based on the results achieved within the TÁMOP-4.2.1.B-10/2/KONV-2010-0001 project and carried out as part of the TÁMOP-4.2.2.A-11/1/KONV-2012-0019 project in the framework of the New Széchenyi Plan. The realization of this project is supported by the European Union, and co-financed by the European Social Fund.

References

[1] ÁBRAHÁM József–MAGYARI Miklós–RÁCZ Lajos–HUTKAINÉ GÖNDÖR Zsuzsanna–LAKATOS János: Laboratóriumi és félüzemi kísérletek TDA-TAR-elegy TDA-tartalma visszanyerési technológiájának és a TAR ártalmatlanítási módszerének kifejlesztéséhez. *Miskolci Egyetem Közleményei. Anyagmérnöki Tudományok,* Vol. 38, 1, 2013, 7–18.

[2] HUTKAINÉ GÖNDÖR Zsuzsanna–ÁBRAHÁM József–RÁCZ Lajos–MAGYARI Miklós–LAKATOS János: TDA-TAR és OTDA folyadékáramok elegyíthetőségének vizsgálata. *Miskolci Egyetem Közleményei. Anyagmérnöki Tudományok,* Vol. 37, 1, 2012, 147–152.

[3] LENGYEL Attila–MOGYORÓDY Ferenc–ÁBRAHÁM József–MAGYARI Miklós–FEHÉR Tamás: Meta-toluilén-diamin (TDA)-kátrány (TAR) koncentrátum előállítása vákuum desztillációval, a koncentrátum viszkozitás hőmérséklet és koncentráció függésének modellezése. *Miskolci Egyetem Közleményei – 2. sorozat, Anyag- és Kohómérnöki Tudományok,* Vol. 35, 1, 2010, 27–38.

[4] COTARCA, L.–ECKERT, H.: *A Phosgenations – Handbook.* WILEY-VCH Verlag GmbH & Co. KGaA, Weinheim, 2003.

[5] *ASTM D3432-89: Standard Test Method for Unreacted Toluene Diisocyanates in Urethane Prepolymers and Coating Solutions by Gas Chromatography.* ASTM International, West Conshohocken, PA, 1996.

Materials Science and Engineering, Volume 40, No. 1 (2015) pp.26–32.

METHODS OF COMPOSITE COATING: A REVIEW

ALI AL-AZZAWI[1]–PÉTER BAUMLI[2]

The surfaces of tools exposed to high wear stressesneed coatings with high hardness and wear characteristics, e.g. diamond coating or coating with composites. Wear resistant, high hardness coatings can be prepared by laser technology,by brazing, or by electrochemical or electroless methods in aqueous solution.The results of research on preparations of surface composites are collected in this review.
Keywords: composite materials, laser cladding, laser melt injection, electroless plating, electrochemical coating

Introduction

A lot of engineering components are exposed to high wear stresses, for example drill bits for oil drilling. The failure of these engineering components is initialized from the surface in processes such as wear, corrosion, fatigue or fracture. A coating on the surface can improve the surface properties and decrease the failure rate. Several techniques have been applied to protect the surface of components, such as chemical vapour deposition [1], physical vapour deposition methods [2, 3], laser cladding [4], laser melt injection [5], electroplating composite [6] or electroless plating [7]. Composite coating with refractory ceramic particles can result in good wear resistant properties, similar to CVD or PVD coatings. In the following sections we will focus on the laser methods, brazing and aqueous chemistry methods for producing composite coatings.

1. Composite coating by Laser cladding

Surface composite coating can be produced by the laser cladding method, which is reminiscent of the traditional hardfacing welding. In this process, a laser beam is used as the heat source to melt the hardfacing alloy onto the substrate and the reinforcing particles. Laser cladding provides good metallurgical bonds and minimal dilution, which are hard to achieve by other hardfacing techniques [8].

Laser cladding of composite coating has been developed for its capability of introducing hard particles such as WC [4], TiC [9], SiC [10] and Cr_3C_2 [11] as reinforcements, each of which have very high hardness and good wear resistance. Among the hardfacing alloys, nickel-based alloys are most frequently investigated in recent years owing to their added characteristics of excellent resistance against abrasion and corrosion at higher temperatures [8].

A Cr_3C_2-Ni/(Ni + Cr) composite coatingcan be produced by the laser cladding method [11, 12]. The hardness of the Ni or N-B coating is improved by adding Cr_3C_2 phase into the Ni or Ni-B,owing to the complete dissolution of the Cr_3C_2 particles in the Ni matrix alloy. The dissolution of the Cr_3C_2 can increase the Cr and C concentration in the melted Ni-alloy

[1] University of Miskolc, Institute of Physical Metallurgy, Metalforming and Nanotechnology
Miskolc-Egyetemváros 3515, Hungary
al_azzawwi@uomisan.edu.iq
[2] University of Miskolc, Institute of Physical Metallurgy, Metalforming and Nanotechnology
Miskolc-Egyetemváros 3515, Hungary
peter.baumli@gmail.com

and during the rapid cooling process Cr_7C_3, $Fe_{23}(C, B)_6$ phases can be formed,causingan improvement in the hardness of the coating [11]. The hardness and wear resistance increase as the amount of Cr_3C_2 phase in the coating is increased [13].

Partial dissolution of the reinforcing particles can be observed in the case of a WCp/Ni–Cr–B–Si–C composite [4]. Metastable phases, i.e. α-W_2C, W_2C and η_1-β-M_6C compound, can be formed on the interface of the WC particles. These phases deteriorate the mechanical properties of the composite [4].

The partial dissolution of reinforcing particles has also been observed in a TiC/Ni–Cr–B–Si–C composite on steel. During cooling the dissolved TiC can crystallise on the surface of the undissolved TiC [14]. When using TiC in an Ni-based alloy, an intermetallic phase with Ti cannot be observed [15, 4].

2. Composite coating by laser melt injection

Composite coating can be prepared by Laser Melt Injection (LMI) technology. In this case the surface of the substrate can be melted by laser beam (the depth of the pool is approximately 1 mm), and the solid particles (particle size 10 to 100 μm) can be delivered into this pool by inert gas.

There are disadvantages to this method: the first isthat the solid particles are not wetted sufficiently by the melted alloy. Good wettability is needed for pushing the particles into the melted alloy with low energy, and perfect wettability is required for spontaneous immersion [16, 17]. The other difficulties of the preparation of a composite coating with this method are the large differences indensity between the melted metal and the reinforcing particles and the chemical reaction on the surface of the particles/metal matrix. These difficulties can be solved when the particles are formed in-situ during the cooling of the melted metal. In-situ composite coating has been prepared foran Al_2O_3 particle-reinforced carbon steel surface composite coating [18] or the in-situ production of bulk Fe/TiCp [19].

Of course, not only in-situ but also ex-situ composite layers can be formed by the LMI method. Ex-situ means the reinforcing particles are prepared independently from the LMI process. Various ex-situ composite layers have been prepared by LMI method in the last two decades: i.e., a SiC particle-reinforced composite coating [20, 21], WC particle-reinforced coating on titanium alloys [5, 22],a WC particle composite with Fe matrix [23, 24], or a TiB_2 particle-reinforced surface composite on steel substrate [25].

In the case of the preparation of an ex-situ WC particle-reinforced Fe surface composite,it was observed that the WC particles can be dissolved or can be melted during the LMI process. From the melted or dissolved WC a Fe_3W_3C compound layer can be formed on the top of the surface composite. The same compound layer can be observed on the surface of the undissolved WC particles [23]. It was found that 10 w% WC (particle size 80 μm) is sufficient in the WCp/Duplex Stainless Steel system for a significant (approximately 50%) improvement in the wear properties [24].

3. Composite coating by brazing

When using laser technologies the sample can become deformed due to mechanical stresses, because of the rapid cooling of the melted part and the non-uniform temperature. In order to avoid such high mechanical stresses in the sample, there is growing interest among researchers in composite coating preparation by brazing. High vacuum or an inert gas atmosphere is used in the brazing process, and the whole sample is heated up. In this method the mechanical stresses in the sample can be avoided orreduced.

WC, or diamond particles or other particles with high hardness and wear resistance are used as reinforcing materials in the composite coating. The following reinforcing/matrix materialpairs can be used for composite coating: i.e. WC/NiCrBSi (Co) composite [26, 27] WC TiC-Co/CuZnNi [28], WC-8TiC-3TaC-8Co/Cu-Zn-Ni [29], diamond/Ni-Cr [30], and diamond/Cu composite [31].

A Co-coatedWC particle-reinforced (particle size range 40–70 μm) Ni-based brazing alloy composite coating was made by Lu et al. [27]. In this case the Co-coated WC powder and Ni-Cr-B-Si brazing alloy powder were mixed separately with an organic binder. The surface of the WC particles was covered by Co in various amounts. The mixture of the powders and the binder was usedto prepare belts by rolling. These belts were applied for the brazing. The WC-Co-binder belt was placed on the surface of mild steel, and this was covered by the Ni-based belt.The brazing was carried out in a vacuum furnace. The brazing temperature was 1060 °C and the holding time was 10 min.The Co coating on the WC particles improved the wettability of the particles in the brazing alloy, but during the brazing Co dissolved in the matrix. The dissolved Co can decrease the hardness and wear resistance of the coating.Not only brazing belts but also brazing paste can be made from a powder of the brazing alloy and the reinforcing material using a larger volume of organic binder. The brazing pastes are more suitable for preparing composite brazing coating on the complex surface of engineering components.

Alloys with a lowermelting point, such as Ag-Cu-Ti alloy, can produce composite coating between 820 and 940 °C. A good example of this is the work of Wu et al. [31], in which the development of a diamond particle-reinforced Ag-Cu-Ti matrix composite on Al_2O_3 substrate was studied. They found that a reaction takes place between the diamond particles and the brazing alloy (matrix), as well between the Al_2O_3substrate and brazing alloy; as a result TiC (on the interface of diamond/brazing) and $Ti_3(Cu, Al)_3O$ compounds form (on the interface of Al_2O_3/brazing), ensuring the good bonding strength of the brazing joint. It was found furthermore that these reaction-product coatings on the surface of the reinforcing particles can improve the mechanical properties when these form a thin coating with thickness of around 2 μm, but thicker coatings on the particles decrease the mechanical properties. In this case the aim is to achieve athin coating. The film thickness can be reduced by reducing the brazing time.

The reaction between the diamond particles and the matrix alloy can also be observed in thecase of another matrix alloy, such as a diamond/Ni-Cr based alloy composite system [30]. In this system the diamond/matrix Cr_3C_2 and Cr_7C_3 compounds appearing on the interface can decrease the mechanical properties of the composite. In this case we have another problem, namely the diamond graphitisation promoted by Ni, which can catalyse the activation energy reduction in graphitisation. The hardness of the composite is reduced by the graphitisation of the diamond.

4. Composite coating from aqueous solutions by electrochemical and electroless methods

Not only nanoparticle-reinforced composites but also Ni or Co coatingsare appropriate for improving the wear resistance of the cutting tool. One of theproduction methods of composite and alloy coating is from aqueous solution by electrochemistry i.e. Ni/TiO_2 [6], Ni/SiC [32, 33], alloyed matrix composites, i.e. Ni-W/SiC [34], Ni-Co/SiC [35], Ni–B/CeO_2 [36] and Co/SiC [33, 37].

Ni/SiC and Co/SiC [33, 37], Ni-W-P/Al_2O_3 [7], and Ni–P/Si_3N_4 [38] composite coatings can be prepared by the electroless method. Electroless plating is good for preparing a metallic

coating on the surface of tools, i.e. Ni-P [39], Co-P [40], Co-B [41]. Both electrochemical and electroless plating are easy methods which are applicable for preparing coatings on tools with complex surfaces.

Comparing the features of electrochemically deposited Ni and Ni/SiC composite coatings, we find that the Ni/SiC composite hardness and wear characteristics are better than those of Ni coatings which are produced in the same manner. The Ni-5% SiC nanoparticle-reinforced composite coating has a maximum microhardness and wear rate of730 Hv and$2.5 \cdot 10^{-6}$$mm^3$/J, respectively (The microhardness and the wear rate of the Ni coating were 550Hv and $5.5 \cdot 10^{-6}$ mm^3/J, respectively). The reason for this is that the SiC nanoparticles deposited in the nickel matrix restrain the growth of the nickel grains and the plastic deformation of the matrix under loading, due to grain fining and dispersive strengthening effects [42].

Similar results were obtained also in the case of electroless Ni-W-P coating and Ni-W-P/Al_2O_3 composite coating [7]. Table 1 shows that the hardness of the composite is only slightly improved against the Ni-W-P coating. However, the value of hardness can be doubled by annealing at 400–500 °C.

Table 1

Microhardness values of electroless Ni-W-P and Ni-W-P/Al_2O_3composite *coatings asplated and annealed atvarious temperatures [7]*

Type of coating	**Microhardness (VHN_{50gf})**				
	As-plated	200 °C	400 °C	500 °C	600 °C
Ni-W-P coating	578±29	612±16	1052±23	992±10	797±14
Ni-W-P/Al_2O_3 composite coating	581±18	836±47	1178±48	1227±72	939±42

Reduction of hardness with respect to higher annealing temperature is a consequence of Ni_3P grain coarsening, Ni recrystallisation and the elimination of point defects. The decrease in hardness at 600 °C can be attributed to the precipitation of a major amount of Ni crystallites compared to the Ni_3P phase [7].

In the case of electroless Ni-B coating we can achieve a significant increase in the value of hardness by heat treatment. The reason for the increaseinhardness is the phase transformation from as-deposited coatings (rather soft supersaturated fcc nickel) to crystallised Ni_3B nickel-boride (orthorhombic system) during heat treatment [43].

The properties of the composite coatings show significant differences according to whether the electroless or electrolytic method was used. Co/SiC composite coatings were investigated by Rudnik et al. [37]. A multilayer composite coating was formed, and they found that the hardness of samples made using the electroless method was 17 times higher than that of the base metal (aluminium), while the hardness of the electrodeposited composite coating was 9 times higher than that of the base metal [37].

Summary

In this review we have collected the results of research on preparations of surface composites and coatings, and here we summarize the findings.

Using the laser technologies there are some difficulties in the preparing of the composite coating. On is the poor wettability between the melted metal and the reinforcing particles and another is the chemical reaction between the two phases. Both the poor wettability and the

chemical reaction can decrease the mechanical properties of the composite coatings. These difficulties can be solved when the reinforcing particles are formed in-situ during the cooling of the melted metal. For example by adding Cr_3C_2 particles into the melted Ni or Ni-B matrixduring the heat process, the Cr_3C_2 particles can completely dissolve in the Ni matrix alloy. During the rapid cooling process Cr_7C_3 and $Fe_{23}(C, B)_6$ phases can be well dispersed in the matrix, causing an improvement in the hardness of the coating.

Mechanical stresses may occur in the sample using the laser methods because of rapid cooling of the melted part and the non-uniform temperature. In order to avoid such high mechanical stresses in the sample, there is growing interest in composite coating preparation by brazing under high vacuum or an inert gas atmosphere, where the whole sample is heated up during the brazing process. A brazing belt or brazing paste can be made from the powder of the brazing alloy and the reinforcing material using a large volume of organic binder. The brazing pastes are especially applicable for preparing a composite brazing coating on the complex surface of engineering components.

The electrochemical and electroless methods are also suitable for preparing wear-resistant compounds or composite coatings on complex surfaces, but provide weaker bonding between substrate and coating than brazing. Electroless plating may yield higher hardness than electrochemical plating.

Acknowledgements

The research work presented in this paper is based on the results achieved in the Center of Applied Materials Science and Nanotechnology at the University of Miskolc and carried out as part of the TÁMOP-4.2.2.D-15/1/KONV-2015-0017 project in the framework of the New Széchenyi Plan. The realisation of this project is supported by the European Union, and co-financed by the European Social Fund.The authors are grateful to Robin Lee Nagano for her advice.

References

[1] Klages, C.-P.–Fryda, M.–Matthke, T.–Schafer, L.–Dimigen, H.: Diamond coatings and cBN coatings for tools. *International Journal of Refractory Metals & Hard Materials,* 16, 1998, 171–176.

[2] Karvankova, P.–Veprek-Heijman, M. G. J.–Zindulka, O.–Bergmaier, A.–Veprek, S.: Superhardnc-TiN/a-BN and nc-TiN/a-TiBx/a-BN Coatings Prepared by Plasma CVD and PVD: A Comparative Study of their Properties. *Surface and Coatings Technology,* 163–164, 2003, 149–156.

[3] Rickerby, D. S.–Matthews, A.: *Advanced Surface Coatings: a Handbook of Surface Engineering.* Blackie, Glasgow, 1991.

[4] Li, Q.–Lei, T. C.–Chen, W. Z.: Microstructural characterization of WCp reinforced Ni-Cr-B-Si-C composite coatings. *Surface and Coatings Technology,* 114, 1999, 285–291.

[5] Vreeling, J. A.–Ocelík, V.–Hosson, J. T. M. De: Ti–6Al–4V strengthened by laser melt injection of WCp particles. *Acta Materialia,* 50, 2002, 4913–4924.

[6] Baghery, P.–Farzam, M.–Mousavi, A. B.–Hosseini, M.: Ni–TiO_2 nanocomposite coating with high resistance to corrosion and wear. *Surface & Coatings Technology,* 204, 2010, 3804–3810.

[7] Balaraju, J. N.–Kalavati–Rajam, K. S.: Electroless ternary Ni–W–P alloys containing micron size Al_2O_3particles. *Surface & Coatings Technology,* 205, 2010, 575–581.

[8] Ming–Q.–Lim–L. C.–Chen, Z. D.: Laser cladding of nickel-based hardfacing alloys. *Surface and Coatings Technology,* 106, 1998, 174–182.

[9] Pei, Y. T.–Zuo, T. C.: Gradient microstructure in laser clad TiC-reinforced Ni-alloy composite coating. *Materials Science and Engineering: A,* 241 (1–2), 1998, 259–263.

[10] PEI, Y. T.–OUYANG, J. H.–LEI, T. C.–ZHOU, Y.: Microstructure of laser-clad SiC-(Ni alloy) composite coating. *Materials Science and Engineering A,* 194, 1995, 219–224.

[11] DAWEI, Z.–LI, T.–LEI, T. C.: Laser cladding of Ni–Cr_3C_2/(Ni+Cr) composite coating. *Surface and Coatings Technology,* 110, 1998, 81–85.

[12] ZHANG, D.-W.–LEIB, T. C.–LIA, F.-J.: Laser cladding of stainless steel with Ni–Cr_3C_2 for improved wear performance. *Wear,* 251, 2001, 1372–1376.

[13] ZHANG, D.-W.–LEI, T. C.: The microstructure and erosive–corrosive wear performance of laser-clad Ni–Cr_3C_2 composite coating. *Wear,* 255, 2003, 129–133.

[14] LI, Q.–LEI, T. C.–CHEN, W. Z.: Microstructural characterization of laser-clad TiCp-reinforced Ni–Cr–B–Si–C composite coatings on steel. *Surface and Coatings Technology,* 114, 1999, 278–284.

[15] OUYANG, J. H.–PEI, Y. T.–LEI, T. C.–ZHOU, Y.: Tribological behaviour of laser-clad TiCp, composite coating. *Wear,* 185, 1995, 167–172.

[16] KAPTAY, Gy.: Interfacial Phenomena during Melt Processing of Ceramic Particle-Reinforced Metal Matrix Composites. Part I. Introduction (incorporation) of solid particles into melts. *Materials Science Forum,* 215–216, 1996, 459–466.

[17] KAPTAY Gy.: Kerámiával erősített fémmátrixú kompozitok gyártásának határfelületi vonatkozásai I. A határfelületi kritériumok levezetése (Interfacial aspects of producing MMCs. Part I/1. Derivation of interfacial criteria) (in Hungarian). *BKL. Kohászat,* 130 (5–6), 1997, 201–208.

[18] JANÓ V.–BUZA G.–KÁLAZI Z.: Diszperz eloszlású, fémmatrixú kerámia kompozitréteg létrehozása lézersugaras felületkezeléssel (Formation of a dispersedly distributed metal matrix ceramic composite coating by laser surface treatment). *Bányászati és KohászatiLapok,* 138 (3), 2005, 39–44.

[19] VEREZUB, O.–KÁLAZI, Z.–BUZA, G.–VEREZUB, N. V.–KAPTAY, Gy.: In-situ synthesis of a carbide reinforced steel matrix surface nanocomposite by laser melt injection technology and subsequent heat treatment. *Surface & Coatings Technology,* 203, 2009, 3049–3057.

[20] PEI, Y. T.–OCELIK, V.–DE HOSSON, J. T. M.: SiCp/Ti6Al4V functionally graded materials produced by laser melt injection. *Acta Materialia,* 50, 2002, 2035–2051.

[21] MRIDHA, S.–BAKER, T. N.: Incorporation of 3μm SiCp into Titanium surfaces using a 2.8kW laser beam of 186 and 373 MJm^{-2} energy densities in a nitrogen environment. *Journal of Materials Processing Technology,* 185, 2007, 38–45.

[22] CHEN, Y.–LIU, D.–LI, F.–LI, L.: WCp/Ti–6Al–4V graded metal matrix composites layer produced by laser melt injection. *Surface & Coatings Technology,* 202, 2008, 4780–4787.

[23] LIU, D.–LI, L.–LI, F.–CHEN, Y.: WCp/Fe metal matrix composites produced by laser melt injection. *Surface & Coatings Technology,* 202, 2008, 1771–1777.

[24] NASCIMENTO, A. M. Do–OCELÍK, V.–IERARDI, M. C. F.–HOSSON, J. T. M. De: Wear resistance of WCp/Duplex Stainless Steel metal matrix composite layers prepared by laser melt injection. *Surface & Coatings Technology,* 202, 2008, 4758–4765.

[25] AGARWAL, A.–DAHOTRE, N. B.: Laser surface engineering of steel for hard refractory ceramic composite coating. *International Journal of Refractory Metals & Hard Materials,* 17, 1999, 283–293.

[26] LU, S.-P.–KWON, O.-Y.: Microstructure and bonding strength of WC reinforced Ni-base alloy brazed composite coating. *Surface and Coatings Technology,* 153, 2002, 40–48.

[27] LU, S.-P.–KWON, O.-Y.–GUO, Y.: Wear behavior of brazed WC/NiCrBSi(Co) composite coatings. *Wear,* 254, 2003, 421–428.

[28] WANG, X.–ZOU, Z.–ZHANG, M.–QU, S.: Microstructure and wear properties of WC–TiC–Co/CuZnNi composite surface coating. *Journal of Materials Processing Technology,* 172, 2006, 188–194.

[29] WANG, X.–ZHANG, M.–ZOU, Z.–QU, S.: Wear properties of cemented carbides/Cu-based alloy composite strengthening materials for milling shoes. *Wear,* 260, 2006, 10–15.

[30] DUAN, D.-Z.–XIAO, B.–WANG, W.–ZHANG, Z.-Y.–WANG, B.–HAN, P.–DING, X.-Y.: Interface characteristics and performance of pre-brazed diamond grains with Ni–Cr composite alloy. *Journal of Alloys and Compounds,* 644, 2015, 626–631.

[31] WU, M.–CAO, C.-Z.–RAFI-UD-DIN–HE, X.-B.–QU, X.-H.: Brazing diamond/Cu composite to alumina using reactive Ag-Cu-Ti alloy. *Transactions of Nonferrous Metals Society of China,* 23, 2013, 1701–1708.

[32] NIU, Z.-X.–CAO, F.-H.–WANG, W.–ZHANG, Z.–ZHANG, J.-Q.–CAO, C.-N.: Electrodeposition of Ni-SiC nanocomposite film. *Transactions of Nonferrous Metals Society of China,* 17, 2007, 9–15.

[33] RUDNIK, E.–JUCHA, T.–BURZYNSKA, L.–ĆWIĘKA, K.: Electro- and electroless deposition of Ni/SiC and Co/SiC composite coatings on aluminium. *Materials Science Forum,* 690, 2011, 377–380.

[34] YAO, Y.–YAO, S.–ZHANG, L.–WANG, H.: Electrodeposition and mechanical and corrosion resistance properties of Ni–W/SiC nanocomposite coatings. *Materials Letters,* 61 (1), 2007, 67–70.

[35] SHI, L.–SUN, C.–GAO, P.–ZHOU, F.–LIU, W.: Mechanical properties and wear and corrosion resistance of electrodeposited Ni–Co/SiC nanocomposite coating. *Applied Surface Science,* 252, 2006, 3591–3599.

[36] SHAKOOR, R. A.–KAHRAMANA, R.–WAWARE, U. S.–WANG, Y.–GAO, W.: Synthesis and properties of electrodeposited Ni–B–CeO2 composite coatings. *Materials & Design,* 59, 2014, 421–429.

[37] RUDNIK, E.–JUCHA, T.: Electroless and electrolytic deposition of Co–SiC composite coatings on aluminium. *Surface & Coatings Technology,* 232, 2013, 389–395.

[38] BALARAJU, J. N.–SESHADRI, S. K.: Synthesis and Corrosion Behavior of Electroless Ni–P–Si_3N_4 Composite Coatings. *Journal of Materials Science Letters,* 17 (15), 1998, 1297–1299.

[39] BALARAJU, J. N.–SANKARA NARAYANAN, T. S. N.–SESHADRI, S. K.: Electroless Ni–P composite coatings. *Journal of Applied Electrochemistry,* 33, 2003, 807–816.

[40] RUDNIK, E.–GORGOSZ, J.: The influence of maleic acid on the Co–P electroless deposition. *Surface & Coatings Technology,* 201, 2007, 6953–6959.

[41] MUIR, S. S.–CHEN, Z.–WOOD, B. J.–WANG, L.–LU, G. Q. (M.)–YAO, X.: New electroless plating method for preparation of highly active Co-B catalysts for $NaBH_4$ hydrolysis. *International Journal of Hydrogen Energy,* 39, 2014, 414–425.

[42] VAEZI, M. R.–SADRNEZHAAD, S. K.–NIKZAD, L.: Electrodeposition of Ni–SiCnano-composite coatings and evaluation of wear and corrosion resistance and electroplating characteristics. *Colloids and Surfaces A: Physicochemical and Engineering Aspects,* 315, 2008, 176–182.

[43] VITRY, V.–KANTA, A.-F.–DELAUNOIS, F.: Mechanical and wear characterization of electroless nickel-boron coatings. *Surface & Coatings Technology,* 206, 2011, 1879–1885.

Materials Science and Engineering, Volume 40, No. 1 (2015) pp. 33–41.

DETERMINATION OF THE MAIN, MINOR AND TRACE METALLIC COMPONENTS OF ANODE SLIME BY ICP-AES SPECTROMETRY FOLLOWING WET CHEMICAL SAMPLE PREPARATION

OLIVÉR BÁNHIDI[1]

In this paper an analytical method based upon wet chemical sample preparation developed for the analysis of anodic slime is presented. Sincethe main-, minor and trace elements to be determined are simultaneously present in the sample, it is of crucial importance that the sample preparation procedure does not adversely affect the detection power of the method. With respect to the elementary composition of the slime, careful experimental work was needed to find the mixture of acids which would dissolve all components of the sample. Potential interference effects among the main constituents were also studied.

Keywords: Wet chemical sample preparation of slime, ICP-AES analysis of main, minor and trace constituents

Introduction

In the European Union the use of lead as a basic constituent of the soldering alloys applied for manual soldering and for solder bathes is restricted by the RoHS2 directive [1]. Therefore lead-free soldering alloys have become widely applied for interconnection purposes in the manufacturing of electronic parts [2]. Regarding their chemical composition, these alloy systemspreferentially contain tin (≥ 90 m/m%), silver (1–4 m/m%) and copper (0.5–1.5 m/m%) as main constituents, but sometimes Sb and Bi are added minor components. Trace levels of As, Bi, Fe, Ni, Pb, Sb might as well be present.

In the course of microelectronic manufacturing the formation of more or less processing waste is inevitable. Since this waste contains valuable metals, beyond environmental and sustainable considerations, it is important to recover as much from these materials as possible, so the processing of solder waste is practically mandatory. There are several methods available for that purpose. One of them includes electrochemical processes, e.g. the anodic dissolution of the waste. During the dissolution process anodic slime forms, which contains metallic elements, therefore slime processing, (i.e. the recovery of the valuable components) is preferred from both the environmental and economic viewpoints. In order to develop a suitable procedure, there is a constant need for analytical information concerning the chemical composition of the slime.

Elemental concentrationsrange from mg/kg level up to 90 m/m%, that's why the analytical method must be capable of providing reliable results along this wide concentration range. When selecting the most appropriate analytical method, an important fact to be taken into account: is that various intermetallic compounds may occur either in the course of alloy-manufacturing or during soldering depending on the concentration of the minor elements [3, 4]. Regarding their physical and chemical properties, these compounds more or less differ from the bulk material.

When solid-sample analytical methodsare to be applied for the determination of the chemical composition of the slime, the certified reference materials (standards) used for calibration and validation must contain the same type and quantity of intermetallic

[1] University of Miskolc, Institute of Chemistry
Miskolc-Egyetemváros 3515, Hungary

compounds as the samples, because of possible matrix effects. Due to their specific chemical composition and structural properties such reference materials are hardly available making the application of solid sample analytical methods rather difficult.

On the other hand, instrumental analytical methods that require the dissolution of the samples are not sensitive to this problem because dissolution actually eliminates the presence of IMCs. The only thing that has to be taken care of is that the sample must be completely dissolved. The presence of the intermetallic compounds can make the dissolution processa bit more difficult.

Several instrumental methods use wet chemical sample preparation, but regarding the strict requirements (wide concentration range, multi-element capability, relative insensivity to chemical interferences) ICP-AES fits the best for this purpose, indeed, this spectroscopic technique is suitable to determine all the elements that might be encountered in the samples [7]. An other favoured technique is the X-ray Flourescence Spectrometry, which is a solid-sample multi-element analytical method, therefore it proved to be excellent to determine some minor components of slimes, but lack of solid certified reference materials it is unsuitable for the determination of the main constituents of such samples [6].

The development of anICP analytical method involves 2 steps; first a suitable dissolution procedure must be worked out, then the parameters of the ICP analytical programme have to be set up. During the preliminary analysis of the slime it turned out that the main metallic constituents are Ag, Cu and Sn, but their concentrationsconsiderably differ from those pertinent in the led free soldering alloys. Unlike the alloys copper also can be found at high concentration in the tin-based anodic slimes.

1. Experimental

1.1. The dissolution procedure

Considering the dissolution procedure, the chemical properties of the main components areof key importance. Tin can be dissolved in hydrochloric acid, but care must be taken of the acidity of the solution, especially while diluting the sample solution or filling it up to the mark of the mark of the volumetric flask using distilled water. Silver and copper can be brought into solution using nitric acid of at least 25 m/m% concentration. It is also important that silver ions react with chloride ions, yielding a white deposit (silver-chloride) insoluble in aqueous media and dilute acidic solutions. Nevertheless there is hardly any information available about the solubility of silver-chloride in concentrated nitric acid or in a concentrated mixture of nitric acid and hydrochloric acid. Preliminary experiments have been carried out to examine whether there is any difference regarding solubility in these medias. We managed to dissolve $AgNO_3$ in concentrated nitric acid, and keep it in dissolved state while diluting the solution with 5.7 mol/dm^{3}of hydrochloric acid. The effect of nitric acid on tin was also studied and it turned out that no metastannic acid forms if the concentration of nitric acid does not exceeds 30 m/m%, moreover the solution remains stable for at least a week.

Based upon these results aqua regia was chosen as the dissolving agent and the solution was diluted with hydrochloric acid of 5.7 mol/dm^3. The procedure developed for the dissolution of the anodic slime was the following: 0.2 g sample wasweighed using an analytical balance and the sample was taken into a glass beaker. 6 cm^3 of concentrated hydrochloric acid and 2 cm^3 of concentrated nitric acid were added to the sample and the mixture was gently heated until the solid material dissolved in the liquid. When the solution cooled down, it was filled up in a volumetric flask to 50 cm^3 with hydrochloric acid of 5.7 mol/dm^3.

1.2. The instrument

The instrument applied in the experiments was an axially viewed simultaneous multi-element ICP spectrometer, type 720 ES by Varian Inc. The technical specifications are presented in Table 1.

The optical system of the ICP instrument made it possible to choose several lines for each element measured. The intensity of each line chosen was measured at the same time, so the measurement time did not depend on the number of spectral lines. Using multiple lines for one element has the following advantages: On one hand, calibration and sample measurements can be carried out an over wide range – even from $\mu g/dm^3$level concentrations up to more than 100 mg/dm^3without diluting the sample (supposing that lines with different sensitivities are chosen).On the other hand, the occurrence of any unexpected spectral interference can be easily recognized and the result provided by the disturbed line can be left out. The spectral lines chosen and their most important properties are presented in Table 2. As for the measurement conditions the following parameters were applied:

A V-groove type nebulizer with Sturman–Masters spray chamber was used as sample introduction device, which is able to endure the use of solutions of concentrated acids, or mixture of acids [5]. The high-frequency power (P_{RF}) applied to the plasma was 1050 W. Integration time was 10 s and in each case the measurement result was obtained by averaging 3 consequent readings – except for those carried out to determine the detection limits. Net intensity values were obtained using two-side off-peak background correction.

1.3. Detection power

Since trace elements are inasmuch targets of the determination as the components present at higher concentration, detection power plays a very important role. The sample solutions contain hydrochloric acid and nitric acid at high concentration, therefore it also must be known whether this acid mixture influences the detection power and if so, how much then. So as get correct information, the detection limits on the spectral lines chosen have been determined both in dilute aqueous solution and in acid-mixture. The measurements were performedunder the same conditions as the analytical determinations, except for the number of parallel measurements. Each average was calculated from ten readings. The results are presented in Table 3.

Table 1

Features of the ICP spectrometer used in the course of experiments

Type of viewing the plasma:	Axial
The frequency of the generator:	40 MHz
The RF power applied on the torch:	900–1500 W, adjustable by the software
Type of the optical system:	Double monochromator with Echelle gratings
Type of detector:	Two-dimension CCD
Wavelength range:	160–780 nm
Primary sample introduction system:	Pneumatic (K-type) nebulizer
Secondary sample introduction systems:	Ultrasonic nebulizer
	V-groove nebulizer with Sturman–Masters sp.ch.
Controlling software:	ICP Expert II (under Microsoft Windows XP)

Table2

The measured spectral lines of the analyte elements

Element	Type of the line	Wavelength [nm]	Excitation energy [eV]
Ag	Ag I	328.058	3.81
	Ag I	338.289	3.69
As	As I	188.980	6.61
	As I	193.696	6.33
	As I	197.198	6.48
Bi	Bi I	190.171	6,57
	Bi I	223.061	5,60
Cu	Cu II	199.970	6.25
	Cu II	213.598	5.85
Fe	Fe II	234.350	5.33
	Fe II	238.204	5.24
	Fe II	259.940	4.81
Ni	Ni II	216.555	5.77
	Ni II	231.604	5.39
Pb	Pb I	182.143	6.86
	Pb I	217.000	5.76
	Pb II	220.353	5.67
Sb	Sb I	187.052	6.68
	Sb I	206.834	6.04
	Sb I	231.146	5.40
Sn	Sn I	181.059	6.90
	Sn I	189.925	6.58
	Sn I	235.485	5.30

Table3

The detection limit (DL) in aqueous media and in the acid mixture used forbringing the samples into solution using V-groove nebulizer and Sturman–Masters spray chamber

Element	Wavelength [nm]	$DL_{aqueous}$ [µg/dm^3]	$DL_{acid-mix.}$ [µg/dm^3]	DL_{solid_sample} [mg/kg]
Ag	328.058	0.85	0.70	0.4
	338.289	4.76	5.83	3.0
As	188.980	6.62	12.20	6.1
	193.696	8.05	9.50	4.8
	197.198	12.48	15.6	7.8
Bi	190.171	19.8	16.7	8.5
	223.061	6.74	11.1	5.6
Cu	199.970	13.45	10.40	5.2
	213.598	1.40	2.45	1.2
Fe	234.350	5.19	2.23	1.1
	238.204	4.89	1.09	0.5
	259.940	5.32	0.79	0.4
Ni	216.555	2.29	2.38	1.2

	231.604	5.05	2.67	1.3
Pb	182.143	23.1	27.1	13.5
	217.000	12.8	16.2	8.0
	220.353	6.08	9.52	4.8
Sb	187.052	35.5	141.3	70.0
	206.834	9.46	37.8	19.0
	231.146	17.7	22.3	11.0
Sn	181.059	70.7	27.50	13.8
	189.925	61.3	12.9	6.5
	235.485	71.6	22.1	11.0

As it is apparent from Table 3.not even by applying acid mixture does the detection power of the ICP device deteriorate substantially. There are lines, which have lower DLs in the acid mixture then in the aqueous solution. The rightmost column of the table contains the DLs calculated for the solid sample, taking into account the fact that the dissolution process produces a solution with a sample concentration of about 2000 mg/dm^3.

1.4. Possible matrix effects

Possible matrix effects among the main components must also be studied. In this respect only the main components were studied, because the trace elements will be calibrated with the help of matrix matched calibration solutions. The test solutions containing the 3 main elements were prepared using concentrated nitric acid containing 1000 mg/dm^3 silver. Some hydrochloric acid of 5.7 mol/dm^3 was gently added to the silver stock solution, then the calculated quantity of copper and tin were added in the form of concentrated stock solutions, finally the solutions were filled up to the mark – with hydrochloric acid of 5.7 mol/dm^3 – of a volumetric flask. The test solutions contained the main elements in the following concentration range: Ag: 50–300 mg/dm^3, Cu: 100–500 mg/dm^3, Sn: 100–500 mg/dm^3

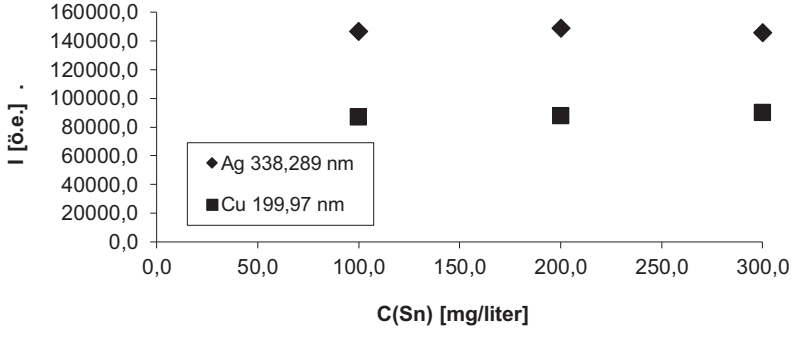

Figure 1. The effect of Sn on the intensity of the Ag line of 338.289 nm and Cu line of 199.97 nm

Three series of solutions were measured, in each series the concentration of one main element was constant, while that of the others changed. The results can be seen in Figures 1, 2 and 3.These figures indicate only slight interference effects among the main components.

2. Results

The results of the above describedinvestigations support the assumption that neither strong spectral interferences, nor chemical matrix effects are likely to occur on the lines studied, therefore the application of matrix-matched calibration solutions prepared from mono-element stock solutions will provide reliable results. The calibration curves measured for the three main elements can be seen in Figures 4, 5 and 6. With the help of the method developed it is possible to determine silver content up to 20 m/m%, tin content up to 35 m/m% and copper up to 40 m/m%. The performance of the method is demonstrated by the results presented in Table 4.

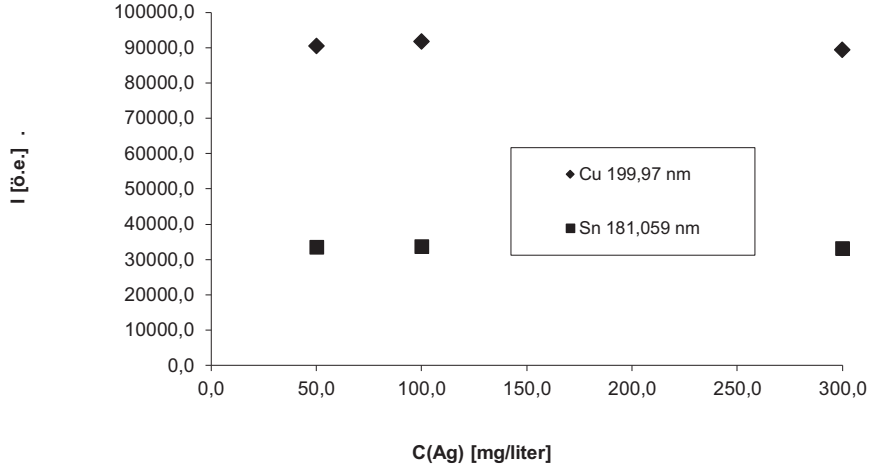

Figure 2. The effect of Ag on the intensity of the Cu line of 199.97 nm and Sn line of 181.059 nm

Discussion of the results

In devising the new analytical method two tasks had to be solved. The first was to develop a proper dissolution procedure, that would bring the samples into solution and yields a solution, from which both the main constituents and the trace elements can be determined. The second task was to develop an ICP analytical program suitable for the analysis using solutions containing hydrochloric acid and nitric acid at high concentrations. The data presented in Table 3 show that no substantial reduction of the detection power has to be encountered, while Figures 1, 2 and 3 suggest that the main components are affected only slightly by one-another. Using matrix

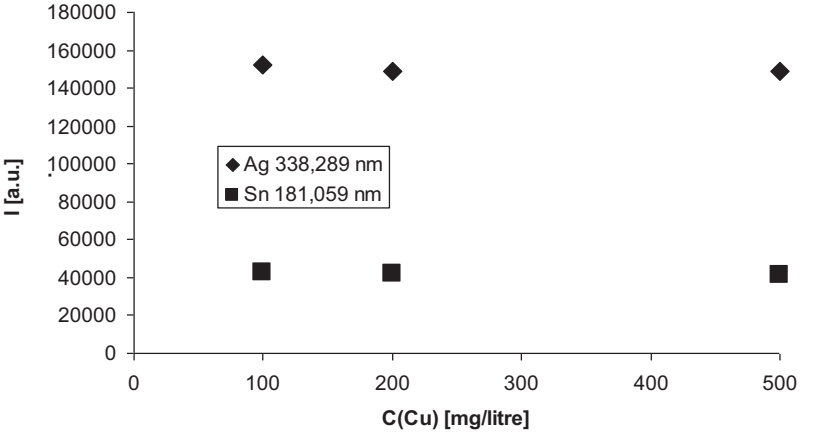

Figure 3. The effect of Cu on the intensity of the Ag line of 338.289 nm and Sn line of 181.059 nm

-matched calibration solutions linear calibration curves could be obtained suitable for analysis in a wide concentration range. In the resulting solution obtained using the sample preparation procedure the concentration of the sample is 2000 mg/dm^3, which, -based upon the detection limits presented in Table 3 makes possible to determine the trace elements at mg/kg levels, as it can be seen in Table 4.

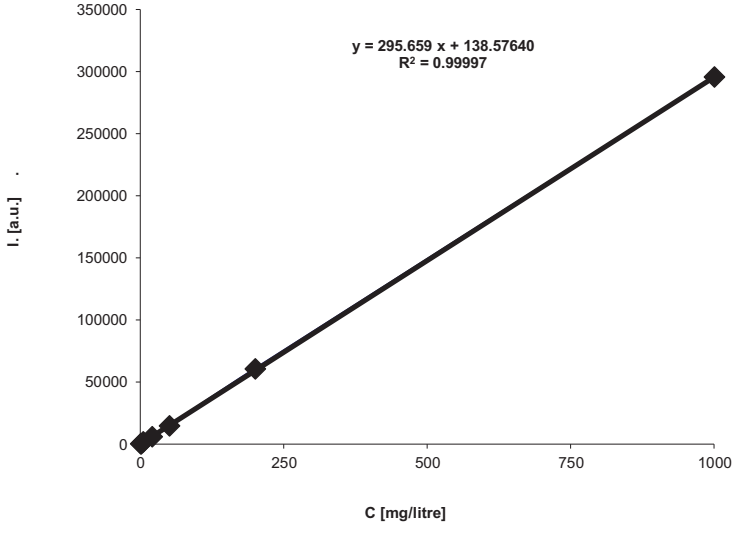

Figure 4. The calibration curve for copper on the 199.97 nm line

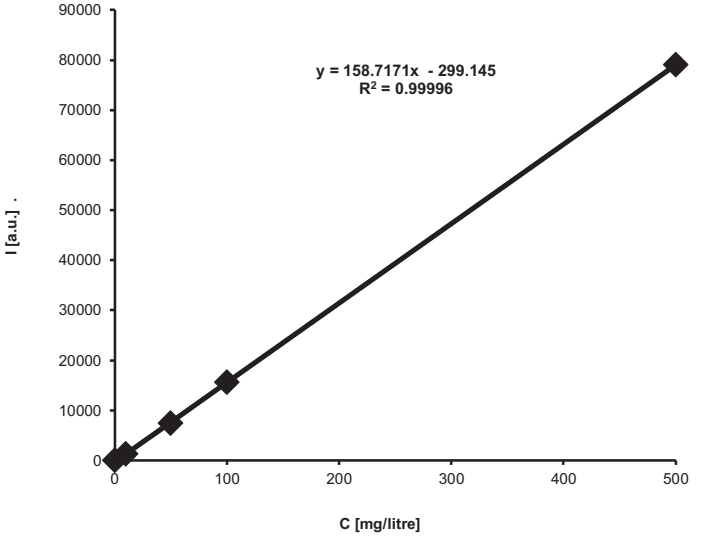

Figure 5. The calibration curve for Sn on the 181.059 nm line

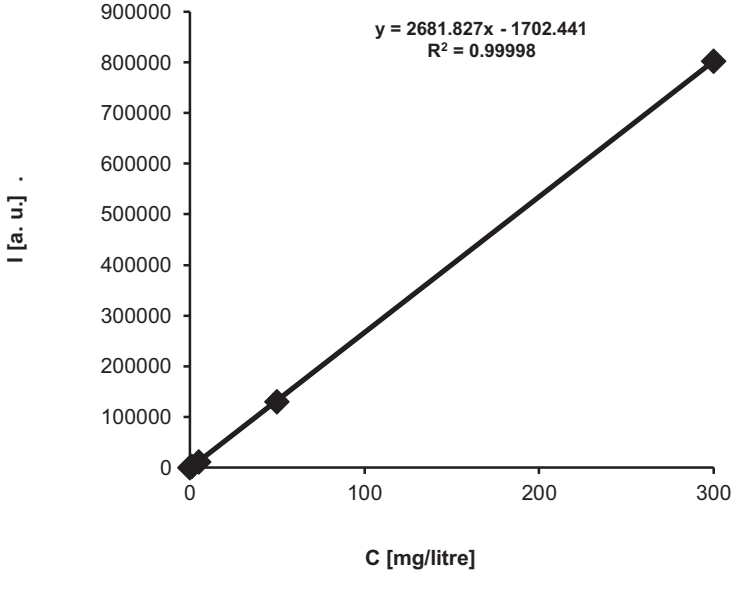

Figure 6. The calibration curve for Ag on the 338.289 nm line

Table 4

Results of 5 parallel measurements of a sample. All values are indicated in m/m% unit. Av: average; SD: standard deviation; CI: confidence interval (in rel. %)

Element	**Ag**		**Bi**		**Cu**		**Fe**		
λ [nm]	328.058	338.289	190.171	223.061	199.970	213.598	234.350	238.204	259.94
Av. [%]	15.59	16.61	0.0056	0.0065	40.00	40.49	0.0111	0.0121	0.011
SD [%]	0.433	0.440	0.0007	0.0005	0.38	0.09	0.0007	0.0005	0.0005
CI (p = 95%)	5.55	5.30	25.0	15.4	1.90	0.45	12.6	8.26	9.09
Element	**Pb**			**Sb**			**Sn**		
λ [nm]	182.143	217.000	220.353	187.052	206.834	231.146	189.059	189.925	
Av. [%]	0.0015	0.0020	0.0014	0.0588	0.0496	0.0550	18.46	18.77	
SD [%]	0.0007	0.0006	0.0007	0.0009	0.0008	0.0008	0.32	0.15	
CI (p = 95%)	93.3	60.0	100.0	3.06	3.23	2.91	3.47	1.60	

Acknowledgement

The research work presented in this paper/study/etc. based on the results achieved within the TÁMOP-4.2.1.B-10/2/KONV-2010-0001 project and carried out as part of the TÁMOP-4.2.2.A-11/1/KONV-2012-0019 project in the framework of the New Széchenyi Plan. The realization of this project is supported by the European Union, and co-financed by the European Social Fund.

References

[1] *Directive 2011/65/EU of the European Parliament and of the Council of 8 June 2011 on therestriction of the use of certain hazardous substances in electrical and electronic equipment.*

[2] SIEVERT, T.–LIU, S.–SMITH, D. R.–MADENI, J. C.: *Database for Solder Properties with Emphasis on New Lead-free Solders, Properties of Lead-free Solders, Release 4.0.* National Institute of Standards and Technology & Colorado-School of Mines, Colorado, 11 February, 2002.

[3] KIMA, K. S.–HUHA, S. H.–SUGANUMAB, K.: *Journal of Alloys and Compounds,* 352, 2003, 226.

[4] NOGITAA, K.–NISHIMURAB, T.: *Scripta Materialia,* 29, 2008, 191.

[5] TREVIZAN, Lilian C.–VIEIRA, Edivan C.–NOGUEIRA, Ana Rita A.–NÓBREGA, Joaquim A.: *Spectrochimica Acta Part B,* 60, 2005, 575.

[6] HARPER, M.–PACOLY, B.: *J. Environ. Monit.,* 8, 2006, 140.

[7] LEODOLTER-DWORAK, M.–STEFAN, I.–PLUMBRIDGE, J. W.–IPSER, H.: *Journal of Eletcronic Materials, 39, 1, 105.*

Materials Science and Engineering, Volume 40, No. 1 (2015) pp. 42–49.

SOLDER MATERIALS WITH MICRO AND NANOPARTICLES: A REVIEW

PÉTER BAUMLI[1]

EU legislation requires that lead and other critical alloying elements have to be removed or replaced by non-hazardous element in the certain segments of the soldering technology. The mechanical and thermal properties, such as tensile strength and melting point, of the newly developed lead-free solder alloys differsignificantly from the previously used lead-tin solders. Nowadays researchers deal with nanostructured solders that are capable of changing these properties.

The melting point of the solder can be reduced by paste solder from metal nanoparticles and the mechanical properties can be improved by a non-soluble nanoparticle-reinforced nanocomposite solder. The results of research on nanostructured solders are collected in this review.
Keywords: lead-free solder, composite, nanoparticles

Introduction

Till now the most successful solder alloysweretin-lead(Sn-Pb), which has appropriate chemical, physical and thermal properties. These properties result in a good bond between the solder and substrate [1].

Different alloying elements can be used to improve the mechanical properties of lead-free solder, i.e. silver [2] or nickel [3]. Nickel can improve the mechanical properties by reducing the thickness of the Cu_3Sn intermetallic (IMC) layer on the interface of the solder/substrate [3]. The wettability of the solder can be improved by adding rare earth metals, e.g. lanthanum (La) and cerium (Ce) [4].

A higher number of elements in lead-free solder can solve the problem of the melting temperature as well. Namely, the solder materials of highest importance in practice, the SAC alloys (S = tin, A = silver, C = copper) have a higher melting point than the Sn-Pb solders. From the viewpoint of technology,this means that the currently used Printed Circuit Boards (PCBs) must be exchanged for higher temperature tolerant PCBs, which involves higher costs. Solder pastes from nano-sized alloy particles are a promising technique for decreasing the melting point of the solder [5].

Nanoparticles (NPs) are also adapted to improve the mechanical properties, as reinforcing materials. Nowadays, composite materials are widely used for improving the properties of materials. Based on this, we can assume that composites are able to fulfil an important role in soldering technology.

1. Classes of particles for composite solder materials

Nano- and micro-sized particles or fibres are applicablefor the preparation of the composite solder. These reinforcing phases can be metals, oxide-, carbide- or nitride ceramics or non-metals,e.g. carbon nanotubes (CNTs). The reinforcing materials can be classified into the following groups according to their behaviour with the solder material [6, 7]:

[1] University of Miskolc, Metalforming and Nanotechnology
Miskolc-Egyetemváros 3515, Hungary
peter.baumli@gmail.com

- In Group I we can categorise the nano- and micro-sized solid phases whose particles may react with a component of the solder and can dissolve in the matrix during the melting or reflow to create an IMC on the solder/substrate interface.On this basis, the elements belonging here are Al, Fe, Zn, Ni, Ag, Cu and Co. These elements may be used as micro-sized particles. In this case, due to the larger size of the particles they cannot completely dissolve in the solder materials, and a "flower-like" IMC structure can form on the surface of these micro-sized particles. The properties of the micro-sized-particle reinforced composite solder tend to deteriorate because of the flower-like structure, which can cause cracks.
  The solder material can be composed of nano-sized particles, namely the solder particles are dispersed in an organic medium. This solder material is the paste. Without oxide or any other reinforcing material in this paste it is not a composite solder.

- In Group II the nano-sized intermetallic phases are categorised, e.g. Sn_6Cu_5, Cu_3Sn, Ni_3Sn_4 and Ag_3Sn. The equilibrium can be reached by using these particles and thus the reactivity between the solder and the substratecan be reduced. In this case the melted solder is not able to create a crater in the substrate in contrast with the solder without intermetallic nanoparticles.

- The inert nano- and micro-particles belong to Group III, e.g. Al_2O_3, TiO_2 and CNTs. These particles do not react with the solder material but they are suited for acting as the sites for the heterogeneous nucleation of β-tin or intermetallic phase, so the size of β-tin and IMC can be reduced significantly on the interface of the solder/substrate.
  In the development of a composite solder, similarly to other metal matrix composites [8, 9]. It is necessary to consider that the surface of the reinforcing materials is not wetted perfectly by the melted alloys, which means the adhesion between solder and reinforcing phaseis weak. The adhesion can be improved by a metallic coating on the surface of the reinforcing materials, e.g. nickel coating on the surface of CNTs [10].

2. Preparation of the composite solders

The metal matrix composites can be categorised according to the preparation of the reinforcing materials. Accordingly we can speak about ex-situ and in-situ composites [11].

2.1. Ex-situ composites

Inert reinforcing particles can be mixed or stirred with the melted solder material. In this casting method the melted solder should be prevented from oxidation by using an inert gas atmosphere [12].

Solder paste can be made with reactive reinforcing materials that can react with the solder or can dissolve in the alloy. In this case we can prepare solder paste from the particles of the components.In preparing the solder paste, the reactive particles can be dispersed with the solder powder in a special water or organic solvent soluble flux [12–14].

Bulk solder (stripor wire) can be prepared by a method to avoid chemical reaction between the solder and the reinforcing particles before the soldering. First, the reinforcing particles and the powder of the solder alloy are homogenously mixed in alcohol. After the

drying of this slurry, the desired solder stripor wirecan be prepared bycold forming methods.

2.2. In-situ composites

Recently, the development of in-situ composites has been investigated by several research groups [12, 15–17]. The reinforcing materials are prepared by the reaction between the elements of the solder alloy, e.g. Cu_6Sn_5 phase from the reaction of Sn and Cu. The required elements of the solder are melted and kept at a given temperature for the formation of the desired IMCphase in the alloy, then the alloy is cooled down and hot rolled. In this way the IMCphases will be micro-sized and well dispersed [12, 15].

3. Application of metal nanoparticles

There are two main groups of metal nanoparticles according to their behaviour with the solder material. In the first group we can find the metallic particles that are dissolved in solders such as Ag or Cu. The non-soluble metal particles (e.g. Mo) belong to the other group.

The most commonly used nano- or micro-sized particles for the developing of the solders are from Cu [18], Ag [19], Al [20], Zn [21], Mo [22, 23], Co [24, 25], Ni [26] andSb [27]. These particles have been used for the production of Sn-Ag based solder, e.g. Sn-3.5Ag, and different SAC alloys, as well as for Sn-Pd, Sn-Cu and Sn-Zn alloys [7].

3.1. Interfacial behaviour of the solders containing metal nano- and micro-particles

The wettability of the copper plate can be improved by copper, nickel, or silver nanoparticles containing lead-free solders [6]; similarly, the solders which contain these elements as alloys but not nanoparticles [28].

Mo nanoparticles in Sn-Ag-Cu solder remain stable during multiple reflow cycles at 250 °C and the Mo nanoparticles do not dissolve in the matrix [23]. The molybdenum nanoparticles affect the formation of the IMCphase on the solder/substrate interface. The addition of Mo NPs to solder causes a decreasein the thickness of the IMC layer on the interface.

The effect of the Mo NPs and the insoluble NPswas explained by Haseeb [23], based on a study by Kim and Tu (cited in [23]). There are two IMC layers on the solder/substrate interface in the SAC solder/Cu substrate system. There is a Cu_3Sn IMClayer on the Cu side. The Cu_3Sn layer is covered by an IMClayer of Cu_6Sn_5 scallops which is directly on the solder side. Fluid channels exist between the Cu_6Sn_5 scallops, and these channels are extended to the Cu_3Sn/Cu interface. The fluid channels allow the possibility of quick diffusion for the dissolved copper, which results in further reaction and the extra Cu creates a thicker IMC layer on the interface. In the composite solder the non-soluble NPscan block the fluid channels, because the NPsare sorbed on the surface of the IMC.

The visible contact angle of the solder is increased and the spreading rate is decreased by the addition of non-soluble NPs or fibres to the solder, as shown in Table 1. The viscosity of the solder is increased by adding non-soluble NPs [29]. The higher viscosity keeps the solder from the spreading that gives rise to the increasing of the contact angle [30]. The increased contact angle value, however, is in the $20° \leq \Theta \leq 40°$ range, which is the necessary contact angle range for soldering.

Table 1

Wetting angle and spreading rate of SAC on Cu substrate with various addition of Co NPs [29]

Solder	Wetting angle(Θ), °	Spreading rate,%
Sn-3.8Ag-0.7Cu	19.46 ± 4.34	82.48 ± 2.42
Sn-3.8Ag-0.7Cu-0.18-CoNPs	26.95 ± 1.02	74.12 ± 4.85
Sn-3.8Ag-0.7Cu-0.41-CoNPs	25.76 ± 1.47	73.40 ± 5.32
Sn-3.8Ag-0.7Cu-0.75-CoNPs	26.71 ± 1.17	60.86 ± 5.32

The metal NPsare important for preparing the composite solder, but the solder itself can be made using metal NPs. In this case, the solderNPsare mixed with solder flux and/or other organic components [31]. Solder pastes prepared with metal NPshave a lower melting point than bulk solder with the same composition [5, 32–37] these results show a good agreement with thetheoretical model as well [35, 36].

The behaviour of the melting point of the SACalloy as a function of particle size was investigated by Gao et al. [32]. In their work an SAC alloy with grain size between 15–60 nm was produced and its melting behaviour was investigated by calorimetry. The melting point of the alloy changed from 218 °C to below190 °C, while the particle size changed from micron size to 10 nm [32]. This melting point is equivalent to the melting point of bulk Sn-Pb alloys, which is between 183 °C and 190 °C [38]. Nano-sized solder alloys, which have a higher melting pointin bulk, are applicable for lower temperature soldering. In this way the lower temperature tolerant PCBsdo not have to be changed to higher temperature tolerant PCBs.

3.2. Mechanical properties ofsolder prepared with metallic nanoparticles

In the development of a solder, there is high interest in its mechanical properties, because the solder bond used in equipment is liable to mechanical stress, such as vibrations, or shocks caused by being dropped. The mechanical properties of the metal NPscontaining solder will be illustrated in the following examples. The first example isan Sn-3.5Ag solder containing Co NPs(Sn-3.5Ag-CoNPs). The shear strength of Sn-3.5Ag-CoNPs compared toSn-3.5Ag improves as a function of the amount of the CoNPs. About 0.1 w% Co NPsin the solder causes an improvement in shear strength by ~28%. The shear strength of the Sn-3.5Ag-Co NPs composite solder reaches its maximum value at 0.1 wt.% CoNPs and from ~1.0 w% CoNPs the shear strength begins to decrease significantly: at 2.0 w% CoNPs reaches the value of the matrix material [39].

The silver in Sn-Zn-AgNPs compsite solder improves the mechanical properties as well. The shear strength of a Sn-Zn-AgNPs composite rises as function of the amount of AgNPs. The shear strength of the Sn-Zn alloy decreases with increasing reflow number. The shear strength of Sn-Zn-AgNPs composite solder is independent of the reflow number. The good mechanical properties are due to the formation of spherical-shaped $AgZn_3$IMCphases that are small in diameter, which can agglomerate and create micrometer-sized $AgZn_3$ islands in the solder [40].

The mechanical properties of Sn-3.5Ag solder can be improved by Ni and Mo nanoparticles. An increase in the amount of MoNPs causes higher hardness; moreover, the addition of Mo NPs and NiNPs can also improve the resistance against creep [41].

4. Application of oxide- and carbide ceramics and non-metallic materials

In the development of composite solders not only metal NPs are used; ceramic or non-metallic nano-sized phasescan also be used as reinforcing phase. The non-metallic reinforcing particles can be composed of oxides, e.g. TiO_2 [42, 43, 44], Al_2O_3 [45, 46], ZrO_2 [47] or Fe-Ni-oxide [48]; carbides, such as the most commonly used SiC [49, 50]; borides, e.g. TiB_2 [30]; as well as nanostructured POSS (polyhedral oligomeric Silsesquioxane) [51] orCNTs and fibres [10, 52, 53]. These materials are applied in order to improve mechanical properties, e.g. hardness and tensile strength, as well as shear strength.

4.1. Wettability and interfacial properties of ceramic NP reinforced compositessolder

The ceramics and non-metallic reinforcing phases can be classified into two groups. Inert materials (e.g. Al_2O_3, TiO_2) belong to the first group; these materials do not react with the components of the solder. Reactive particles, for example SnO_2 [6], belong to the second group. Theseparticles can react or dissolve in the solder. Thus, for the two groups a different effect can be observed in the wetting properties.

The wettability and spreading of the Sn3.5Ag0.7Cu-MWCNT (multi-walled carbon nanotube) and Sn-3.5Ag-0.7Cu-TiB_{2NPs}composite solders were investigated by Nai et al. [30]. They determined that the contact angle decreases as a function of increasing the amount of $TiB_{2\ NPS}$ in the solder. The composite solder can reach the minimum contact angle at 2 vol% $TiB_{2\ NPs}$ content. The viscosity of the solder is increased by a higher amount of $TiB_{2\ NPs}$, so the solder is not able to spread on the surface of the substrate, as seen also in Subsection 3.1 in connection with the CoNPs. This gives a higher contact angle.

The improvement of the wetting of the composite solder was observed with a small amount of other NPs, e.g. TiO_2 (minimum contact angle at 0.1 w% TiO_2[54]), Y_2O_3 (minimum contact angle at 1 w% Y_2O_3[55]) and Al_2O_3 (minimum contact angle at 0.5 w% Al_2O_3[56]).

4.2. The mechanical properties of solder-ceramic NP composites

Ceramic NPs, similar to metal particles, improve the mechanical properties of the composite solders. Gain et al. [47] observed that 0.5 w% ZrO_2 NPs can significantly improve the shear strength compared to solder without NPs. In addition, the reflow number causes only a small decline in the shear strength if the solder consists ofNPs compared to the solder without NPs. We can say from the data in Table 2 that the tensile strength of the composite solder is increased and its ductility is decreased by the addition of oxide NPsor CNTs.

Table 2

Mechanical properties of nanocomposite-SAC solder [57, 58]

Solder	Reinforcing phase	Mechanical properties	
		Tensile strength, R_m, MPa	Elongation, %
Sn3.0Ag0.5Cu	0.00 w%TiO_2	40.90	47.60
	0.25 w%TiO_2	45.80	46.10
	0.50 w%TiO_2	49.10	44.30
	0.75 w%TiO_2	53.00	41.40
	1.00 w%TiO_2	57.00	38.40
	1.25 w%TiO_2	56.00	33.70

Sn3.5Ag0.5Cu	0.00 w%Al_2O_3	54.30	49.20
	0.25 w% Al_2O_3	60.20	47.30
	0.50 w% Al_2O_3	62.40	44.00
	1.00 w% Al_2O_3	68.05	43.50
	1.50 w% Al_2O_3	70.05	32.50
Sn3.8Ag0.7Cu	0.00 w% SWCNT*	37.70	33.30
	0.01 w% SWCNT	40.90	32.70
	0.08 w% SWCNT	44.28	27.32
	0.10 w% SWCNT	48.60	26.57
	0.80 w% SWCNT	53.47	23.28
	1.00 w% SWCNT	56.70	24.36

*SWCNT: single-walled carbon nanotube

Summary

In accordance with European Union legislation lead and other critical alloying elements have to be removed and replaced by non-hazardous elements in the certain segments of the soldering technology. In the interest of achieving the mechanical and thermal properties of the tin-lead alloy, it isnecessary to use two, three or even more alloying elements in the newly developed lead-freesolder.

Several lead-free solders have a higher melting point than the melting temperature of the Sn-Pb alloys. The higher soldering temperature required achange in PCB from lower temperature to higher temperature resistant PCBs. This industrial problem (the change of the PCB) can be solved by using a solder paste made from metal NPs. Solder pastes from nano-sized alloy particles have a lower melting point than the bulk solder with same composition, and their temperature is equivalent to the melting point of the Sn-Pb alloys.

In the development of the solder, its mechanical properties are important because equipment with solder bondingis liable to mechanical stress, such as vibration, or shock caused by falling. The mechanical properties, hardness, tensile strength and shear strength can be improved by adding non-reactive NPs, e.g. Al_2O_3. Moreover, the presence of NPs in solder may decrease the IMClayer thickness on the solder/substrate interface.

Acknowledgement

The research work presented in this paper is based on the results achieved within the TÁMOP-4.2.1.B-10/2/KONV-2010-0001 project and carried out as part of the TÁMOP-4.2.2.A-11/1/KONV-2012-0019 project in the framework of the New Széchenyi Plan. The realisation of this project is supported by the European Union, and co-financed by the European Social Fund. The author was further supported by the János Bolyai Research Fellowship of the Hungarian Academy of Science.

The author is grateful to George Kaptay and Robin Lee Nagano for their advice.

References

[1] Loomans, M. E.–Vaynman, S.–Ghosh, G.–Fine, M. E.: *J Electron Mater,* 23, 1994, 741–746.

[2] Molnár A.–Kardos I.–Molnár I.–Gácsi Z.: *BKL. Kohászat,* 147, 2, 2014, 17–20 (in Hungarian).

[3] Yoon, J.-W.–Noh, B.-I.–Kim, B.-K.–Shur, C.-C.–Jung, S.-B.: *J Alloy Compd,* 486, 1–2, 2009, 142–147.

[4] Wang, L.–Yu, D. Q.–Zhao, J.–Huang, M. L.: *Mater Lett,* 56, 2002, 1039–1042.

[5] Bao, T. T.–Kim, Y.–Lee, J.–Lee, J. G.: *Mater Trans,* 51, 2010, 2145–2149.

[6] Zhang, L.–Tu, K. N.: *Mat Sci Eng R,* 82, 2014, 1–32.

[7] Chen, S.: *Thesis for the degree of licentiate of engineering.* Chalmers Univeristy of Technology, Göteborg, Sweden, 2013.

[8] Baumli, P.–Sytchev, J.–Kaptay, Gy.: *J Mater Sci,* 45, 2010, 5177–5190.

[9] Baumli, P.–Sychev, J.–Budai, I.–Szabo, J. T.–Kaptay, Gy.: *Composites A,* 44, 2013, 47–50.

[10] Han, Y. D.–Nai, S. M. L.–Jing, H. Y.–Xu, L. Y.–Tan, C. M.–Wei, J.: *J Mater Sci Mater Electron,* 22 (3), 2011, 315–322.

[11] Lekatou, A.–Karantzalis, E.–Evangelou, A.–Gousia, V.–Kaptay, Gy.–Gacsi, Z.–Baumli, P.–Simon, A.: *Mater Des,* 65, 2015 1121–1135.

[12] Shen, J.–Chan–Y. C.: *Microelectron Reliab,* 49, 2009, 223–234.

[13] Liu, J. P.–Guo, F.–Yan, Y. F.–Wang, W. B.–Shi, Y. W.: *J Electron Mater,* 33 (9), 2004, 958–963.

[14] Shi, Y.–Liu, J.–Yan, Y.–Xia, Z.–Lei, Y.–Guo, F.–Li, X.: *J Electron Mater,* 37 (4), 2008, 507–514.

[15] Hwang, S.-Y.–Lee, J.-W.–Lee, Z.-H.: *J Electron Mater,* 31 (11), 2002, 1304–1308.

[16] Kao, S.-T.–Lin, Y.-C.–Duh, J.-G.: *J Electron Mater,* 35 (3), 2006, 486–493.

[17] Shen, J.–Liu, Y. C.–Gao, H. X.: *J Mater Sci-Mater El,* 18 (4), 2007, 463–468.

[18] Lin, D.–Wang, G. X.–Srivatsan, T. S.–Al-Hajri, Meslet–Petraroli, M.: *Mater Lett,* 53, 2002, 333–338.

[19] Tai, F.–Guo, F.–Xia, Z.-D.–Lei, Y.-P.–Shi, Y.-W.: *Int J Min Met,* 16 (6), 2009, 677–684.

[20] Gain, A. Kumar–Fouzder, T.–Chan, Y. C.–Sharif, A.–Wong, N. B.–Yung, Winco K. C.: *J Alloy Compd,* 506, 2010, 216–223.

[21] Haseeb, A. S. M. A.–Leong, Y. M.–Arafat, M. M.: *Intermetallics,* 54, 2014, 86–94.

[22] Arafat, M. M.–Haseeb, A. S. M. A.–Johan, M. R.: *Solder Surf Mt Tech,* 23 (3), 2011, 140–149.

[23] Haseeb, A. S. M. A.–Arafat, M. M.–Johan, M. R.: *Mater Charact,* 64, 2012, 27–35.

[24] Haseeb, A. S. M. A.–Leng, T. S.: *Intermetallics,* 19, 2011, 707–712.

[25] Lee, J.-S.–Chu, K.-M.–Jeon, D. Y.–Patzelt, R.–Manessis, D.–Ostmann, A.: Electronic Components and Technology Conference. *Proceedings,* 2006, DOI: 10.1109/ECTC.2006.1645654

[26] Tay, S. L.–Haseeb, A. S. M. A.–Johan, M. R.–Munroe, P. R.–Quadir, M. Z.: *Intermetallics,* 33, 2013, 8–15.

[27] Shafiq, I.–Chan, Y. C.–Wong, N. B.–Yung, W. K. C.: *J Mater Sci-Mater El,* 23 (7), 2012, 1427–1434.

[28] Baumli P.–Vaskó G.–Laczkó S.–Sytcheva A.–Svéda M.: *BKL. Kohászat,* 147 (2), 2014, 21–25 (in Hungarian).

[29] Tay, S. L.–Haseeb, A. S. M. A.–Johan, Mohd Rafie: *Solder Surf Mt Tech,* 23 (1), 2011, 10–14.

[30] Nai, S. M. L.–Wei, J.–Gupta, M.: *Thin Solid Films,* 504 (1–2), 2006, 401–404.

[31] Jiang, H.–Moon, K.-S.–Hua, F.–Wong, C. P.: *Chem Mater,* 19 (18), 2007, 4482–4485.

[32] JIANG, H.–MOON, K.-S.–HUA, F.–WONG, C. P.: Electronic Components and Technology Conference. *Proceedings 57th*, 2007, 54–58. DOI: 10.1109/ECTC.2007.373776; ISSN: 0569-5503
[33] GAO, Y.–ZOU, C.–YANG, B.–ZHAI, Q.–LIU, J.–ZHURAVLEV, E.–SCHICK, C.: *J Alloys Compd,* 484, 2009, 777–781.
[34] ZOU, C.-D.–GAO, Y.–YANG, B.–ZHAI, Q.: *Trans. Nonferrous Met. Soc. China,* 20, 2010, 248−253.
[35] KAPTAY, Gy.: *J Mater Sci,* 47, 2012, 8320–8335.
[36] KAPTAY, Gy.–JANCZAK-RUSCH, J.–PIGOZZI, G.–JEURGENS, L. P. H.: *J Mater Eng Perform,* 23, 2014, 1600–1607.
[37] ZOU, C.-D.–GAO, Y.–YANG, B.–ZHAI, Q: *Mater Charact,* 61, 2010, 474–480.
[38] ABTEW, M.–SELVADURAY, G.: *Mat Sci Eng: R: Reports,* 27 (5–6), 2000, 95–141.
[39] LEE, J.-S.–CHU, K.-M.–PATZELT, R.–MANESSIS, D.–OSTMANN, A.–JEON, D. Y.: *Microelectron Eng,* 85, 2008, 1577–1583.
[40] GAIN, A. K.–CHAN, Y. C.–SHARIF, A.–WONG, N. B.–YUNG, W. K. C.: *Microelectron Reliab,* 49, 2009, 746–753.
[41] NIRANJANI, V. L.–RAO, B. S. S. Chandra–SARKAR, Rajdeep–KAMAT, S. V.: *J Alloy Compd,* 542, 2012, 136–141.
[42] LIN, D. C.–LIU, S.–GUO, T. M.–WANG, G. X.–SRIVATSAN, T. S.–PETRAROLI, M.: *MaterSci Eng A,* 360, 2003, 285–292.
[43] GAIN, A. K.–CHAN, Y. C.–YUNG, W. K. C.: *Microelectron Reliab,* 51, 2011, 975–984.
[44] CHANGS. Y.–JAIN, C. C.–CHUANG, T. H.–FENG, L. P.–TSAO, L. C.: *Mater Design,* 32, 2011, 4720–4727.
[45] CHUANG, T. H.–WU, M. W.–CHANG, S. Y.–PING, S. F.–TSAO, L. C.: *J Mater Sci-Mater El,* 22 (8), 2011, 1021–1027.
[46] CHANG, S. Y.–TSAO, L. C.–WU, M. W.–CHEN, C. W.: *J Mater Sci-Mater El,* 23 (1), 2012, 100–107.
[47] GAIN, A. K.–CHAN, Y. C.–YUNG, W. K. C.: *Microelectron Reliab,* 51, 2011, 2306–2313.
[48] CHELLVARAJOO, S.–ABDULLAH, M. Z.–SAMSUDIN, Z.: *Mater Design,* 67, 2015, 197–208.
[49] EL-DALY, A. A.–AL-GANAINY, G. S.–FAWZY, A.–YOUNIS, M. J.: *Mater Design,* 55, 2014, 837–845.
[50] LIU, P.–YAO, P.–LIU, J.: *J Electron Mater,* 37 (6), 2008, 874–879.
[51] SHEN, J.–PENG, C.–YIN, H. G.–CHEN, J.: *J Mater Sci-Mater El,* 23 (9), 2012, 1640–1646.
[52] BUKAT, K.–SITEK, J.–KOSCIELSKI, M.–JAKUBOWSKA, M.–SLOMA, M.–MLOZNIAK, A.–NIEDZWIEDZ, W.: *Solder Surf Mt Tech,* 24 (4), 2012, 267–279.
[53] HE, P.–LÜ, X.-C.–LIN, T.-S.–LI, H.-X.–An, J.–MA, X.–FENG, J.-C.–ZHANG, Y.–LI, Q.–QIAN, Y.-Y.: *Trans Nonferrous Met Soc China,* 22, 2012, 692−696.
[54] TANG, Y.–PAN, Y. C.–LI, G. Y.: *J Mater Sci-Mater El,* 24 (5), 2013, 1587–1594.
[55] LIU, X. Y.–HUANG, M. L.–WU, C. M. L.–WANG, L.: *J Mater Sci-Mater El,* 21 (10), 2010, 1046–1054.
[56] TSAO, L. C.–CHANG, S. Y.–LEE, C. I.–SUN, W. H.–HUANG, C. H.: *Mater Design,* 31 (10), 2010, 4831–4835.
[57] FU, S.-M.: *Master Thesis.* China, 2012.
[58] TSAO, L. C.: *Corrosion Resistance.* Book chapter. 2012, 107–132.

Materials Science and Engineering, Volume 40, No. 1 (2015) pp. 50–55.

VERTICAL SECTIONS IN THE CALCULATED TERNARY PHASE DIAGRAMS BETWEEN FOUR TIN-SILVER-COPPER SOLDERING ALLOYS AND PURE COPPER

ANDRÁS DEZSŐ[1]–GYÖRGY KAPTAY[2]

The Sn-Ag-Cu (SAC) solder alloys are used most frequently in the electronic industry to replace the traditional Sn-Pb eutectic solder. In the present paper, the vertical sections of the ternary phase diagram between four commercial solder alloys (SAC105, SAC205, SAC305 and SAC405) and pure Cu will be calculated using the Thermo-Calc software and its databank. For this purpose, a general material balance equation was derived for the A-B-C / C type vertical sections. The results of calculation can be used to understand the processes taking place when solid copper is soldered and is partially dissolved in the liquid solder alloy.
Keywords: lead-free soldering, SAC, copper dissolution, vertical section

Introduction

Lead-free soldering is a hot subject of investigations [1–11]. It is known that copper is partially dissolved in tin-based liquid solder alloys during soldering [8], leading to the necessity of re-processing the contaminated solder alloy [12–14]. In order to understand and control the process of this dissolution, vertical sections of the corresponding Sn-Ag-CU phase diagram should be constructed. As the Sn-Ag-Cu (SAC) solders are most frequently used in the electronic industry, the Sn-Ag-Cu / Cu calculated vertical sections are describedin this paper for the four industrial solder alloys SACX05 (X = 1, 2, 3, 4).

The calculations have been performed using the Thermo-Calc software and its corresponding databank [15]. To calculate quasi-binary sections of ternary alloys by this software, the user should first create the appropriate materialbalance equation. Therefore, this equation has been derived first, corresponding to the above formulated task.

1.Derivation of the general materials balance equation

Let us consider an $A_aB_bC_c$ / C vertical section of a ternary A-B-C system, where a, b and c are mass fractions of the components of the initial ternary solder alloy, connected as:

$$a + b + c = 1 \tag{1}$$

The following general material balance equation is built into the Thermo-Calc software:

$$\sum_i w_i = 1 \tag{2}$$

where w_i (dimensionless) are the mass fractions of components i (= A, B, C). If one wants to calculate the above vertical section using the Thermo-Calc software [15], the following

[1] University of Miskolc,Institute of Physical Metallurgy, Metalforming and Nanotechnology
Miskolc-Egyetemváros 3515, Hungary
dezsoa0318@freemail.hu
[2] Bay Zoltan Nonprofit Applied Research Ltd.
Miskolc 3519, Hungary
kaptay@hotmail.com

linear relationships should be also created between any two of the components of the ternary system, as an input information:

$$\alpha \cdot w_i + \beta \cdot w_j = \gamma \tag{3}$$

where *i* and *j* are any combination of the above components *A*, *B, C*, while the Greek letters denote numerical constants.Let us select components A and C for the purpose of Eq. (3).

The vertical ternary section will have temperature in itsy-axis and composition along its x-axis. This composition, denoted as *x*, will have a value of 0 at the $A_aB_bC_c$ corner and will have a value of 1 at the C corner. Then, the two materials balance equations are written as:

$$w_A = a \cdot (1 - x) \tag{4a}$$

$$w_C = c \cdot (1 - x) + x \tag{4b}$$

Now, let us express *x* from Eq. (4a) and let us substitute this equation in Eq. (4b) Finally, let us re-organize the resulting equation into the format of Eq. (3):

$$(1 - c) \cdot w_A + a \cdot w_C = a \tag{5}$$

This is the materials balance equation we are using to run the Thermo-Calc software. After this formula was used, the software calculated the chemical potential of the phases, and searched the phase equilibrium in the predefined intervals of temperature, and concentration. The data are from the software databank, and the calculation were made by numerical methods.

2. Calculations

The compositions of four, commercially available Sn-Ag-Cu solders are given in Table 1. As the sum of the concentrations in mass per cent of the three components Sn-Ag-Cu does not equal 100% in Table 1 (due to some contaminations), these values were normalized to 100% when coefficients *a* and *c* of Eq. (5) were calculated (A = Sn, C = Cu). This normalization brings us closer to reality, as the present calculation corresponds to the ternary Sn-Ag-Cu system. Parameters *a* and *c* of Table 1 were substituted into Eq. (5) and the corresponding results of calculations are shown in Figures 1–4 for the four solder alloys. In the top left corners of these diagrams the particular materials balance equations are given. The broken arrows added to the plots schematically indicate the processes, taking place during soldering. While the solder alloy is solid, no dissolution of Cu takes place. When the solder alloy becomes at least partly liquid, the dissolution of Cu starts, and it takes place till the final solidification takes place.

Table 1

Compositions of the four industrially important Sn-Ag-Cu solder alloys and the values of parameters a and c to be used in Eq. (5) to calculate the quasi-binary sections

Type	**Sn, w%**	**Ag w%**	**Cu w%**	***a***	***c***
SAC105	98.1	1.15	0.514	0.9833	0.0052
SAC205	96.4	2.21	0.511	0.9725	0.0052
SAC305	95.4	3.35	0.485	0.9613	0.0049
SAC405	94.9	4.28	0.536	0.9517	0.0054

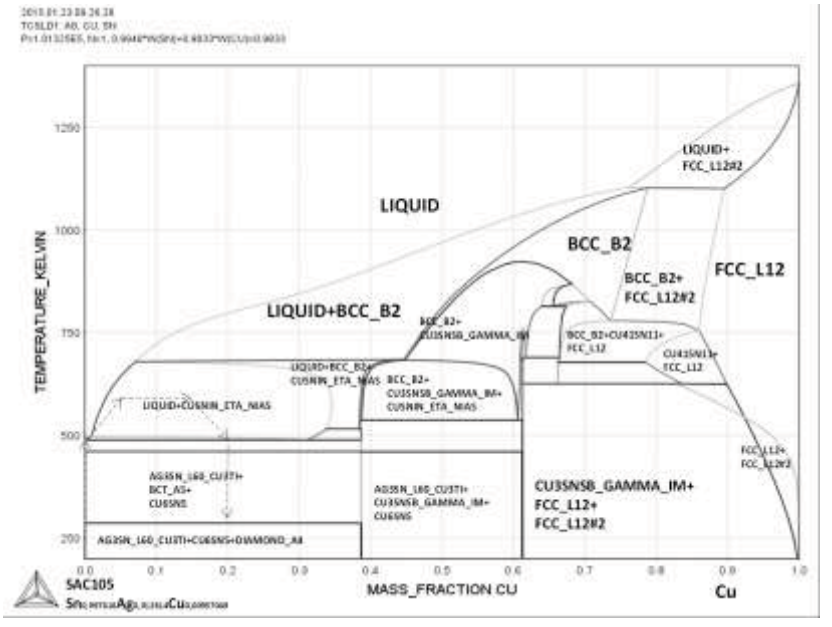

Figure 1. The SAC105 – Cu quasi-binary section of the Sn-Ag-Cu ternary phase diagram. Broken arrows show schematically the processes taking place during soldering

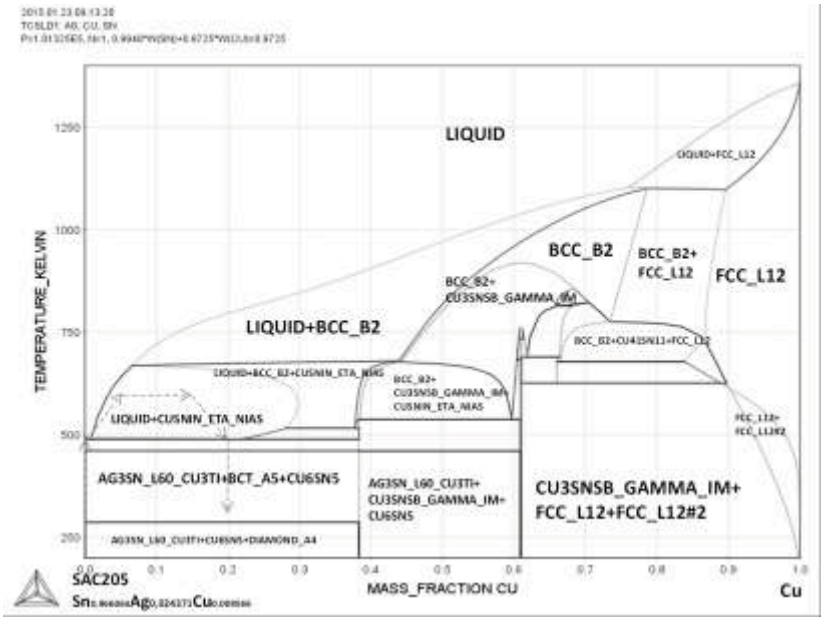

Figure 2. The SAC205 – Cu quasi-binary section of the Sn-Ag-Cu ternary phase diagram. Broken arrows show schematically the processes taking place during soldering

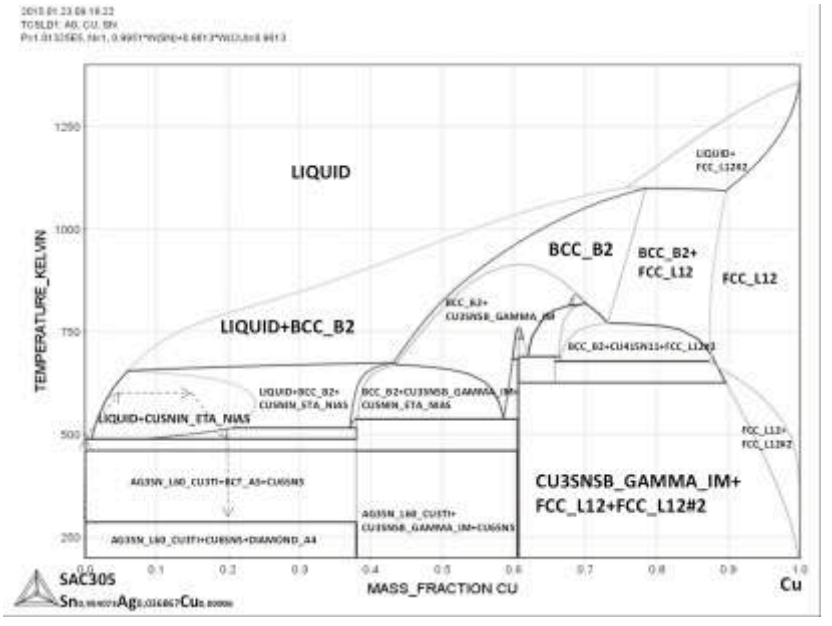

Figure 3. The SAC305 – Cu quasi-binary section of the Sn-Ag-Cu ternary phase diagram. Broken arrows show schematically the processes taking place during soldering

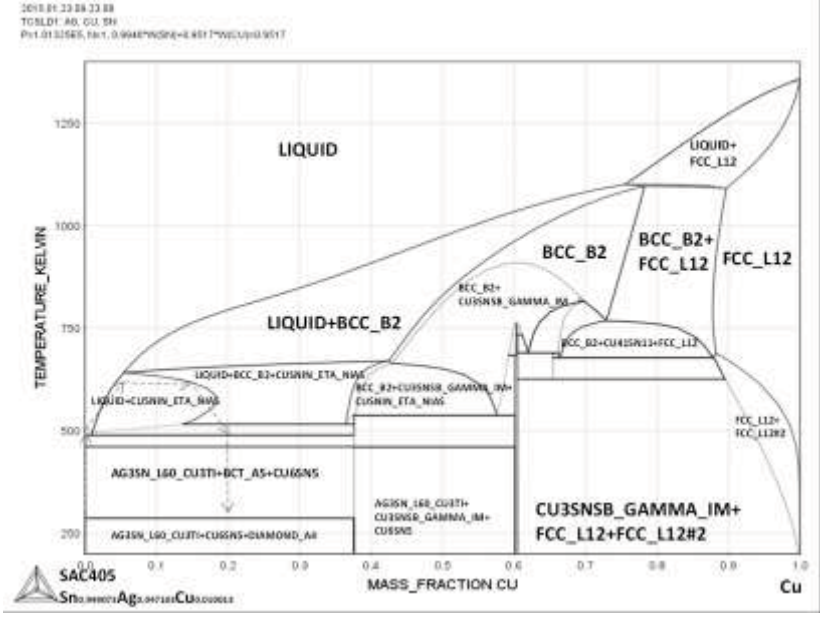

Figure 4. The SAC405 – Cu quasi-binary section of the Sn-Ag-Cu ternary phase diagram. Broken arrows show schematically the processes taking place during soldering

Comparing Figures 1–4, one can see the gradual evolution of the vertical sections of the Sn-Ag-Cu/Cu phase diagrams. The most important qualitative conclusion remains the same for all the four solder alloys: unless unreasonably long soldering time or too high soldering temperature is used (i.e. unless unreasonably lots of Cu is dissolved in the liquid solder), there will be the same three phases in the final solder: the bct Sn-rich phase (which might transform into the diamond structure at lower temperatures) + the Cu_6Sn_5 intermetallic phase (with some Ag dissolved in it) + the Ag_3Sn intermetallic phase (with some Cu dissolved in it). With Ag-content, soldering temperature and soldering time the ratios of these three phases will gradually change.

Conclusions

The quasi-binary SAC-Cu sections for 4 Sn-Ag-Cu solder alloys have been calculated in this paper, using a special materials balance equation (5) and the Thermo-Calc software. It is concluded that under normal industrial conditions there will be the same three phases in the final solder: the bct Sn-rich phase + the Cu_6Sn_5 intermetallic phase (with some Ag dissolved in it) + the Ag_3Sn intermetallic phase (with some Cu dissolved in it).

Acknowledgemenets

This work is based on the results achieved within the TÁMOP-4.2.1.B-10/2/KONV-2010-0001 project and carried out as part of the TÁMOP-4.2.2.A-11/1/KONV-2012-0019 project in the framework of the New Széchenyi Plan. The realization of this project is supported by the European Union, and co-financed by the European Social Fund. This work was partially carried out in the framework of the Center of Applied Materials Science and Nano-Technology at the University of Miskolc.

References

[1] Sycheva, A.–Radányi, Á.–Gácsi, Z.: Studying Pressure Induced Whiskers Formation from Sn-rich Surfaces. *Mat. Sci. Forum,* 790–791, 2014, 271–278.

[2] Baumli P.–Vaskó G.–Laczkó S.–Sytcheva, A.–Svéda M.: Ólommentes forraszanyagok nedvesítésvizsgálata: Sn-Ag/ Cu rendszer. *BKL. Kohászat*, 147 (2), 2014, 21–25.

[3] Tatárka, E.–Mende, T.–Roósz, A.: Liquidus temperature calculation in Sn-Bi-Cd system by Estphad method. *Mat. Sci. Forum,* 790–791, 2014, 265–270.

[4] Molnár, A.–Kardos, I.–Molnár, I.–Gácsi, Z.: Effect of Silver Content on the Properties of Lead-Free Solders. *Mater Sci Eng,* 39 (2), 2014, 51–58.

[5] Gyenes A.–Lanszki P.–Nagy E.–Gácsi Z.: Nikkellel mikroötvözött Sn-0,7Cu ólommentes forraszanyagok vizsgálata. *BKL. Kohászat*, 147 (2), 2014, 12–17.

[6] Koncz-Horváth, D.–Gácsi, Z.: Analysis of Lead in SnAg Based Solders Using X-ray Fluorescence. *Mat. Sci. Forum,* 752, 2013, 37–41.

[8] Dezső A.–Kaptay Gy.: Forraszanyagok térfogati éshatárfelületi egyensúlyának modellezése, *BKL,* 147 (2), 2014, 2–6.

[9] Rontó V.–Tranta F.–Svéda M.–Baumli P.–Czagány M.:Ólommentes forraszanyagok vizsgálata: Sn-Bi ötvözetek. *BKL,* 147 (2), 2014, 7–12.

[10] Török T.–Sós D.–Kun É.–Szabó M.–Hakl J.–Csík A.–Kövér L.–Glodán Gy.–Vad K.:Vékonybevonatos felület-előkezelések ólommentes önforrasztáshoz. *BKL,* 147 (2), 2014, 29–33.

[11] Svéda M.–Sycheva, A.–Kovács J.–Rónaföldi A.–Roósz A.: Forgó mágneses mező hatása a Sn-Cd peritektikus ötvözet kristályosodására függvényében. *BKL,* 147 (3), 2014, 45–48.

[12] Kulcsár T.–Kékesi T.: Az elektrolitos ónraffinálás kísérleti vizsgálata folyamatos technikával és az elektródfolyamatok értékelése. *BKL,* 147 (2), 2014, 47–52.

[13] TÓTH G. B.–UCHIKOSHI, M.–KÉKESI T.: Az ón katódos leválását befolyásoló polarizációs jellemzők potenciodinamikus vizsgálata sósavas önklorid oldatokban. *BKL,* 147 (2), 2014, 52–56.

[14] KULCSÁR, T.–DOBÓ, Zs.–KÉKESI, T.: The Effect of Micro-impulse Current on the Morphology of Tin Electrodeposited from Chloride Solutions. *Mat. Sci. Forum,* 752, 2013, 294–303.

[15] ANDERSSON, J.-O.–HELANDER, T.–HÖGLUND, L.–SHI, P.–SUNDMAN, B.: THERMO-CALC & DICTRA. *Computational Tools for Materials Science. Calphad,* Vol. 26, 2002, 273–312.

Materials Science and Engineering, Volume 40, No. 1 (2015) pp. 56–63.

TRIANGULAR AND SQUARE VOLTAGE WAVEFORMS IN WATER ELECTROLYSIS – INFLUENCE OF FREQUENCY AND AMPLITUDE CHANGE

ZSOLT DOBÓ[1]–ÁRPÁD BENCE PALOTÁS [2]

Alkaline water electrolysis is a traditional way of hydrogen generation. Water splitting via the use of direct current is a well-known process, however alternating, fluctuating or impulse current is one of the hot research topics today. Using direct current no gas release is observed on electrodes until voltages of 1.65–1.70 V are applied, but if the voltage between the electrodes is fluctuating, the average voltage can be less than the mentioned limit. The main goal of this study is to showhow the cell power, the generated gas flow rate and the efficiency is affected by fluctuating voltage around the 1.48 V isothermal operation. Square and triangular waveforms were applied to the cell with an average voltage of 1.5 V. The frequency and the amplitude of the waveforms was changed from 1 Hz to 99 Hz and from 0.1 V to 3.9 V with a resolution of 2 Hz and 0.2 V. Thus 2000 individual measurements were made by an automatic measurement system designed for the alkaline water splitting.
Keywords: water electrolysis, voltage waveform, electrolysis efficiency

Introduction

Hydrogen generation by water splitting theoretically requires potential difference of 1.23 V between the electrodes at temperature 298 K and ambient pressure (reversible voltage) [1, 2]. However, hydrogen generation using less than 1.48 V is possible only if heat is absorbed while heat must be supplied for the process to work above 1.48 V (thermoneutral voltage) [2, 3, 4]. The mentioned thresholds are temperature dependent (Figure 1) [4]. Practically no gas generation is observed until 1.65–1.70 V is applied, and the commercial water electrolyzers are operating with 1.8–2.6 V because of intentional overvoltages and the necessary ohmic losses [4, 5].

Efficiency of water electrolysis depends on many factors including the waveform of the applied voltage. Although there are several papers about applying impulse voltage or interrupted direct current to the cell [6, 7, 8, 9], some authors says that the amount of available papers in this area is low, and more experimental studies are required [10, 11], probably because of the following reason: the waveform parameters, such as frequency, amplitude, offset and waveform type can be varied almost independently over a very broad range [12].Our main goal is toselect a subset of the possible settings, and apply two different types of waveforms (square and triangular) to the cell at offset voltage 1.5 V (a value close to the thermoneutral voltage at normal temperature conditions) and to analyze the gas production, the electric power of the cell, and the efficiency of the electrolysis as a function of frequency and amplitude.

[1] University of Miskolc, Department of Combustion Technology and Thermal Energy
Miskolc-Egyetemváros 3515, Hungary
zsoltdobo@gmail.com
[2] University of Miskolc, Department of Combustion Technology and Thermal Energy
Miskolc-Egyetemváros 3515, Hungary
arpad.palotas@uni-miskolc.hu

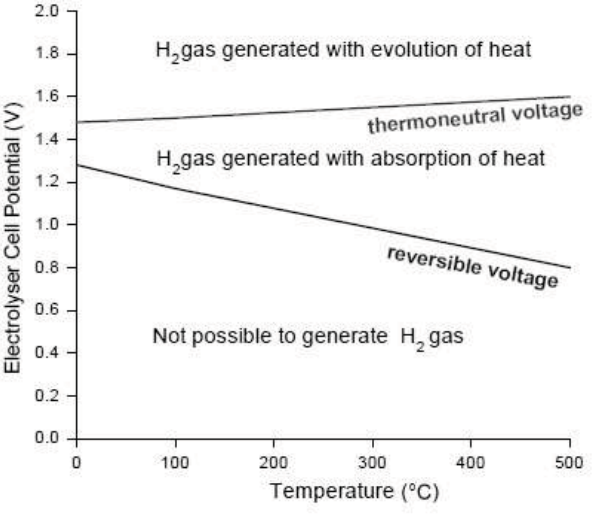

Figure 1. Hydrogen generation by water electrolysis as a function of temperature

1. Measurement system overview

Figure 2 illustrates the block diagram of the measurement system. The main component is the gas-tight cell powered by a special power supplythat is controlled by a dedicated National Instrumentsdevice (NI USB-6259). Its operation can be automated using a LabVIEW program. The device is responsible for measuring the cell voltage, the cell current and the pressure of the generated gas. It can alsocontrol the electric valve connected to the top of cell.

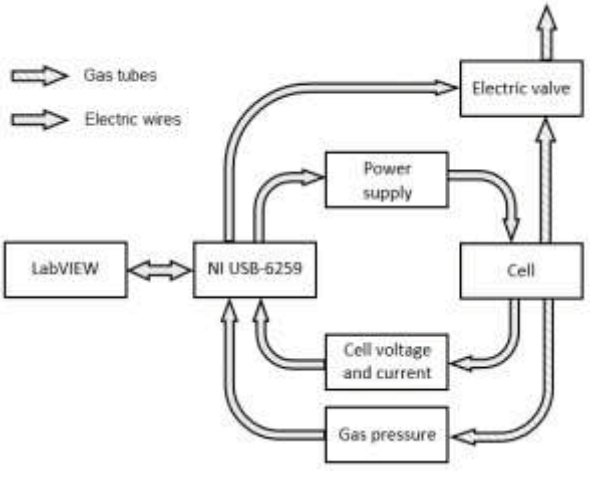

Figure 2. Block diagram of the measurement system

The measurement algorithm was the following:

A) initial parameters (voltage waveform) areset;
B) the actual waveform is applied to the cell for 15 s, while the cell voltage, cell current and the actual pressure of generated gasis recorded at a rate of 4000 samples/s;
C) data collection is stopped and the power supply is turned off;
D) system relax time for 5 s;
E) valve is opened for 4 s so that the produced gas can leave the cell and the pressure can come into equilibrium with the ambient;
F) valve is closed and the system paused for 1 s;
G) frequency and/or the amplitude is adjusted;
H) the procedure is repeated from step B until the system reaches the last frequency and amplitude setup.

The power supply can be operated between –10 V and +10 V. The maximum current is limited to 8 A, and the frequency limit is 50 kHz. The power supply can produce various waveforms within the limits. The frequency and the amplitude of the triangular and square waveforms were changed from 1 Hz to 99 Hz and 0.1 V to 3.9 V, respectively, with frequency resolution of 2 Hz and amplitude resolution of 0.2 V. Thus2000 individual measurement were performed.The measured data points were logged in separate files.Manual evaluationof each file would have been a long process, thus a special data estimator software was created in the programming language C#. The software computes the two main parameter of each measurement: the pressure and the cell power change with time. The velocity of increase in gas pressure is proportional to the gas flow rate. The exact ratio can be determined by calibration.

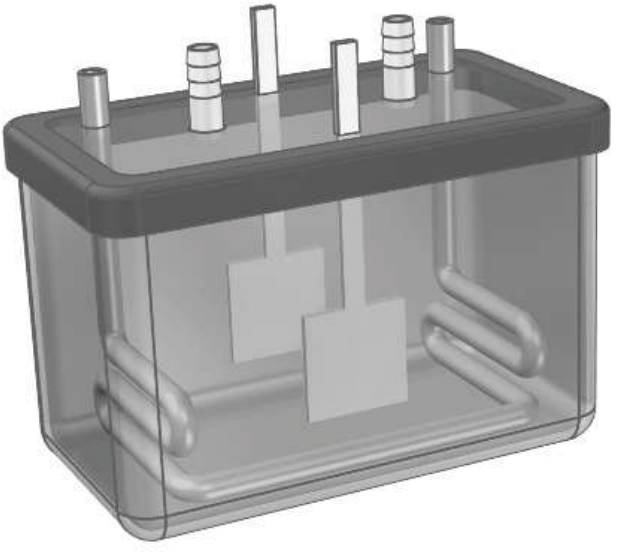

Figure 3. The cell used for water electrolysis

The sketch drawing of the cell is shown in Figure 3. The electrode was made of stainless steel with cross sections of 25 mm x 25 mm, and with thickness 1.5 mm (material type: 1.4307). The distance between electrodes was adjusted to 40 mm. 1 mol/l KOH solution was used as electrolyte with volume 500 ml. The cell contains two gas outlets. One of them was connected to pressure sensor (type: MPX5010DP), the other to an electrically controllable valve. The cell also contains a water-cooling circle in order to keep the electrolyte temperature at constant value. The temperature was measured by T-type thermocouple inserted into the electrolyte and connected to a temperature meter. The typical electrolyte temperature was 25 ±1 °C for each measurements.

2. Results

The generated gas flow rates as a function of frequency and amplitude are shown in Figure 4a (triangular waveform) and 4b (square waveform), respectively. The trends in both cases are similar: while the frequency increases or the amplitude decreases the gas flow rate decreases.The graphs also show, that by increasing the frequency the gas flow rate sooner or later reaches a frequency limit.Oncethe frequency is over the limit the gas flow rate equals to flow rate measured in DC case with the samevoltage as the waveform offset (while the power consumption is still increasing with increasing frequency).Because there was no gas flow at 1.5 VDC, the gas flow rate at frequencies greater than the frequency limit is also zero. The frequency limit depends on many factors, at least on amplitude, offset, and voltage waveform. The statement is supported by prior measurements at different offset voltages ranging from 1 V to 3.5 V.

Behaviour of the increasing amplitude is somewhat different. Above an amplitude limit the gas flow rate starts to increase, while the average voltage of the waveform is still 1.5 V. The smallest amplitude limit was at square waveform approximately0.7 V at frequency 1 Hz.

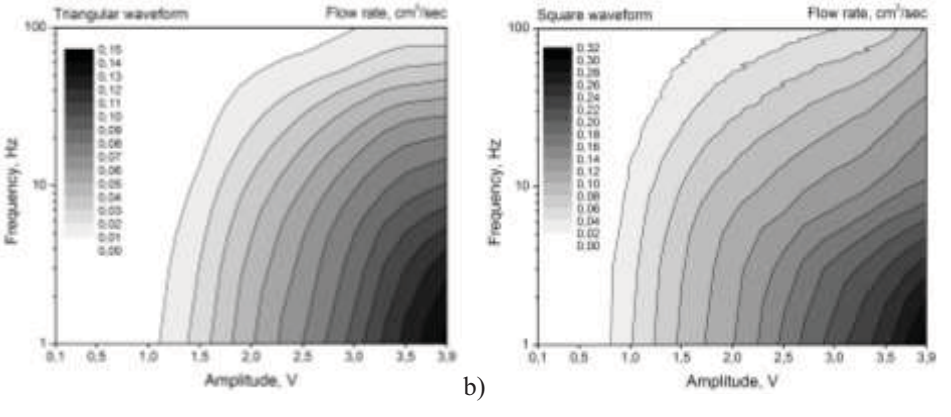

a) b)

Figure 4. Flow rates: Frequency and amplitude dependence for triangular and square waveforms

The square waveform generates at least 1.8 times more gas than the triangular waveform, but the exact square/triangular flow rate ratio depends on frequency and amplitude (Figure 5). The graph shows that the ratio is increasing while the amplitude is decreasing, and at low frequencies the difference between the ratios at various amplitudes is

smaller. The results shown on graph are polynomial type regressions on data points. The minimum value of the coefficient of regression (R^2) in each case is 0.97, the only exception is the 1.1 V line, where $R^2 = 0.88$.

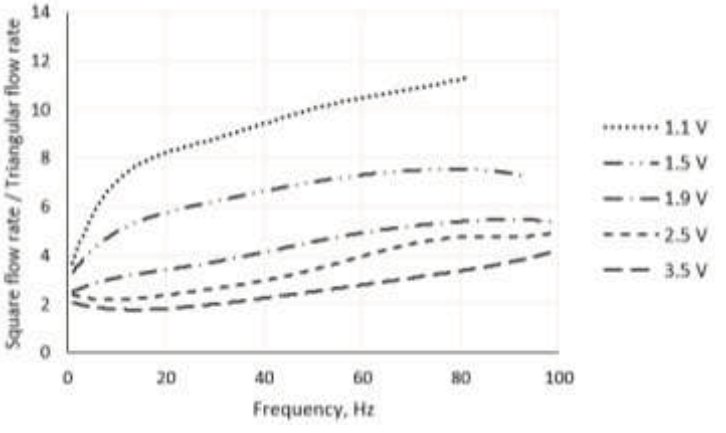

Figure 5. Square/Triangular flow rate ratio as a function of frequency and amplitude

Figure 6 illustrates the cell power as a function of frequency and amplitude using triangular and square waveforms, respectively.The results of both waveforms are similar: increasing the frequency and/or the amplitude also increases the cell power. However, the power measured with square waveform is much higher than the power measured with triangular waveform at the same settings.

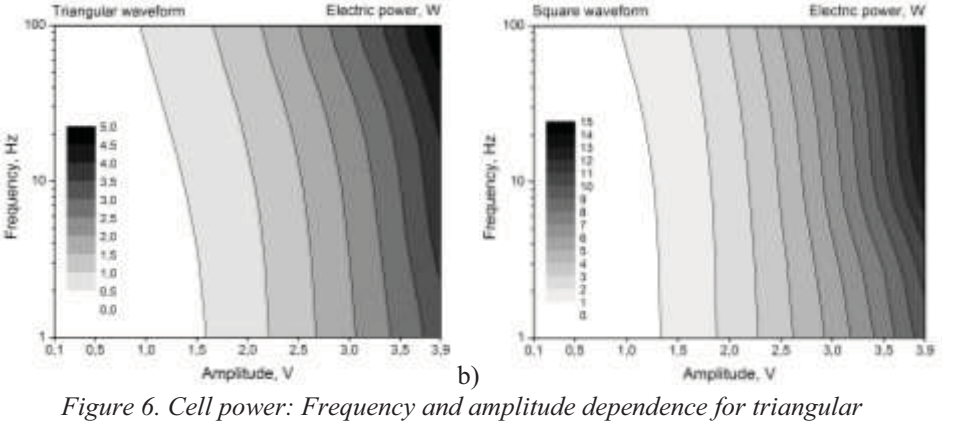

a) b)

Figure 6. Cell power: Frequency and amplitude dependence for triangular and square waveforms

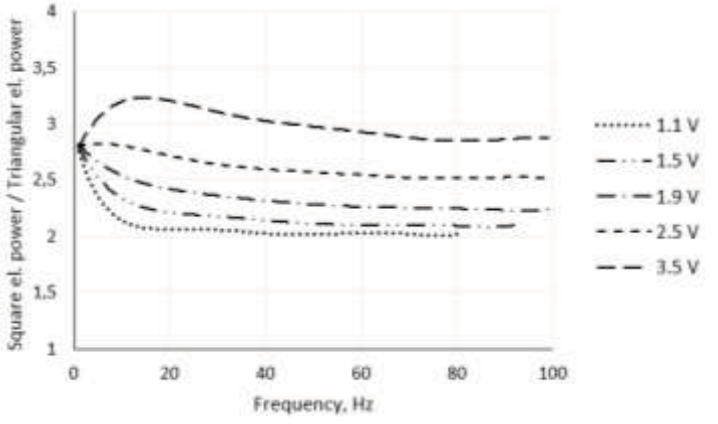

Figure 7. Square/Triangular power ratio as a function of frequency and amplitude

Figure 7 illustrates the exact square/triangular cell power ratio. The trends are somewhat different than the flow rate ratio. The curves on graph have a commonintersection at frequency 1 Hz and around ratio 2.8.

The cell efficiencies as a function of frequency and amplitude using triangular and square waveforms, respectively, are shown in Figure8. The efficiency was computed from flow rates and cell powers. Ideal gas flow rate (V_i) was calculated for each cell power values [5], and with the help of the real (measured) gas flow rate (V_m), the efficiency was calculated by the following equation [5]:

$$\eta = \frac{V_i}{V_m} \cdot 100$$

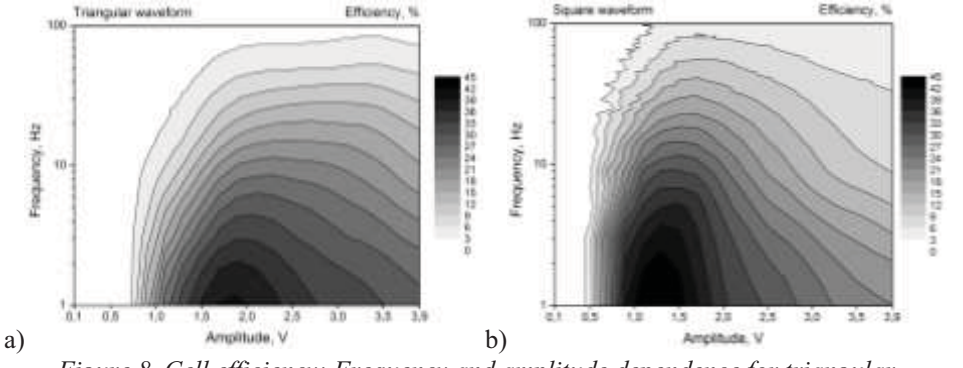

a) b)

Figure 8. Cell efficiency: Frequency and amplitude dependence for triangular and square waveforms

The maximum efficiency using square waveform was at amplitude 1.3 V while it was 1.8 V for triangular waveform. The figures show, that by applying 1.5 V DC (0 V amplitude would mean DC) to the cell the efficiency is practically zero, however with increasing the amplitude the efficiency starts to increase but bear in mind, that the average voltage (offset) is still 1.5 V. A value higher than 1.5 V in amplitude means, that the

polarity of the electrodes is always changing, but there are no obvious signs of this effect in efficiency, flow rate or cell power graphs.

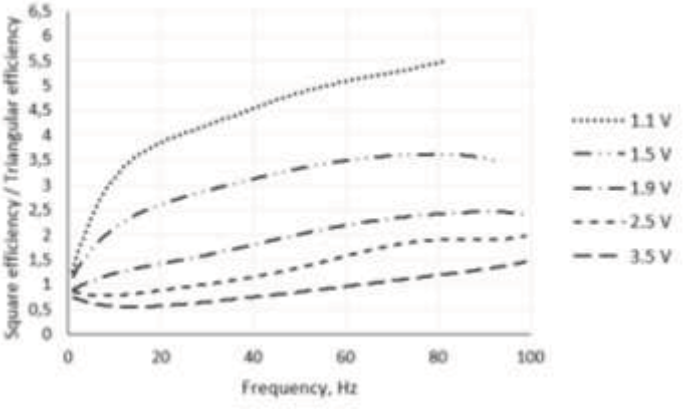

Figure 9. Square/Triangular efficiency ratio as a function of frequency and amplitude

Figure 9 illustrates the efficiency ratio of two waveforms. While the flow rate and cell power using square waveform was always greater, the efficiency ratio at some settings is less than 1. At high amplitude and low frequency settings the efficiency of water electrolysis is greater by applying triangular waveform to the cell, but at low amplitudes and high frequencies the square waveform is better.

Summary

The gas flow rate and the cell power of water electrolysiswere measured. Square and triangular waveforms at different frequencies and amplitudes were applied to the cell at a fixed 1.5 V offset. The efficiency of the system was computed from the gas flow rate and cell power.

It was shown that the produced H_2+O_2 gas flow rate is increasing with increasing amplitudes and decreasing frequencies. The maximum efficiency of the electrolysis process was found at the amplitude of 1.3 V for square and 1.8 V for triangular waveforms, both at 1 Hz frequency. Using the same frequency and amplitude setting at both waveforms, the absolute values of flow rates and cell powers differ significantly.

The high amount of individualdata required the development of an autonomous measurement system where the voltage, current and pressure in the cell are measured and registered according to the control algorithms.

Acknowledgement

This research was realized in the frames of TÁMOP 4.2.4. A/2-11-1-2012-0001 „National Excellence Program – Elaborating and operating an inland student and researcher personal support system convergence program" The project was subsidized by the European Union and co-financed by the European Social Fund. This research was carried out in the framework of the Center of Excellence of Sustainable Resource Management at the University of Miskolc.

References

[1] MARINI, Stafania–SALVI, Paolo–NELLI, Paolo–PESENTI, Rachele–VILLA, Marco–BERRETTONI, Mario–ZANGARI, Giovanni–KIROS, Yohannes: Avanced alkaline water electrolysis. *Electrochimica Acta,* 82, 2012, 384–391.

[2] NIKOLIC, Vladimir M.–TASIC, Gvozden S.–MAKSIC, Aleksandar D.–SAPONJIC, Djordje P. – MIULOVIC, Snezana M.–KANINSKI, Milica P. Marceta: Raising efficiency of hydrogen generation from alkaline water electrolysis – Energy saving. *International Journal of Hydrogen Energy,* 35, 2010, 12369–12373.

[3] ZENG, Kai–ZHANG, Dongke: Recent progress in alkaline water electrolysis for hydrogen production and applications. *Progress in Energy and Combustion Science,* 36, 2010, 307–326.

[4] VISWANATH, R. P.: A patent for generation of electrolytic hydrogen by a cost effective and cheaper route. *International Journal of Hydrogen Energy,* 29, 2010, 1191–1194.

[5] WANG, Mingyong–WANG, Zhi–GONG, Xuzhong–GUO, Zhancheng: The intensification technologies to water electrolysis for hydrogen production – A review. *Renewable and Sustainable Energy Reviews,* 29, 2014, 573–588.

[6] MAZLOOMI, Kaveh–SULAIMAN, Nasri–AHMAD, Siti Anom–YUNUS, Nurul Amziah Md.: Analysis of the frequency response of a water electrolysis cell. *International Journal of Electrochemical Science,* 8, 2013, 3731–3739.

[7] SHIMIZU, Naohiro–HOTTA, Souzaburo–SEKIYA, Takayuki–ODA, Osamu: A novel method of hydrogen generation by water electrolysis using an ultra-short-pulse power supply. *Journal of Applied Electrochemistry,* 36, 2006, 419–423.

[8] VANAGS, Martins–KLEPERIS, Janis–BAJARS, Gunars: *Water electrolysis with inductive voltage pulses*. *Electrolysis,* Chapter 2. Published by InTech, 2012.

[9] SHAABAN, Aly H.: *Pulsed DC and anode depolarization in water electrolysis for hydrogen generation*. HQ air force civil engineering support agency, final report, 1994.

[10] MAZLOOMI, S. K.–SULAIMAN, Nasri: Influencing factors of water electrolysis electrical efficiency. *Renewable and Sustainable Energy Reviews,* 16, 2012, 4257–4263.

[11] MAZLOOMI, Kaveh–SULAIMAN, Nasri–MOAYEDI, Hossein: Electrical efficiency of electrolytic hydrogen production. *International Journal of Electrochemical Science,* 7, 2012, 3314–3326.

[12] IBL, N.: Some theoretical aspects of pulse electrolysis. *Surface Technology,* 10, 1980, 81–104.

Materials Science and Engineering, Volume 40, No. 1 (2015) pp.64–74.

HYDROMETALLURGICAL PROCESSING OF ANODE SLIMES OBTAINED FROM THE ELECTROLYTIC REFINING OF SOLDERING SCRAP

ZOLTÁN HARANGI[1]–TIBOR KULCSÁR[2]–TAMÁS KÉKESI[3]

The anode slime generated as a by-product during the electrorefining of tin in hydrochloric acid solutions should be processed to recover the included tin, tin oxides and the alloying elements. The most frequently used lead-free soldering alloy contains significant amounts of silver and copper, which elements report to the slime. The metallic tin is leached with boiling hydrochloric acid, and the residue is digested in nitric acid. The leaching efficiency was examined as a function of time, temperature and liquid/solid ratio. It was found that more than 80% of the soluble tin content of the slime can be dissolved with ~ boiling 10M HCl in 4–5 hours in a reactor, while silver is retained, however copper also tends to dissolve with tin under these conditions. The remaining copper and all the silver was efficiently dissolved with boiling cc. HNO_3 in less than 2 hours. The obtained solutions are suitable for metal extraction by standard methods.
Keywords: anode slime, tin, hydrometallurgy, hydrochloric acid, leaching, extraction

Introduction

As the lead-free soldering alloys applied in the modern electronic industry tend to produce more dross during the wave soldering technology, the recycling of the included metallic values are becoming increasingly important. These alloys are more aggressive towards the copper material of the PCB (Printed Circuit Board) surface and also their oxidation resistance is lower. The most widely used type of such alloys are the SAC (Sn-Ag-Cu) materials, containing considerable amounts of silver, making the recovery even more imperative. During wave soldering, an oxidized dross is generated at the surface of the tin melt. It is removed periodically by skimming and it contains a large amount of entrapped metal. The metallic component can be separated by re-melting the primary dross and after skimming, the molten metal can be cast into anodes that are dissolved electrolytically. Recovery of pure tin from the electrolyte is achieved by cathodic reduction. Tin recovery is dictated by a high market price and a shrinking primary supply. Extensive investigations [1, 2] haveresulted in the development of a new technology [3] applying inexpensive and additive-free HCl-$SnCl_2$ electrolyte solutions combined with either current reversing (PCR) technology or some electromechanical system to compact the loosely deposited dendritic metal crystals at the cathode [4, 5]. Silver and copper, as more noble elements than tin, can also be separated efficiently by electrorefining, as they are accumulated undissolved at the surface of the cast anodes. A thick layer of slime is formed at the surface of the anode from the undissolved elements and particles of the tin based alloy and of some non-metallic

[1] University of Miskolc, Department of Chemical Metallurgy and Surface Technology
Miskolc-Egyetemváros 3515, Hungary
harangizoltan@gmail.com
[2] University of Miskolc, Department of Chemical Metallurgy and Surface Technology
Miskolc-Egyetemváros 3515, Hungary
kulcsar@uni-miskolc.hu
[3] University of Miskolc, Department of Chemical Metallurgy and Surface Technology
Miskolc-Egyetemváros 3515, Hungary
kekesi@uni-miskolc.hu

components. Avoiding vigorous agitation of the electrolyte, or even applying a diaphragm or an anode bag for physical separation, this layer of the argentiferous slime can be maintained undisturbed for a certain time, but it should be removed periodically as it may obstruct the process beyond a certain thickness. Due to its valuable components, it constitutes a valuable by-product, which needs processing to recover silver and tin, eliminating the residue from the main process of electrorefining at the same time.

Because of uneven anodic dissolution, a large amount of tin particles drops from the anode surface, thus the formed slime layer contains metallic tin, which can be dissolved in boiling and concentrated hydrochloric acid [1], although it may take considerable time. If conditions are oxidising, some copper may also be dissolved together with tin. This should be the first step of a hydrometallurgical processing of the slime. As silver ispractically not dissolved in this medium, tin can be leached from the residue with concentrated nitric acid. Some copper, which was not dissolved in the hydrochloric acid leaching step may also follow silver. The feasibility and the kinetic characteristicsof these leaching stepsneed to be investigated by the examination of the anodic slime structure and the fundamental behaviour in leaching.

1. Experimental procedure

The examined anode slime material was prepared by electrolytic refining of anodes cast from a tin alloy enriched in copper and silver by fractional crystallization of the ordinary Sn-Ag-Cu (SAC alloy) bath. The averagecomposition of the anode was 9% Cu, 3% Ag, the balance made up by tin. Electrolysis was carried out with 100, 500 and 1000 A/m^2 anodic current densities in stationary solutions of 1 M HCl and 10 g/dm^3 Sn. The electrolysis process, the produced anodic slime layer and the anode surface are illustrated by the pictures in Figure 1. The lowest current density experiment was carried out in a different cell of semi-industrial scale. The slime layer was removed from the anode surface by scraping, as shown in Figure 2a. The collected material was rinsed with water and dried at 110 ^{o}C in an oven, followed by fine grinding in an achat mortar (Figure 2b). In the main feasibility experiments, samples of the slime powder (20 g) were taken and mixed with usually 200 cm^3 hydrochloric acid of 10 mol/dm^3 concentration in a closed reactor vessel (Figure 2c) equipped with a water cooled reflow condenser (Figure 2d) to exhaust the evolved hydrogen gas.

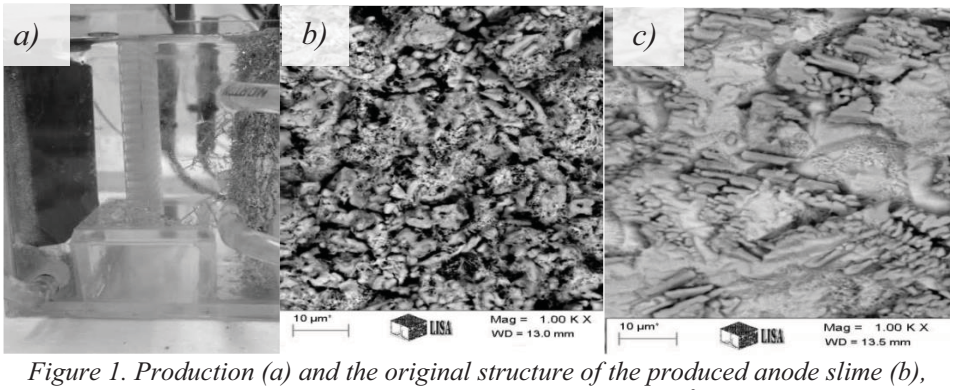

Figure 1. Production (a) and the original structure of the produced anode slime (b), on the metal substrate surface (c) (1000 A/m^2, 3h)

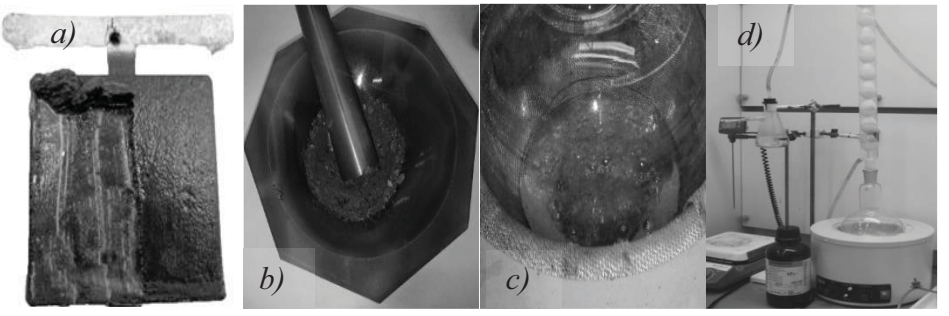

Figure 2. Anode slime removal (a), mortar (b), leaching (c), reactor(d)

For further testing, the ground powder was mixed with different volumes of 6M HCl and heated in a simple beaker placed on a hot plate (also seen in Figure 1d) where magnetic stirring was also applied. Solution samples of 1 cm^3 volume were taken regularly during the process of leaching. The analysis was carried out for Sn, Cu and Ag and some more common elements by Inductively Coupled Plasma Atomic Emission Spectrometry (ICP-AES). The duration of the leaching was longer than 8 hours with the closed reactor at boiling temperature (85~90 ºC). The additional experiments with the simple beaker lasted for 1.5 hours with 5, 10, 20 cm^3/g liquid-to-solid (L:S) ratios and for 8 hours with the standard 10:1 ratio.

The residual material obtained from the reactor after the long lasting hydrochloric acid leaching (obtained with the 10 M HCl lixiviant applied at boiling temperature with 10:1 L:S ratio) was removed and rinsed with water, dried and weighed. Small amounts (0.5 g) of this material were leached with 50 cm^3 nitric acid of 65% concentration by mass in a stirred beaker heated to 90–95 ºC temperature. This leaching step was continued for 2 hours, leaving virtually no residue in the beaker. Solutions samples were taken and analysed, as described above.

The dried anode slime and the residue from the first leaching step were examined by Scanning Electron Microscopy (SEM), Energy Dispersive X-Ray analysis (EDX) for the physical structure and the elemental distribution, and by X-Ray Diffraction (XRD) for the phase composition.

2. Experimental results and discussion

2.1. The structure of anode slime

Produced with 1000 A/m^2 anodic current density for 3 hours – while the cathodic deposition still remained of acceptable visual quality – is illustrated by the SEM images of the dried and ground powder sample in Figure 3. The residue of the anodic dissolution produced relatively large crystals of silver and copper, in virtually metallic forms, but the dispersed Sn-Ag, Sn-Cu or Sn-Cu-Ag intermetallics are also apparent. The relevant EDX spectra (Figure 4), clearly suggest the presence ofmetallic Ag and Cu particles. The XRD spectrum of the sample is presented in Figure 5, revealing the clearly identified intermetallic phases of Ag_4Sn, Cu_6Sn_5 and also metallic Cu.

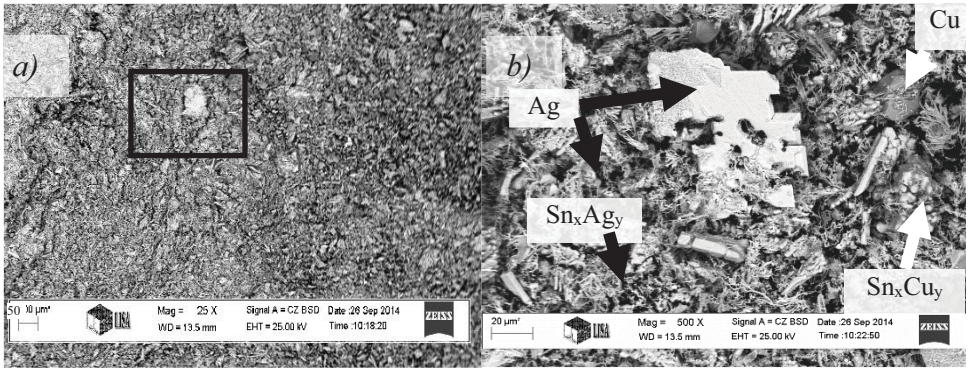

Figure 3. The SEM images of the dried and ground anode slime sample produced by an electrolysis of 3h with 1000 A/m^2, a)– low magnification, b)– high magnification of the marked area

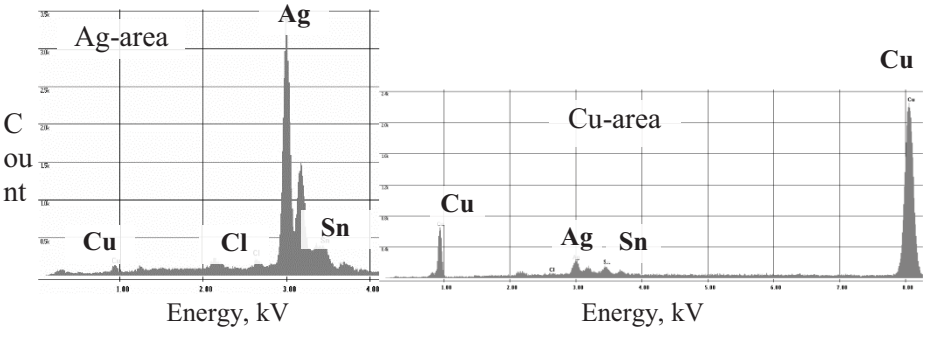

Figure 4. The characteristic EDX spectra of the anode slime produced in 3h with 1000 A/m^2

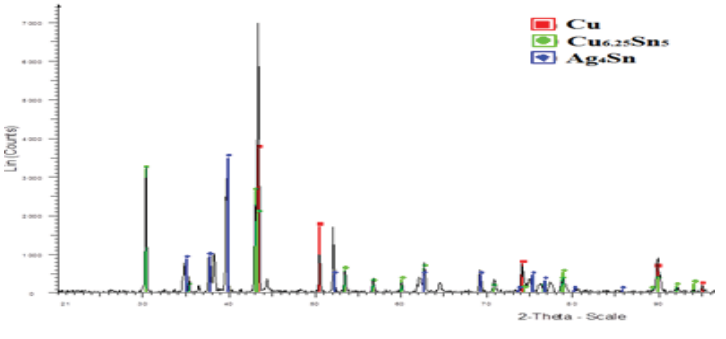

Figure 5 The XRD spectrum of the produced anode slime sample (3h electrolysis with 1000 A/m^2)

Similar results were obtained for the anode slime powders produced with 500 and 100 A/m^2 anodic current densities. Figure 6 shows the SEM images and the overall EDX spectrum for the slime powder obtained with 3h electrolysis applying 500 A/m^2 anodic current density.

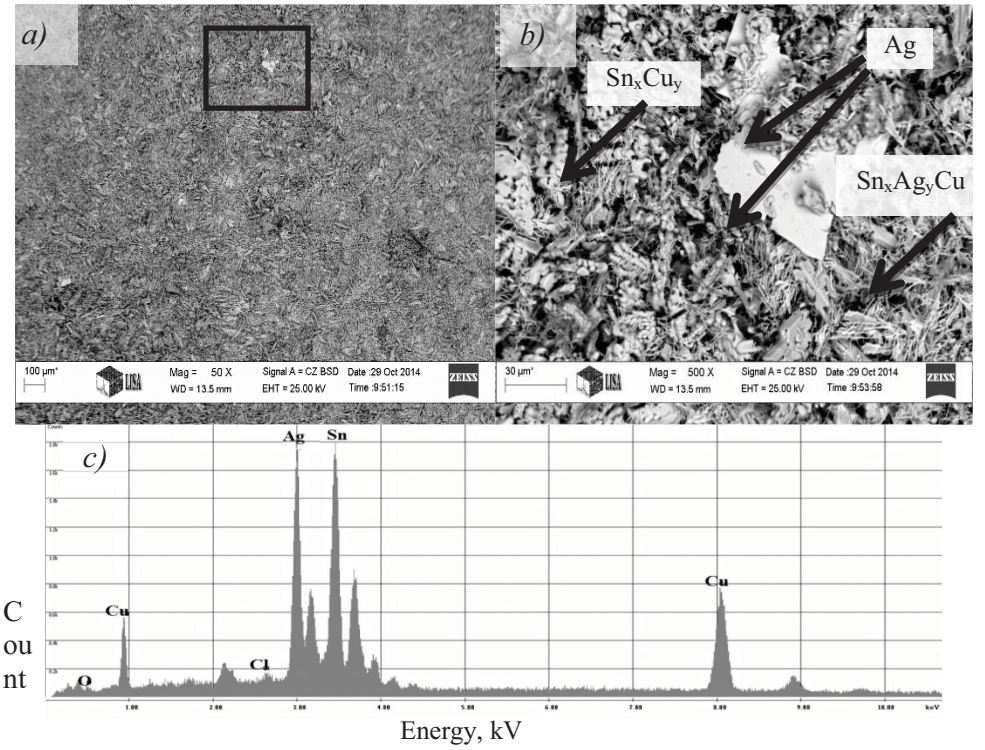

Figure 6 The SEM images and the overall EDX spectrum of the dried and ground anode slime sample produced in 3h electrolysis with 500 A/m^2, a) – low magnification, b) – high magnification of the marked area, c) – the characteristic EDX spectra of the examined area

The amount, the structure and the composition of the produced slime layer primarily depends on the type of the soldering alloy scrap refined, however it is also affected by the potential developing during the anodic dissolution. It is in direct correlation with the applied anodic current density and the average thickness of the slime layer impeding the free dissolution process. At lower currents the preferred crystallographic orientation will dissolve faster [6], thus rougher structures may develop. In this case, the impurities of higher electrode potential may be more efficiently retained in the metal matrix. At high current densities, on the other hand, the anodic overpotential will be higher, resulting in a more uniform dissolution pattern and more intensive drop out of metallic particles from the surface, causing higher rate of slime generation. At higher potentials the dissolution process may produce Sn(IV) ions primarily, which can react with the tin particles in the slime layer to form Sn(II) ions [1]. Thus the metallic tin concentration may decrease and the noble metal concentration increases. At low HCl concentrations, however, the Sn(IV) ions may lose their stability and cause $SnO_2 \cdot H_2O$ type precipitation to accumulate in the slime.

2.2. The leaching behaviour of the anode slime

Samples were examined in two steps. Application of hydrochloric acid at the first stage targeted the selective removal of the metallic tin component from the collected slime.The analysis of the anode slime samples obtained with different current densities is given in Table 1. The indicated values, however can be considered only approximate because of the difficulties caused by the refractory nature of the material. In order to analyse the powder, it needed a complex pre-treatment by digestion in aqua regia, followed by high temperature alkaline fusion of the residue with $KNaCO_3$ and $NaBO_4$ and a final dissolution in hydrochloric acid. The ICP analysis of the solution fractions needed a careful selection of the proper conditions. Despite all the precautions taken, some loss of components during these steps may have affected the results.

Table 1

Elemental analysis of the examined anode slime samples

Currentdensity, A/m^2	**Elementalanalysis, % (bymass)**								
	Ag	As	Bi	Fe	Ni	Pb	Sb	Cu	Sn
100*	3.36	0.0000	0.0086	0.2627	0.0002	0.0047	0.0096	34.21	46.10
500	6.15	0.0042	0.0005	0.0217	0.0075	0.0053	0.0265	25.5	43.74
1000	11.75	0.0025	0.0001	0.0096	0.0045	0.0062	0.0182	22.06	36.04

* Produced in a semi-industrial cell

Applying the analytical results of the slime samples and those of the solution samples taken during the leaching experiments, the relative masses of the dissolved metals could be determined. Figure 7 shows that tin may be dissolved to a great proportion from the anode slime with 10 M HCl in a reactor 4–5 hours boiling.

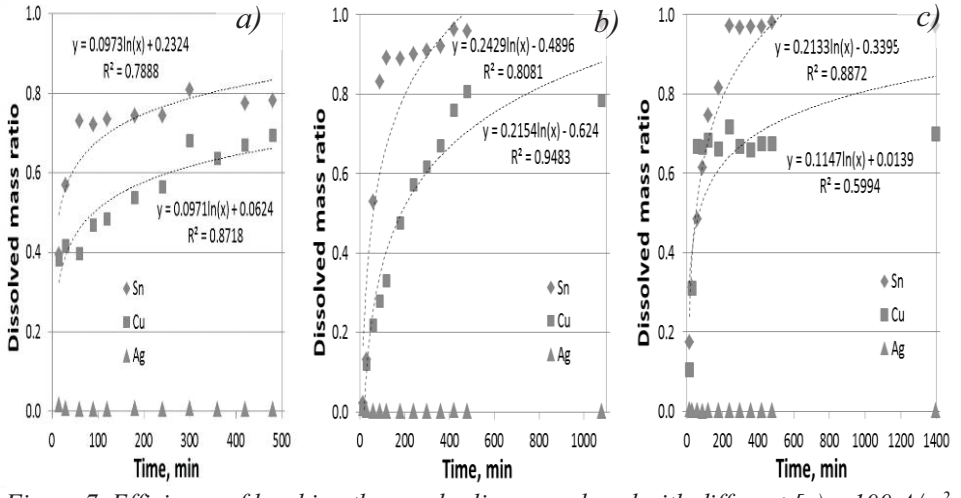

Figure 7. Efficiency of leaching the anode slimes produced with different [a) – 100 A/m^2, b) – 500 A/m^2, c) – 1000 A/m^2] current densities in 10 M boiling HCl

As the reaction vessel was not isolated from the ambient air, the dissolution of copper is also seen to take place to a similarly high degree. However, silver is virtually perfectly retained in the solid residue. Figure 8 shows that leaching in simple beakers – covered by watch-glasses – with the azeotropic concentration of HCl solution without intensive boiling can be also efficient for dissolving tin, but leaving most of the copper content behind undissolved.

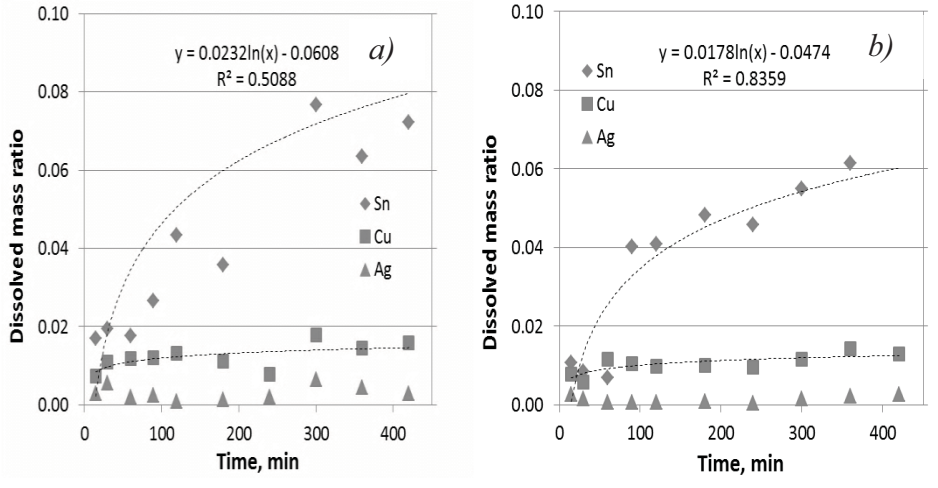

Figure 8. Efficiency of leaching the anode slimes produced with different [a)– 500 A/m^2, b)– 1000 A/m^2] current densities in 6 M HCl at 80 °C temperature in glass beakers

However, the efficiency of tin leaching is considerably lower as the HCl concentration is decreased from 10 to 6 mol/dm^3 and boiling is less vigorous. The effect of changing the liquid to solid ratio was also examined. For this purpose, relatively short experiments were carried out utilizing the glass beaker option. The results summarized in Figure 9 show that the L/S ratio in the 5–20 cm^3/mg range does not affect the leaching rate of tin, however the application of the lowest volume ratio may efficiently depress the dissolution of copper.

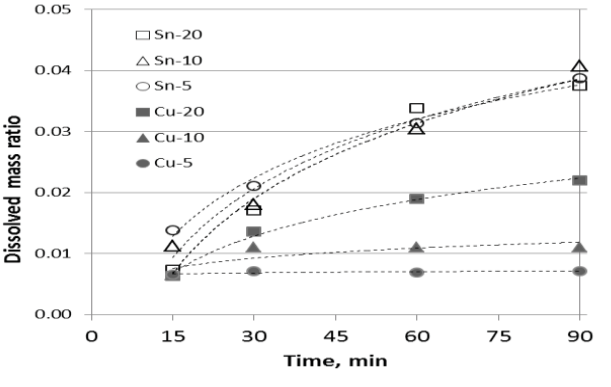

Figure 9. Efficiency of leaching the anode slimes – produced with 500 A/m^{2}current density – in 6 M HCl at 80 °C temperature in glass beakers with L/S ratio of 5, 10 and 20 cm^3/mg

The reaction depends on the exchange of electrons at the surface of the metal particles with hydrogen ions. Without any additional oxidising effect this process is impeded by the slightly negative electrode potential of tin and the high (approx. -0.75V at 1 mA/cm^2) overpotential of hydrogen on the tin surface [7]. This is slightly changed by the alloying elements. [8]. Still the component of the anode slime most soluble in HCl is tin. The higher rate of dissolution from the slime produced with higher current densities indicates that more metallic tin particles drop out from the surface of the anode during operation. As show in Table 1, increasing the current density gradually decreases the total tin concentration in the anode slime, proving the assumption that the enhanced generation of the Sn(IV) ions result in a more intensive reaction with the metallic tin particles as the ions are diffusing through the slime layer. Therefore more metallic tin is solubilized in a secondary process. The higher anode potential may also cause the formation of oxidised tin species, which – unless precipitation occurs because of dropping acid concentration in the cell – may readily dissolve in the subsequent leaching. The similar decrease in the copper concentration of the slime as the anodic current density is increased indicates that Sn(IV) ions may also react with the metallic copper content of the slime layer. As the solubility of silver is much lower and its redox potential is more positive, this affect is not seen in the silver concentration of the slimes. Rather, the higher rate of secondary dissolution of Sn and Cu causes higher silver concentrations in the slimes produced at higher current densities.

The residue of the slime produced with 500 A/m^2 anodic current density after the intensive 10M HCl leaching step in the reactor is shown by the SEM image and the corresponding EDX spectrum in Figure 10.

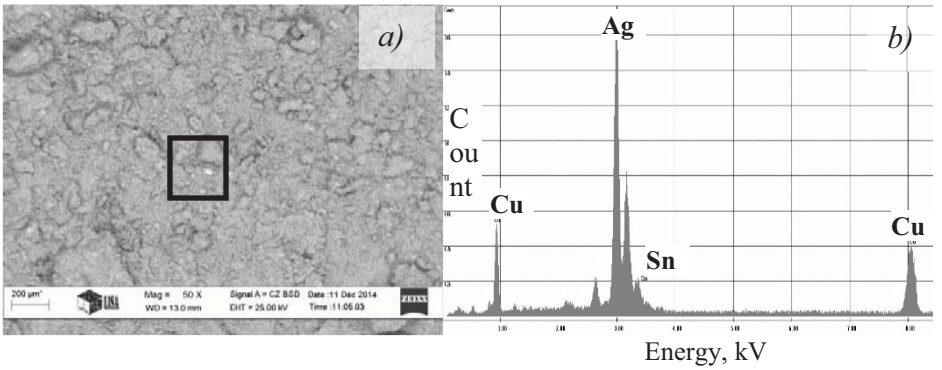

Figure 10. Solid residue of the anode slime – produced with 500 A/m^{2}current density – after boiling in 10 M HCl [a) – SEM image, b) – EDX spectrum]

As boiling 10 M HCl dissolves most of the tin component from the anode slime, the resistant silver can be liberated. A silver rich area – marked in Figure 10 – is shown in higher magnification in Figure 11. The large silver particle virtually corresponds to a similar one seen in the raw anode slime in Figures 3 and 6, however, the intensive leaching with boiling 10 M HCl has apparently converted the originally smooth surface into a porous structure by removing the soluble tin component from the agglomerate. The smaller crystals in the more heterogeneous looking surrounding area have also been transformed into a finer structure by the selective dissolution. While the leaching process with HCl is relatively slow even at high temperatures and high acid concentrations, the resulting porous structure will be advantageous for a faster reaction in the subsequent leaching step with nitric acid.

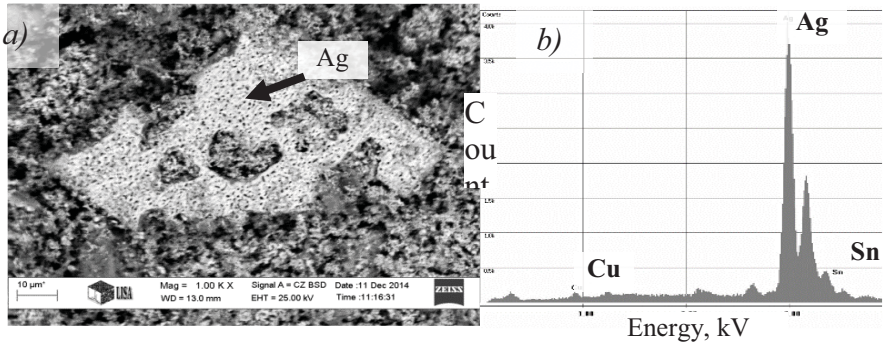

Figure 11. Magnified SEM image (a) and a relevant EDX spectrum (b) of the residue of the anode slime after intensive leaching with 10 M HCl

A similar picture is characteristic of the residue obtained from the slime produced with 1000 A/m^2 anodic current density after the HCl boiling step is shown by the SEM image and the corresponding EDX spectrum in Figure 12.

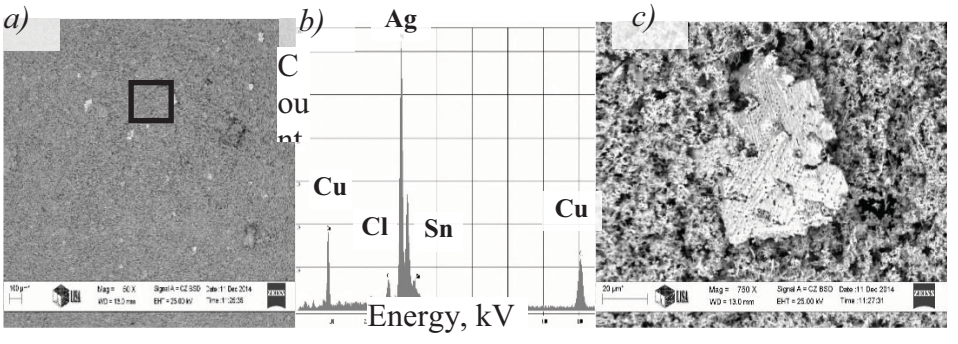

Figure 12. Solid residue of the anode slime – produced with 1000 A/m^{2}current density – after boiling in 10 M HCl [a) – SEM image, b) – EDX spectrum, magnified SEM image of the marked area]

After the more or less selective hydrochloric acid leaching, the residue is enriched in silver, which can be efficiently dissolved in hot and concentrated nitric acid. This reaction is relatively fast because the oxidising power of nitric acid enhances the rate of electron transfer from the metallic particles of large specific surface produced by the selective dissolution in the first leaching step. As the elemental analysis of this residue was even less reliable than that of the raw slime, the results of the nitric acid leaching (Figure 13) are given in terms of the dissolved masses of metals from the treated 0.5 g solid sample taken from the residue of the intensive HCl leaching in the reactor.

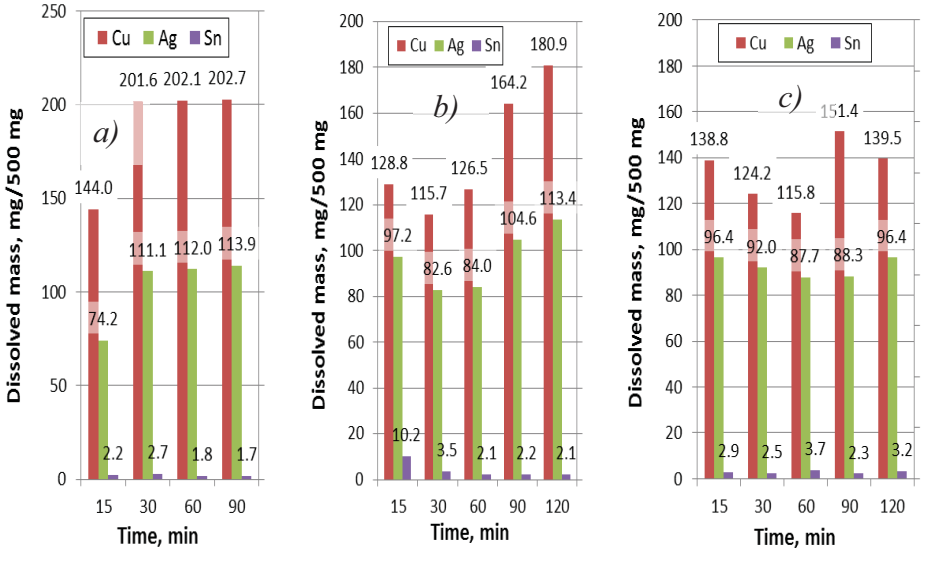

Figure 13. Digesting the HCl- leaching residuesof slimes produced with a) – 100 A/m², b) – 500 A/m², c) – 1000 A/m² current densities with hot cc. HNO_3

It can be seen that the tin and copper contents of the residues obtained from the high temperature 10M HCl leaching can be easily dissolved in hot and concentrated nitric acid. The lixiviated amounts of these metals are not increasing after the first 15 minutes of digestion in the reactor vessel. At the same time, the tin content of the residue from the HCl leaching is converted into a white $SnO_2 \cdot xH_2O$ type precipitate and virtually no tin is entering the strongly oxidizing hot nitric acid solution. Finally just a minor fraction of the original slime mass is collected as a refractory precipitate. Both the tin-chloride solution from the first leaching step and the silver-copper nitrate solution from the final digestion step can be used for metal extraction by standard techniques. For producing pure tin from the hydrochloric acid solution, it is necessary to use solution purification by selective sorption in an organic phase, like controlled anion exchange by a strongly basic resin [9], or selective precipitation. Controlled potential electrowinning may also be used for a preliminary removal of copper, followed by the cathodic deposition of pure tin [2]. The silver-copper nitrate solution can be processed by precipitating silver after the addition of sodiumchloride. Silver chloride can be converted into metallic silver by the commonly practiced methods. Copper from the residual nitrate solution can be electrodeposited.

Conclusions

The anode slime produced in the electrorefining of lead-free soldering tin alloy waste materials contain high amounts of tin and the alloying elements, most commonly silver and copper. The composition of the slime may slightly differ according to the current density applied in in the electrolysis utilizing the 1 M HCl – 10 g/dm³ Sn electrolyte solution earlier optimized for the electrorefining procedure. Hydrometallurgical processing of this secondary residue can be based on a two-step leaching process. The experimental results reveal that leaching with boiling 10 M HCl in a closed reactor is relatively efficient; however copper is significantly dissolved together with tin from the metallic components of

the slime. A close to 90% tin recovery can be achieved within 4–5 hours of leaching. To assure also selectivity in leaching tin from the anodic slime, it is advisable to use the moderately aggressive conditions of gentle boiling in 6 M HCl solution and applying a L/S ratio not higher than 5 cm^3/mg.While the relative amount of the applied HCl solution hardly affects the recovery of tin, it has a strong effect on the dissolution of copper. Any copper entering the hydrochloric solution together with tin should be removed by modern or conventional solution purification methods. It can be executed in a straightforward way by a selective deposition of copper by electrolysis or by cementation using tin particles. If tin is co-deposited, this by-product may still be useful to be applied in the foundry industry. The subsequent leaching step with hot concentrated nitric acid is efficient in dissolving silver and the remaining copper from the first residue. Separation of silver and copper fromthe nitric solution is straightforward by the chloride precipitation procedure. Reduction of silver chloride in aqueous media or decomposition at high temperature can result in the recovery of this valuable component. Recovery of tin from the chloride solution is possible by recently developed electrolytic processes. The final copper containing nitrate liquor can be decopperized by electrowinning. Thus the electrorefining of tin based lead-free soldering waste materials can be devised in an environmentally safe way leaving no secondary wastes behind.

Acknowledgement

The research work presented in this paper based on the results achieved in the Center of Applied Materials Science and Nano-Technology at the University of Miskolc and within the TÁMOP-4.2.2.A-11/1/KONV-2012-0019 project, and carried out as part of the TÁMOP-4.2.2.D-15/1/KONV-2015-0017 project in the framework of the New Széchenyi Plan. The realization of this project is supported by the European Union, and co-financed by the European Social Fund.

References

[1] RIMASZÉKI, G.–KULCSÁR, T.–KÉKESI, T.: Application of HCl solutions for recovering the high purity metal from tin scrap by electrorefining. *Hydrometallurgy,* 125–126, 2012, 55–63.

[2] RIMASZÉKI, G.–KULCSÁR, T.–KÉKESI, T.: Investigation and optimization of tin electrorefining in hydrochloric acid solutions. *J. Appl. Electrochem,* 42, 2012, 573–584.

[3] KÉKESI, T.: Electrorefining in aqueous chloride media for recovering tin from waste materials. *Acta Metallurgica Slovaca,* 19 (3), 2013, 196–205.

[4] KULCSÁR, T.–DOBÓ, ZS.–KÉKESI, T.: The Effect of Micro-impulse Current on the Morphology of Tin Electrode posited from Chloride Solutions. *Materials Science Forum,* 752, 2013, 294–303.

[5] DOBÓ, ZS.–KULCSÁR, T.–KÉKESI, T.: Electrorefining of tin in pure acid solutions by mechanically controlled cathode deposition and solar power utilization. *Materials Science & Engineering,* 37 (2), 2012, 19–26.

[6] WINAND, R.: Electrocrystallization. *Hydrometallurgy,* 29, 1992, 567–598.

[7] TALBOT, D.–TALBOT, J.: *Corrosion Science and Technology.* CRC Press LLC, Boca Raton, 1998.

[8] EZAKI, H.–MORINAGA, M.–WATANABE, S.: Hydrogen overpotential for transition metals and alloys, and its interpretation using an electronic model. *Electrochimica Acta,* 38 (4), 1993, 557–564.

[9] KÉKESI, T.–ISSHIKI, M.: Anion Exchange for the Ultra-High Purification of Transition Metals *Erzmetall,* 56 (2), 2003, 59–67.

Materials Science and Engineering, Volume 40, No. 1 (2015) pp. 75–87.

INVESTIGATION AND CHARACTERIZATION OF THE ANODIC AND CATHODIC PROCESSESOF TIN AND SN-AG-CU ALLOYS IN HCL SOLUTIONS

TIBOR KULCSÁR[1]–TAMÁS KÉKESI[2]

Lead-free wave soldering applied in modern electronic technology generates growing amounts of drosses containing high proportions of metallic tin, which is usually accompanied by several percentages of silver and copper. The proposed technology targets the extraction of pure tin from this valuable secondary raw material. Although electrorefining in dilute HCl media can offer great advantages, the process may be disturbed by the sensitivity of the anodic dissolution to the conditions and the dendrite formation at the cathode. In order to clarify the processes involved, the mass changes of the electrodes were monitored with high precision without interrupting the current. This technique revealed the disturbing effects caused by Sn(IV) species and the evolved hydrogen gas. Comparing the measured anode potentials to the calculated stability ranges of the Sn species, the practical limits of the anodic current density were estimated. Suitable conditions of anodic dissolution requires controlling the anode potential. The deposited tin is generally loose and dendritic in the entire range of the examined tin and HCl concentrations. However this difficulty can be practically overcome by a patented electromechanical system for compressing the cathodic deposit.
Keywords: tin recycling, soldering dross, electrorefining, hydrochloric acid, anode, cathode

Introduction

Most of the lead-free soldering materials applied in modern electronic industry are tin based alloys containing Ag andCu (SAC series), although Bi and Sb may also appear as added components [1, 2]. Applying the lead-free alloys in soldering or coating implies a higher rate of copper pick-up by the tin based molten metal bath unfortunately. Therefore, the dross collected regularly from the open surface contains an increased concentration of copper and the bath needs to be refreshed by adding copper-free tin-silver alloy material. In some technologies, the copper concentration of the removed material is even increased by the cooling and partial crystallization. No direct technology has been available for recycling these hazardous secondary tin alloy materials, thus long transportation and conventional tin metallurgy for the reclaiming of the valuable metallic components is currently the only available way of disposal. Electrorefining has also been applied to purify tin, but earlier technology implies special and expensive components in generally sulfuric acid solutions or the inconvenient use of alkaline media at high temperatures [3]. The common H_2SO_4 media imply the difficulties of solution stability, cathode morphology and purity [4]. Pure tin can be recovered directly from soldering waste by electrorefining in a $SnCl_2$-HCl media [5, 6].

There have been two major difficulties related to the electrorefining of tin in pure acidic aqueous solutions. One of them is the inherently dendritic morphology of the tin crystals deposited at the cathode surface and the other is providing the optimum conditions for the

[1] University of Miskolc, Department of Chemical Metallurgy and Surface Technology
Miskolc-Egyetemváros 3515, Hungary
kulcsar@uni-miskolc.hu
[2] University of Miskolc, Department of Chemical Metallurgy and Surface Technology
Miskolc-Egyetemváros 3515, Hungary
kekesi@uni-miskolc.hu

dissolution of the anode [5, 6]. As the tin deposition is generally characterized by the formation of long dendrites [7], the rate at which diffusion can supply the ions to the ideally smooth cathode surface must be considerably lower than the rate of charge transfer. Therefore, forced convection should be useful in assuring better deposit morphology and also the required high efficiency of purification. However, efficient solution agitation at the surface of the electrode is difficult and it may disturb the stability of the formed anode slime layer and disperse unwanted particles in the electrolyte. Another way to tackle this difficulty is the application of periodically reversed or interrupted current, or electrodeposition with micro-scale current impulses. Although these techniques have been proved [7] to influence beneficially the crystal form, an adequately dense cathode deposit could only be achieved by mechanical compression [7, 8].

The difficulty of stabilizing the anode processes is caused by the generation of Sn(IV) species instead of the preferred divalent ions of tin. In this case secondary chemical reactions may occur, thus efficiency and stability characteristics of the electrolysis may be impaired. The deposited cathode crystals may be attacked by the reaction:

$$\mathrm{Sn(IV) + Sn = 2\ Sn(II)} \tag{1}$$

causing re-dissolution of tin already deposited and deterioration of the crystal structure. The chloride medium even enhances this reaction, as it is proven by the results of thermodynamic simulation [5]. In chloride solutions, chloro-complex ions take part, therefore the general form of reaction (1) can be specified according to the following equation:

$$\left[\mathrm{SnCl}_y\right]^{4-y} + \mathrm{Sn} + (2\mathrm{x} - \mathrm{y})\mathrm{Cl}^- = 2[\mathrm{SnCl}_x]^{2-x} \tag{2}$$

As the finest tin crystals are re-dissolved, the cathode loses active surface area and the local current density may increase, resulting in hydrogen evolution. Consequently the acid concentration may drop in such regions and the tetravalent tin ions may start precipitating by hydrolysis. Although in the fresh electrolyte solutions prepared by dissolving metal particles in cc. HCl [5], tin is present in the Sn(II) form, Sn (IV) may arise either because of oxidizing effects from the ambient air or by the irregular conditions of the anode. The former is expressed by the reaction with oxygen:

$$[\mathrm{SnCl}_x]^{2-x} + \frac{1}{2}\mathrm{O}_2 + 2\mathrm{H}^+ + (y - x)\mathrm{Cl}^- = \left[\mathrm{SnCl}_y\right]^{4-y} + \mathrm{H}_2\mathrm{O} \tag{3}$$

which is driven by a high thermodynamic force [5]. The precipitation of Sn(IV) species by hydrolysis may cause turbidity. As the HCl concentration drops considerably below 1 mol/dm^3 under oxidizing conditions, the formation of hydrated tin-dioxide particles may eventually break up the electrolyte. However, Cl^- activity by forming $[SnCl_x]^{y-}$ complexes [9, 10] may stabilize the dissolved tin. The redox potential (E) diagrams as functions of the pH or the pCl^- values in Figure 1*a* and 1*b* show increased stability areas of the Sn(II) and Sn(IV) species in the chloride system compared to the common Sn-H_2O system.

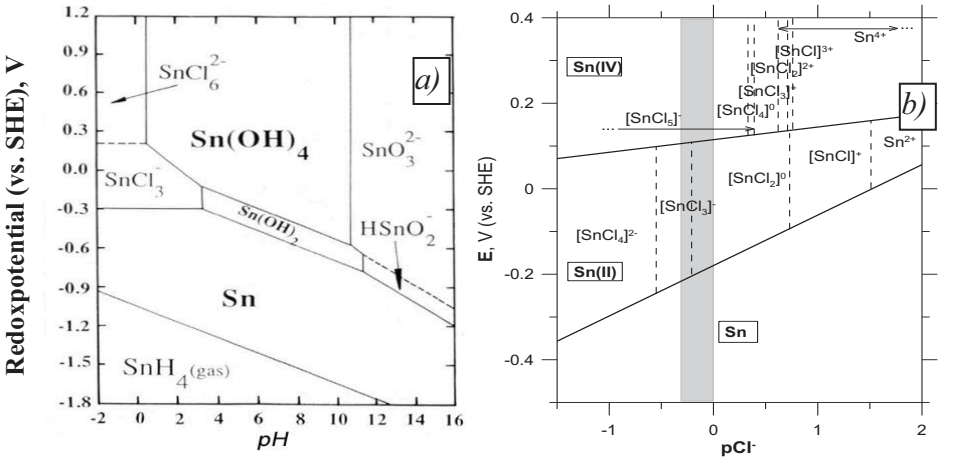

Figure 1. Potential – pH diagrams in the Sn-H_2O-Cl system [11] *(a) and the potential-pCl^- diagram (b) constructed from the stability constants and the standard potentials (25 °C)*

Another source of the generated Sn(IV) species is the anode itself. As shown in Figure 1*b*, when the potential is higher than the values of the line separating the predominance areas of the Sn(IV) and Sn(II) species in the actual range of HCl concentration marked by the gray area, the anodic dissolution may produce dominantly Sn(IV) species. With the control of the anodic potential, and the corresponding limiting of the anodic current density, the increase of the Sn(IV) concentration can be avoided. However, when the anode is covered with a growing slime layer, maintaining the required current density may imply high anode potentials. As the anode slime containsa high proportion (~50%) of solid tin particles, the anodic process may also be considered involving two consecutive steps. At higher potentials, Sn(IV) ions may be generated primarily, but as they diffuse through the slime layer, they get into contact with the tin particles and Sn(II) may finally arise by reaction (1). However, if the anode slime layer is still thin or loose, the Sn(IV) ions may enter the bulk of the electrolyte. They can also be generated there by reaction (3) if the electrolyte solution is not isolated from the ambient air. As Sn(IV) species reach the cathode of large specific surface area, reaction (1) can significantly reduce the net production of the metal. The origin of the Sn(IV) ions may be indicated by the change in the overall Sn concentration during electrorefining. The major impurities, silver and copper, are virtually indifferent in the anode and retained undissolved in the anode slime. The rest of the practical impurities usually have more negative standard electrode potentials than that of tin, so they may also take part in the anodic process and accumulate in the electrolyte, but they are generally present only in negligible amounts. Thus the change in the bulk tin concentration can be caused by two major effects: (i) oxidation of dissolved Sn(II) species to the Sn(IV) state by air and their reaction with the metal deposited at the cathode; or (ii) hydrogen evolution because of the shortage of available tin ions at the cathode surface at polarized cathode potentials. These effects may both increase the tin concentration in the solution.

The main dangers to the proper operation of the electrolysis are rooted in the conditions of the anode. Its effects are however also detectable in the composition of the electrolyte solution and in the cathodic morphology and current efficiency. The mass changes of the electrodes recorded continuously during the electrolysis may help understand the processes.

1. Experimental procedure

The raw materials for the anodes were selected according to practical reasons. The compositions of the SAC type soldering alloys generally used by the large electronic companies also in Hungary are characterized by a silver concentration of 2.5–4% and a copper content of 0.1–0.9% some producers may apply a metallurgical treatment to their soldering dross. By cooling the spent soldering bath to low temperatures much of the original copper content can be removed by fractional crystallization. In this way the secondary dross – purchased by the scrap collectors – may reach as high levels as 9–10%. Therefore we have examined the behavior of tin alloys representing a large variety in the SAC group: Sn999, SnCu1, $SnCu_9Ag_3$, $SnAg_3$.The compositions of the examined electrolytes were5, 10, 20and 40 g/dm^{3}Sn and 1 mol/dm^{3}HCl. The elemental compositionsof the anode materials are given in Table 1. Cathodes were cast from pure tin.

Table 1

Compositions of the tested anode materials

Anode	Ag	Al	Cu	Fe	Ni	Pb	Sb	Zn	Sn
Sn 99.9	0,009	<0,01	0,003	0,004	<0,0005	0,001	0,002	0,003	99,97
SnCu1	0,028	0,246	**1,061**	0,0183	0,001	0,002	0,001	0,002	98,62
SnAg3	**3,34**	0,205	0,152	0,021	0,0014	<0,002	0,005	0,007	96,25
SnCu9Ag3	**2,83**	0,01	**9,04**	0,011	0,0038	0,001	0,0017	0,008	86,42

The experimental system capable of in-situ recording of the mass changes of the electrodes is shown in Figure 2.The electrode (of 6X6 cm active surface area) was hungon a positioning adapter with a thin polyamide thread. The current is conducted by a thin flexible cable, so as not to interfere with the mass measurement. The data acquisition system was designed to record beside the actual mass readings the detected values of the current, the cell voltage, the electrode potential vs. a calomel reference electrode. This set-up was used for short term measurements (5 min) with fresh electrodes. For testing the behavior of the cell on a longer run, the in-situ mass measurement was not used, because for longer runs some mechanical intervention was needed to prevent the growing dendrites from reaching the anode. In this case, the electrodes were supported firmly and periodiccathode compression was applied every 5 minutes. The electromechanical compressing system [8] has been developed for laboratory and pilot scales. The cell applied in the laboratory experiments is shown in Figure 3, also illustrating the cathode crystals at the start and the finish of the compression period. The cathode compression system and the current supply were controlled by a special electronic device developed in our laboratory, based on micro-processing units. The system characteristics were recorded continuously by a data acquisition system consisting of an AD interface (NI-USB6212) and a data processing program specifically developed using the NI-LabView software.

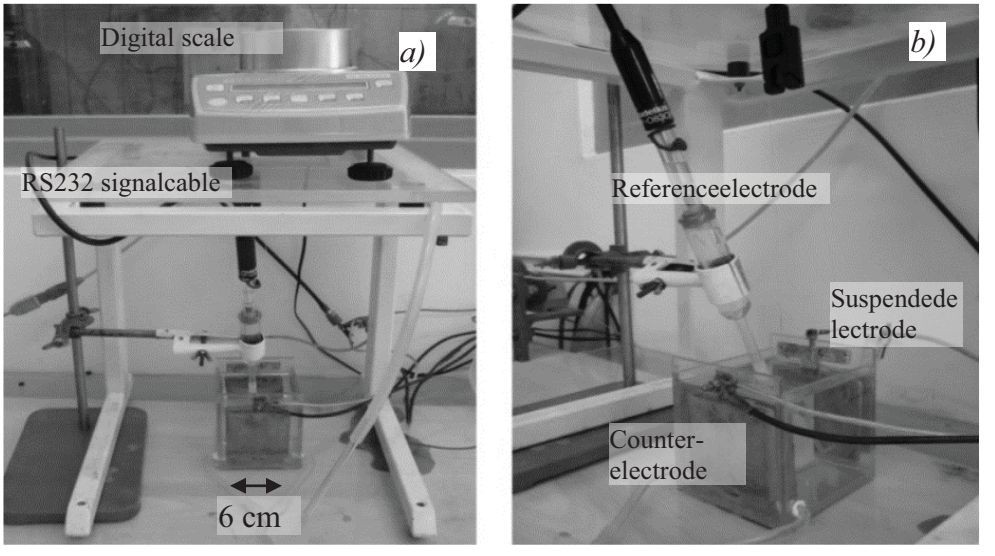

Figure 2. The electrolysis system equipped with mass and potential monitoring

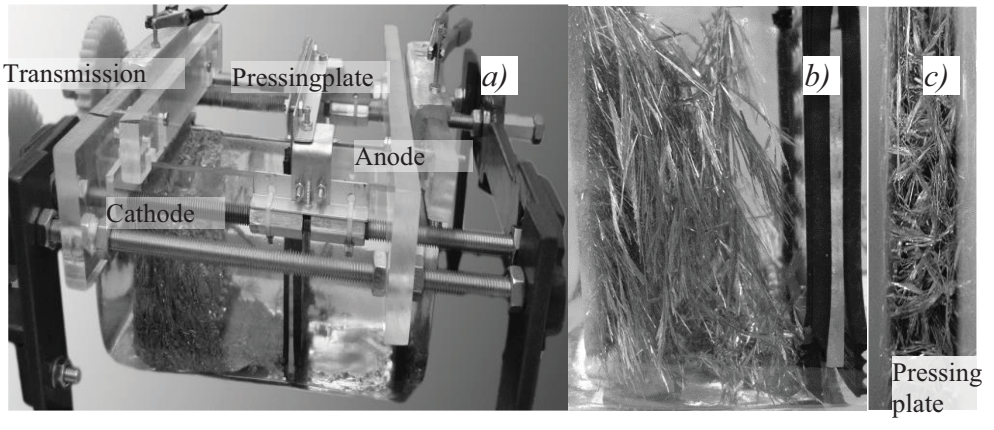

Figure 3. Laboratory-scale electromechanical refining cell (a), the cathode before (b) and after compression (c)

2. Experimental results and discussion

The electrode processes are clearly indicated by the continuously recorded masses of the electrodes. The buoyancy force in the electrolyte solution of the given composition was automatically corrected by an algorithm built in the computerized data processing system. The correlation is based on the density values of Figure 4, preliminarily determined.

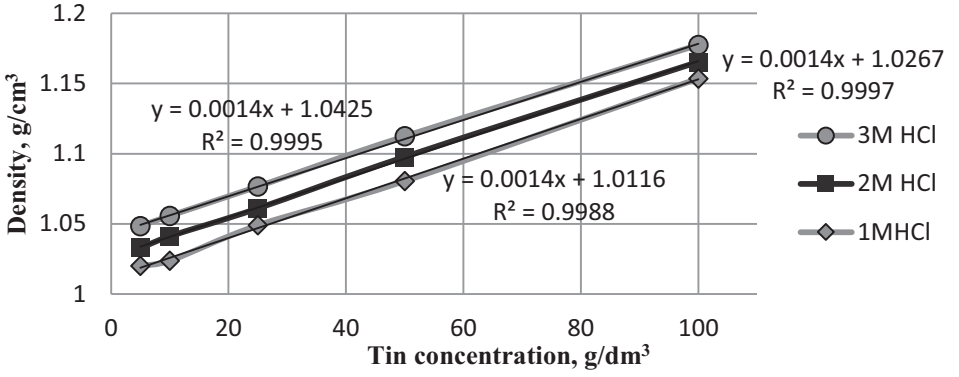

Figure 4. Densities of the electrolyte solutions as functions of the composition at 25 °C

The anodic process is demonstrated by the decreasing mass of the electrode. As shown in Figure 5*a*, the dissolution rates of the freshly prepared Sn99.9 (technically pure tin) anodes are proportional to the time elapsed after the start of the current and also to the applied anodic current density. With the high sensitivity of mass measurement, relatively slight furtherchanges in the mass could also be detected after the current was switched off (Figure 5*b*). It can be interpreted as an indirect proof for the assumed reaction of the Sn(IV) species with the metallic tin in the anode or in the produced slime layer. The effect is stronger after the electrolysis runs with higher anodic current densities. It can also be noted that in this case there is a progressive increase, as the amount of Sn(IV) generated does not only depend on the amount of electric charge transmitted, but also on the potential of the anode.

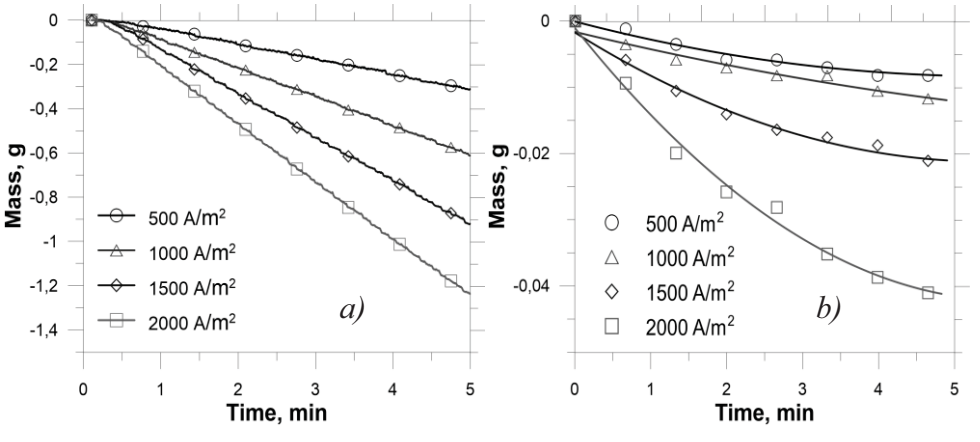

Figure 5.Changes in the masses of the Sn99.9 anodes during (a) and immediately after (b) electrolysis with different current densities (40 g/dm³ Sn, 25 °C)

The relevant anode potentials are shown in Figure 6. The values are measured vs. a calomel reference electrode and transformed according to the expression of the reference potential:

$$Hg_2Cl_2 + 2e = 2Hg + 2Cl^-, \qquad E = 0{,}283\ \text{V} \qquad (c_{Cl^-} = 1\ \text{mol/dm}^3) \qquad (4)$$

to be expressed vs. the standard hydrogen electrode (SHE). Figure 6 shows the potential values developing on different anode materials at relatively low (500 A/m^2) and high (2000 A/m^2) current densities in electrolyte solutions of low (10 g/dm^3) and high (40 g/dm^3) tin concentrations. The latter settings represent less favorable conditions for the anodic process.

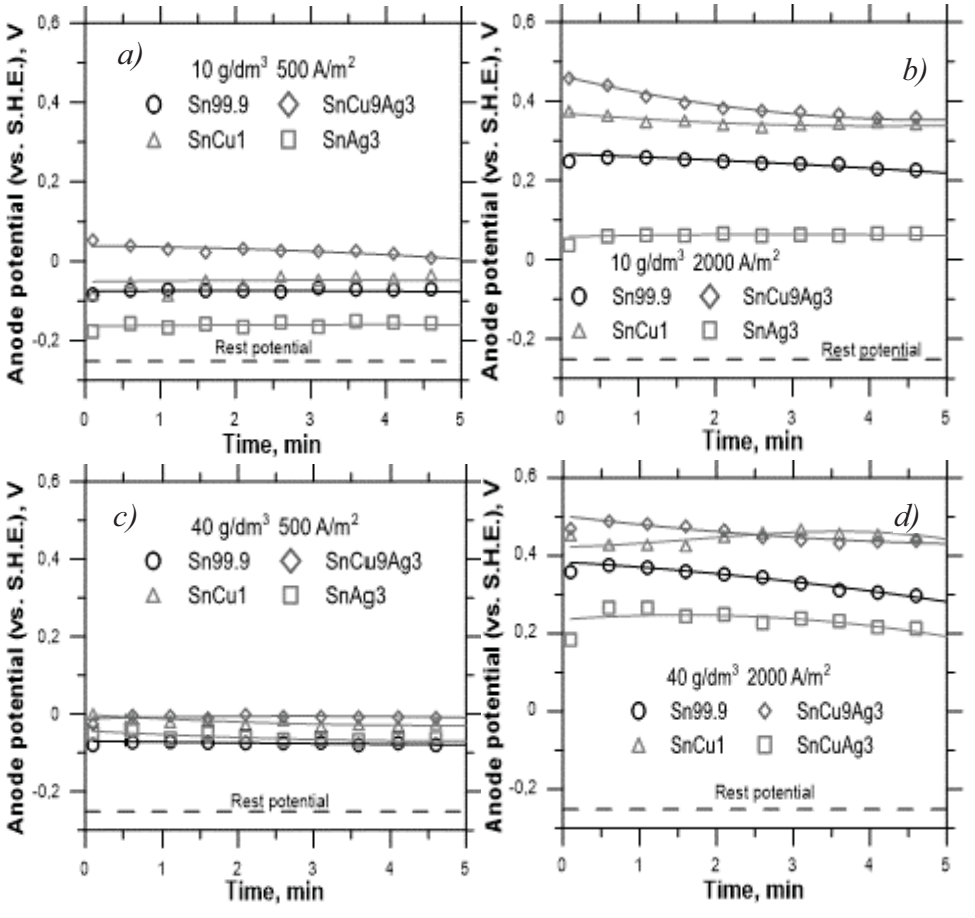

Figure 6. Measured potentials of different anode materials at different current densities and tin concentrations in the electrolyte (1 mol/dm^3 HCl, 25 ^{o}C)

The potentials do not show much change during the first 5 minutes of the electrolysis. Generally, the dissolution of the anodes alloyed with silver can take place at the lowest potentials, however copper seems to hinder the reaction. Especially at higher current densities, the anodic dissolution requires higher potential in the electrolytes of higher tin concentration. At the lowest examined current density, the anodes made of different materials, work at virtually the same potential.

The alloying elements influence the phase composition and the texture of the anode produced by casting. If the cooling rate is normal, copper may appear in the form of Cu_6Sn_5 intermetallics dispersed in the α-Sn solid solution type matrix. Silver is prone to form larger aggregates of the segregating Ag_3Sn phase [12]. Dissolution of the anode is not uniform

over the active surface. The solid solution and the primary crystalline tin phases, especially in the preferred orientation are preferentially dissolved. Thus the originally smooth surface becomes gradually rougher and some particles of the intermetallics and the matrix metal may drop out. The increasing surface area reduces the effective current density in a galvanostatic operation, which results in lower overpotentials. This mechanism is corroborated by the experienced higher mass of the anode slime, containing larger particles in the case of the silver containing anodes. The typical structure of the anode slime produced from the $SnCu_8Ag_3$ type anode material is shown in Figure 7.

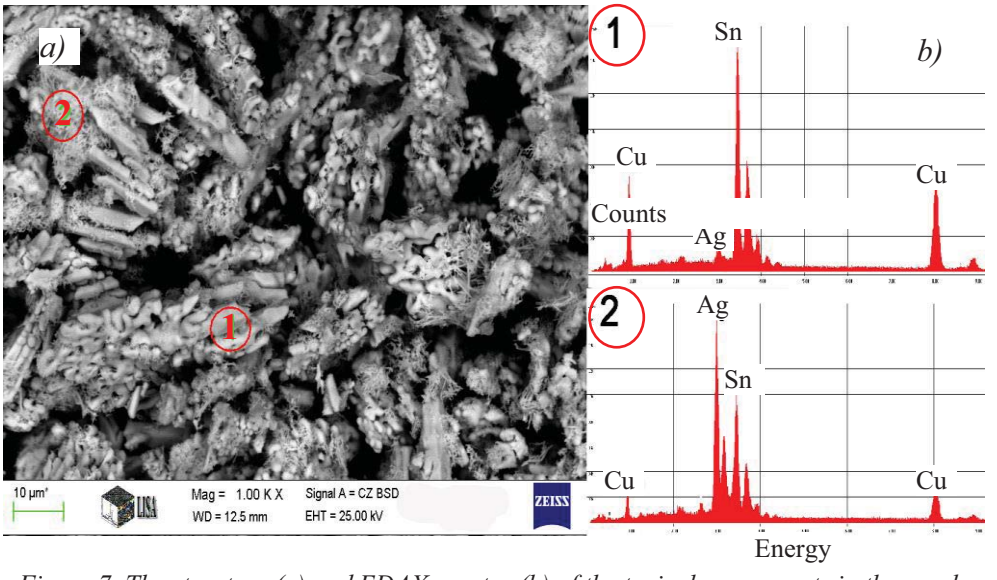

Figure 7. The structure (a) and EDAX spectra (b) of the typical components in the anode slime generated from the SnCu9Ag3 material

The area marked with No. 1 in Figure 7 indicates the virtually homogeneous Sn-Cu crystals, whereas the area marked with "2" shows the segregated fibrous Sn-Ag phase. The metallic content in the anode slime makes this by-product valuable, although selective extraction of the contained metals requires a special processing technology. The elemental analysis of the slime gives 44% total tin concentration, with 31% copper and 6.7% silver beside minor concentration of other impurities.

The results referring to the changing masses of different anodes in electrolytes of low and high Sn concentrations in the electrolyte (Figure 8) indicate that at high Sn concentrations the anodic dissolution partly takes place by generating Sn(IV) species even at relatively low anodic current densities. The resulting mass change is consequently less.

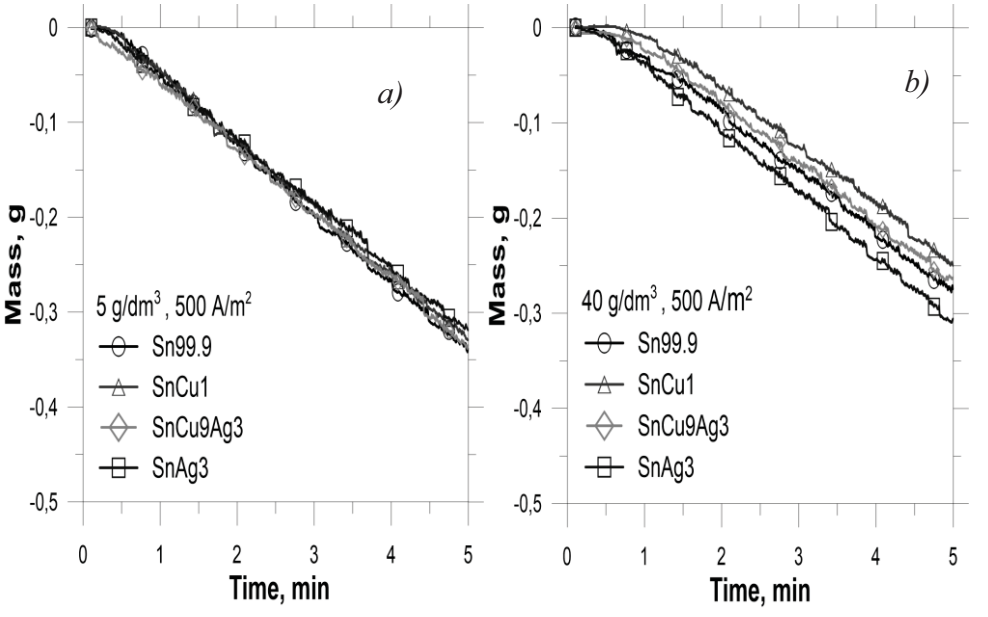

Figure 8. Measured mass changes of different anodes in electrolytes containing low (a) and high (b) concentrations of tin (1 mol/dm^{3}HCl, 25 ^{o}C)

The unfavorable anodic reaction at high anode potentials resulting in the generation of Sn(IV) species can be normally compensated by the secondary reaction in the slime, but there is virtually no such layer present at the surface of the anodes in the first 5 minutes of the operation. The Sn(IV) may thus escape to the bulk of the solution and reaching the cathode surface, they may cause re-dissolution by Eq. (1) As also seen, copper alloying deteriorates the conditions.

The cathodic process should be associated with a continually increasing mass of the electrode. However, Figure 9 shows that in electrolytes of low tin concentration the decreasing cathode masses were recorded after the start of the electrolysis. It is especially so at higher apparent current densities (Figure 9*b*). The current density for the cathode can only be expressed referring to the original geometric surface area. The fresh and smooth starting cathode is quickly covered by separately growing crystals of deposited tin, thus the actual surface area is increasing until a virtually stable form is reached. The initial decrease in the observed cathode mass is caused by the evolution of hydrogen gas. As demonstrated by Figure 10, the small bubbles are stuck at the gradually changing surface of the cathode and they are released slowly. Later, the cathode surface becomes rougher, the cathode potential may also rise under galvanostatic conditions and the hydrogen evolution stops. Subsequently the tin deposition is predominant. At high applied apparent current densities it happens considerably later.

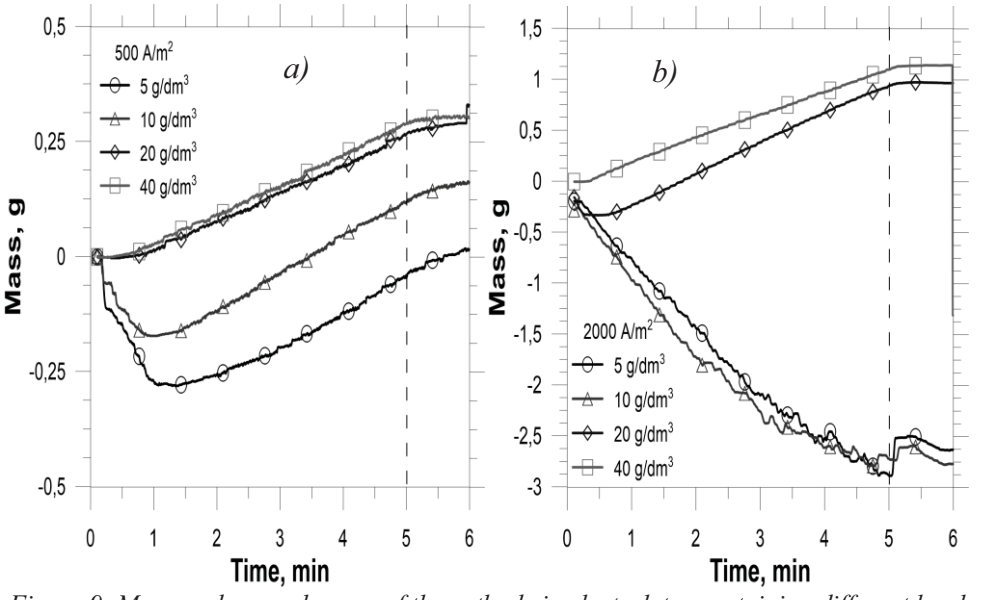

Figure 9. Measured mass changes of the cathode in electrolytes containing different levels of Sn concentration at low (a) and high (b) apparent cathodic current densities (1 mol/dm^3 HCl, 25 ^{o}C)

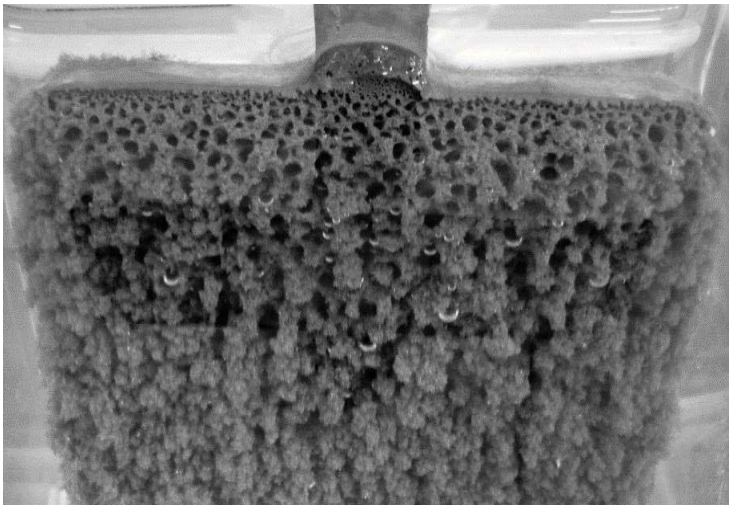

Figure 10. The initial structure of the cathode deposit influenced by the evolved gas bubbles (2000 A/m^2, 10 g/dm^3 Sn, 1 mol/dm^3 HCl, 25 ^{o}C).

This irregularity is however absent if the Sn concentration in the electrolyte is 20 g/dm^3 at least. The initial hydrogen evolution has little direct effect on the current efficiency but it is mostly unfavorable because of blocking a significant fraction of the active cathode surface when the initial tin deposition takes place. Thus the morphology of the produced

cathode deposit is also affected by these conditions. Because of the irregular contact with the substrate, the metal deposit is formed with a typical spongy structure.

The characteristic deposit structures obtained with the experiments of 5 min duration with the various tin concentration and apparent current density settings are arranged in Figure 11.

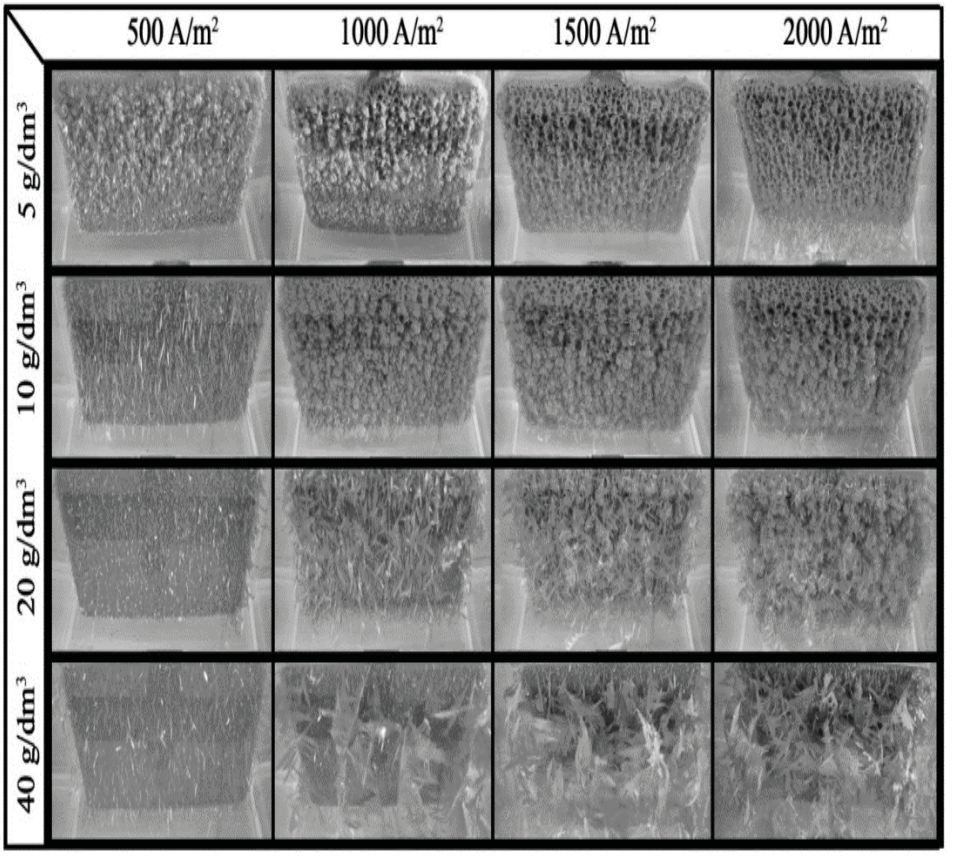

Figure 11. Cathodic deposits obtained with different apparent current densities in electrolytes of varied tin concentrations (1 mol/dm³ HCl, 25 °C)

A consistent or recurring evolution of hydrogen may also raise concern about the stability of the tin chloride solution because of the decreasing acidity and the danger of Sn(IV) hydrolysis. Although at higher then optimum apparent current densities, hydrogen bubbles do not interfere with the initial deposition, but the fast charge transfer associated with the sluggish ion transport [7] produces long dendrites and needle crystals, which is also undesirable.

The longer-term electrolysis may also involve the gradual change in the distribution of dissolved tin among its species. The iodometric analysis results of solution samples taken regularly during an 8h long run are plotted in Figure 12. The cathodic current efficiency – measured by removing the deposit every hour – referring to the whole time of electrolysis was ~95%.

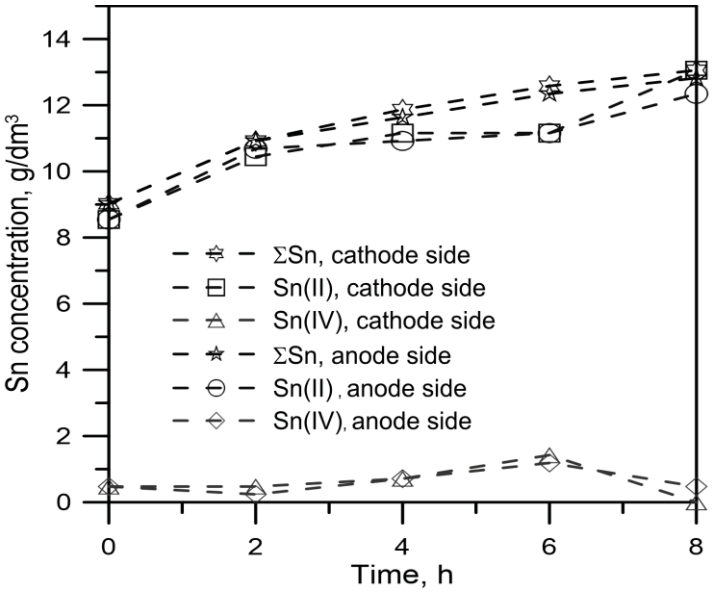

Figure 12. The change of Sn concentration during electrorefining (SnCu1 anode, 1000 A/m^2, 1 mol/dm^3 HCl, 25 ^{o}C)

As the current efficiency is close to the theoretical value and virtually no Sn(IV) species are found in the electrolyte, it may be assumed that the anodic process was run under favorable conditions. The slime layer – and the metallic particles in it - developed during the extended process could eliminate the generated Sn(IV) species and aerial oxidation could be considered negligible.

Conclusions

The specially designed experimental cell equipped with in-situ continuous mass measurement of the electrodes could indicate the principal processes taking place at the anode and the cathode during the initial stage of the tin electrorefining in chloride solutions. It has shown, that the tin anode is dissolving undisturbed in a wide range of current densities, however the distribution of dissolved tin among the possible Sn(II) and Sn(IV) species may vary. The presence of Sn(IV) ions was indirectly indicated by the mass changes. High currents are possible at significantly increased anode potentials, especially on anodes containing copper alloying. Controlling the anode potential is therefore primarily important in providing optimum conditions for the procedure. The anode slime is composed of a large proportion of metallic particles, especially with silver containing anodes. These particles may be efficient in eliminating the generated Sn(IV) species and help assure the desired overall anodic process of producing Sn(II) species. The experiments have pointed out the initial evolution of hydrogen at the cathode, especially in electrolytes of low tin concentration (< 20 g/dm^3) and high (> 1000 A/m^2) apparent current densities. Hydrogen bubbles stuck on the surface of the cathode may also deteriorate the developing structure of the tin deposit. The anodic slime not only contains a high proportion of metallic tin, but also collects – beside copper – the valuable silver content of the anode alloy. Therefore it is considered as an important by-product beside the cathode tine of high purity. The process is

stable under optimum conditions and electromechanical cathode compression can assure trouble-free operation over a long period of time without human supervision. The system of cathode compression, however may be further developed and the anode slime processing may be integrated with the electrorefining procedure. In that way this new technology can be attractive for practical implementation at the sites of electronic producers.

Acknowledgement

The research work presented in this paper based on the results achieved in the Center of Applied Materials Science and Nano-Technology at the University of Miskolc and within the TÁMOP-4.2.2.A-11/1/KONV-2012-0019 project, and carried out as part of the TÁMOP-4.2.2.D-15/1/KONV-2015-0017 project in the framework of the New Széchenyi Plan. The realization of this project is supported by the European Union, and co-financed by the European Social Fund.

References

[1] MANKO, H. H.: *Solders and Soldering.* McGraw-Hill, New York, 2001.
[2] PUTTLITZ, K. J.–STALTER, K.A.: *Handbook of lead-free solder technology for microelectronic assemblies.* CRC Press., 2004.
[3] HALSALL, P.: The Refining of Tin. *Metall,* 43, 1989, 131–136.
[4] TUNOLD, R.–BROLI, A.: Anodic and cathodic behaviour of tin in acidic sulphate solutions. *Corrosion Science,* 13, 1973, 361–373.
[5] RIMASZÉKI, G.–KULCSÁR, T.–KÉKESI, T.: Application of HCl solutions for recovering the puremetal from tin scrap by electrorefining. *Hydrometallurgy,* 125–126, 2012, 55–63.
[6] RIMASZÉKI, G.–KULCSÁR, T.–KÉKESI, T.: Investigation and optimization of tin electrorefining in hydrochloric acid solutions. *J. Appl. Electrochem,* 42, 2012, 573–584.
[7] KULCSÁR, T.–DOBÓ, Zs.–KÉKESI, T.: The Effect of Micro-impulse Current on the Morphology of Tin Electrodeposited from Chloride Solutions. *Materials Sci. Forum,* 752, 2013, 294–303.
[8] DOBÓ, Zs.–KULCSÁR, T.–KÉKESI, T.–RIMASZÉKI, G.: *Apparatus using programmable electromechanical cathode compression and current control for the electrorefining of soldering tin scrap and the process of its utilization.* Hungarian patent, HU201100722-A2. 10-860957.
[9] ZEMAITIS, J. F. et al.: *Handbook of Aqueous Electrolyte Thermodynamics.* American Inst. Chem. Eng. Inc., New York, NY, 1983.
[10] SILLÉN, L. G.–MARTELL, A. E.: *Stability Constants of Metal-Ion Complexes.* Supplement, Special Publ. No. 25, The Chem. Soc., London, 1964.
[11] KELSALL, G. H.–GUDYANGA, F. P.: Thermodinamics of Sn-S-Cl-H_2O system at 298 K. *Journal of Electroanal. Chem. and Interfacial Electrochem,* 280, 1990, 267–282.
[12] OSORIO, W. R. et al.: The Effects of Microstructure and Ag3Sn and Cu6Sn5 Intermetallics on the Electrochemical Behavior of Sn-Ag and Sn-Cu Solder Alloys. *Int. J. Electrochem. Sci.,* 7, 2012, 6436–6452.

Materials Science and Engineering, Volume 40, No. 1 (2015) pp. 88–95.

STUDYOFLEAD-FREESOLDERINGONSILVERPLATED COPPER

ÉVA KUN[1]–DÁNIEL SÓS[2]–ANETT GYENES[3]–
ZOLTÁN GÁCSI[4]–TAMÁS TÖRÖK[5]

The purpose of this paper is to comparesilver layers produced on copper substrates by five typical immersion plating (IP) methods and two electroplating procedures (EP), and to examine the wetting propertiesof a commonly applied, six-component lead-free solder alloyused for these differently made conductor surfaces.The formation of intermetallic phasesbetween the solders and the substrates wasinvestigated, andthe thicknesses of the silver layers were determined on the cross-sections of the samples by SEM-EDS and also by GD-OES analysis. The contact angles of the solder joints dropt on the plates were measured, respectively. Intermetallic compounds (IMC)were detected in the solder material as spheroid Ag_3Sn and$(CuNi)_6Sn_5$needles.The thickness of immersion silver layers ranged within a few hundred nanometers, while electroplatedlayers reached up to 5-10 μm.The intermetallic layers (IML) were very thin and could not be easily detected even by scanning electron microscope. The silver layer was partially or totally dissolved into the solder drop – depending on its thickness. The lowest contact angle was observed for matt electroplating silver coating, the worst wetting was given by the immersion silver plating solution containing cyanide. Consequently, the target alloy system shows affinity to dissolve approximately 9-10 μm thickness of the silver layer into the solder matrix.

Keywords: lead-free soldering, silver plated copper, immersion plating, electroplating, intermetallic layer

Introduction

Recently, a series of development on Pb-free soldering have been carried out, giving free way to a huge variety of lead-free soldering materials.On the other hand, preference is given to the research of surfaces and coatings used for PCB-s and other electronic and microelectronic devices. Materials with improved mechanical properties and enhanced thermal stability are also a current topic. The switch to lead free solders has resulted in a wide variety of solder alloy compositions. Silver coatings produced on copper substrates have many advantages, such as good conductivity, proper solderability and high corrosion resistance. The preferential properties depend on the technology of silver plating, the applied solutions and the processing method. Silver coatings can be produced by electroplating immersion, fototechnical and layer precipitation platingmethods.

[1] University of Miskolc,Institute of Metallurgy and Foundry Engineering
Miskolc-Egyetemváros 3515, Hungary
anyag21@gmail.com
[2] University of Miskolc,Institute of Metallurgy and Foundry Engineering
Miskolc-Egyetemváros 3515, Hungary
daniel.sos.89@gmail.com
[3] University of Miskolc,Institute of Physical Metallurgy, Metalforming and Nanotechnology
Miskolc-Egyetemváros 3515, Hungary
femanett@uni-miskolc.hu
[4] University of Miskolc,Institute of Physical Metallurgy, Metalforming and Nanotechnology
Miskolc-Egyetemváros 3515, Hungary
femtangz@uni-miskolc.hu
[5] University of Miskolc,Institute of Metallurgy and Foundry Engineering
Miskolc-Egyetemváros 3515, Hungary
fektt@uni-miskolc.hu

Several studies are devoted tosilver plating methods, but little is said about their performance in terms of soldering – either separately or in comparison. Gyenes et al. measured the effect of nickel content on a six-component solder alloy, where they found needle-like intermetallic phases[1]. Gergely et al. [2] described the formation of precipitates under the effect of lead and bismuth, which limits elementary and structural diffusion across the IMClayer, furthermore, beyond a given concentration level, it promotes IMC growth. Antimony, on the other hand, blocks excessive intermetallics growth and decreases the thickness of the IMC layer, leading to finer structure. It should be noted thatantimony has been identified as a harmful element by the United Nations Environment Program (UNEP) [3]. There is a number of papers addressing the effect of particular components on soldering alloys, and the formation kinetics of intermetallic compounds is also considered as a major topic [4–11].

1. Materials

Solder. A lead-free material was used for soldering, composed of tin, 3.8wt% silver, 0.7wt% copper, 3wt% bismuth, 1.4w% antimony and 0.15wt% nickel. It is an advanced variation of the well-known SAC (Sn-Ag-Cu) solders, where antimony and part of the bismuth are dissolved in the β-tin solid solution, while Ni is added to improve the mechanical properties throughthe formation of intermetallic compounds.

Substrates. The substrates were thin silver plated copper foils, where the thickness of the high purity copper substrate was about 90 μm. The visual appearance of the silver plated copper substrates is shown in Figure 1. The most relevant data of the silver plating methods are briefly summarized in Table 1.

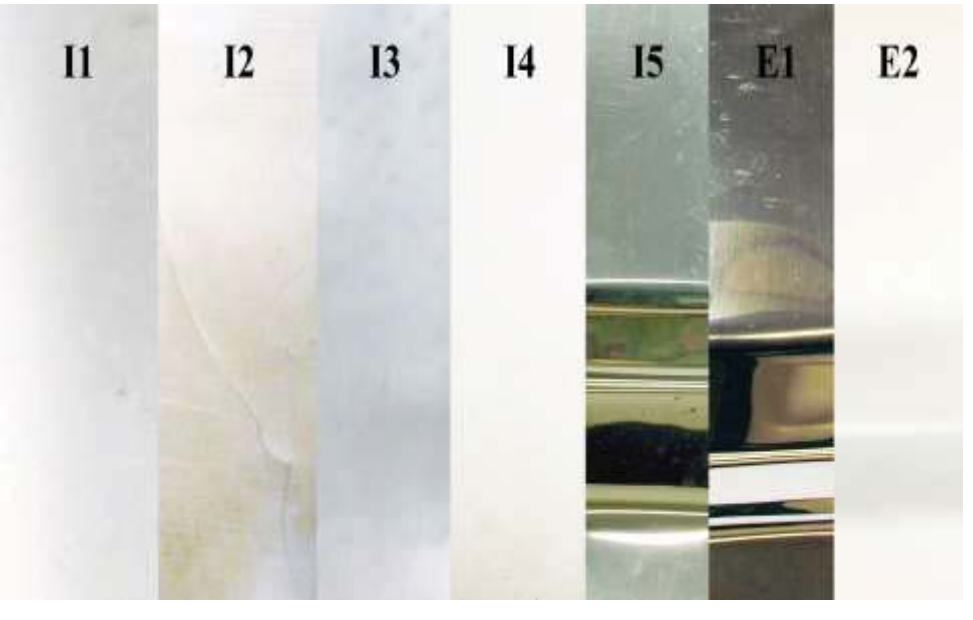

Figure 1. Visual appearance of the silver plated copper substrates

Table 1

Silver plating methods of substrates

Sample	Silver plating method
I1	Immersion plating with silver-nitrate, sodium-thiosulphate and ammonia
I2	Immersion plating with silver-nitrate, ammonium-thiosulphate and ammonia
I3	Immersion plating with Sterling 2.0
I4	Immersion plating with Sterling 2.0 B
I5	Immersion plating with Argentomerse NC
E1	Electroplating, shiny surface, passivated
E2	Electroplating, matt surface, passivated

The soldering was executed with a soldering-iron type Parkside PLS 48 B1, and a Fahrenheit ZWN 17071 (DIN 8511) type flux was applied before the soldering process.

We must call attention to the fact that the soldering procedure is the commonly applied method with soldering-iron, where the heat treatment cannot be controlled properly to set a strict temperature and treatment time, but on the other side, this demonstrates the really common application of solders.

2. Evaluation methods

Optical microscopy and SEM-EDS. To inspect and analyse the cross-section of the soldered, silver plated copper specimens, optical microscopy and scanning electronmicroscopy (SEM) were utilized with energy dispersive spectroscopy (EDS). A Zeiss AxioVision Imager m1M type optical microscope with an AxioVision Rel. 4.8 software was used for relatively low magnification. For higher magnification and elementary analysis, a Zeiss EVOMA10 scanning electron microscopeand an EDAX type electron microprobe were applied. For sample preparation, the cross-sections of soldered foils were embedded into a resin cylinder. After proper solidification, metallographic sections were grinded with P320, P400, P600, P800, P1200, P2400 and P4000 fine abrasive wheels, polished with MD Mol (3 μm) and MD Nap (1 μm) type clothes using Lubricant Blue solution, then polished with a colloid containing SiO_2 particles of 0.02 μm average size.

GDOES. By immersion plating one can produce only rather thin (up to a few hundred nms thick) deposits, therefore the elementary concentration depth profiles were measured by GDOES (Glow Discharge Optical Emission Spectrometer, type GD Profiler 2, France). In the case of depth profiles, the horizontal axis represents the sputtering time of argon plasma which is proportional to the crater depth of the specimen. The sputtering time was converted to the depth of the sputtered craters using the profilometers MarSurf M400 and Ambios XP-I.

Contact angle. A SEE (Surface Energy Evaluation) System was used obtained from the Advex Instruments to determine the contact angle of solder drops on silver plated copper samples. All the substrates were soldered with three drops using flux and soldering iron. Every drop was measured three times. From the data,surface tension was calculated.Since the instrument is designed primarily for contact angle measurement and surface energy determination, for the proper analysis of the drop profile, the measurement points had to be fitted with an image taken of the sample to yield results that are supposed to determine the baseline and the radius of spherical solder drop.

3. Results

The ***visual appearance*** of the silver plated copper substrates is shown in Figure 1. Sample E1 exhibited the shiniest surface. Just like sample E2, sample I4 (which was produced using Argentomerse NC) looked absolutely matt and white, but the coating was not so durableas the electroplated coating. All other samples had silver-grey, meanly durable, glossy metallic surface coatings. SEM images of the silver plated substrates are shown in Figure 2. As seen,sample I3, I4 and E2 have a thick, rough, mortar-like appearance. The roughness of these surfaces provide for a high reflection of photons, so macroscopically the whiteness is justified, but sample I3 is actually on the verge between the shiny and matt looks. All the other materials have shiny, steady, flat surfaces.

Surface topographycan likewise be displayed in SEM images (Figure 2), where one can observe that the immersion silver plated samples possess a high level of porosity on the surface, while there are no detectable holes on electroplated coatings. Notable porosity was noticed only in the case of sample I5, therefore the backscatter type image of the sample with two measurement points are shown in Figure 3.

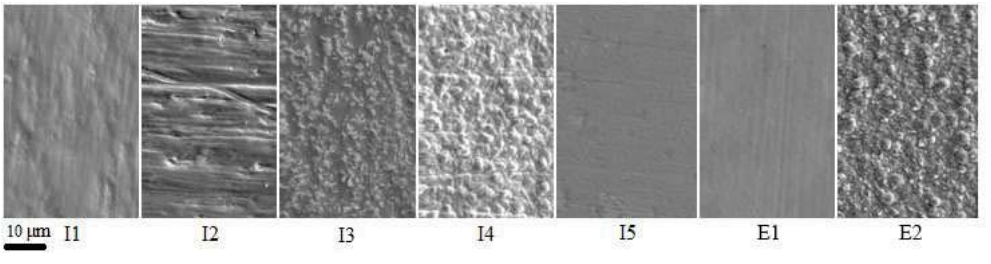

Figure 2. SEM images of the surfaces of the silver plated copper foils, Mag1000X

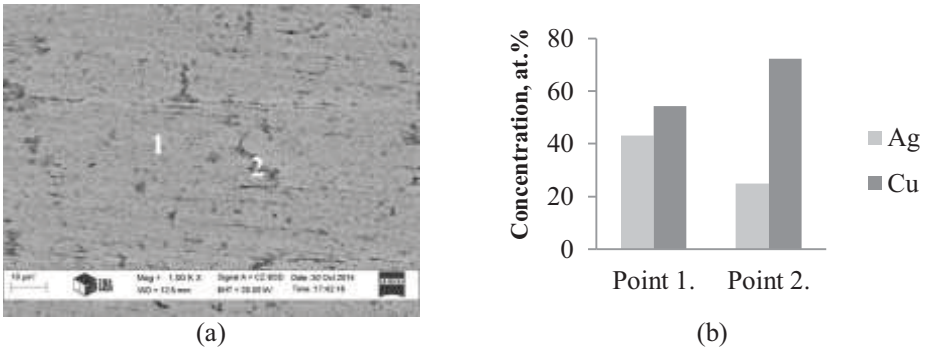

Figure 3. BSE image of sample I5, Mag 1000X (a), Ag and Cu content of points 1 and 2 (b)

The thickness of the immersion plated samples was so low that, from the front side of the samples, it was impossible to measure any more than a bit of silver by EDS, because the electron beam induced a deeper area than the thin silver layer. SEM-EDS cross-section tests were performed on each of the specimens. Furthermore, GD-OES surface analysis was executed, complemented with a profilometric crater depth profile measurement, where the results were similar to those obtained in previous method. Figure 4 shows the results of the surface analysis, where one can see that the twoelectroplating silver coatings (about 5 and 9

μm) are much thicker, than the few hundred nm thick immersion silver layers. The weakest coating was produced with the Sterling 2.0 solution. The thickness of the silver layers can be seen in Figure 4.

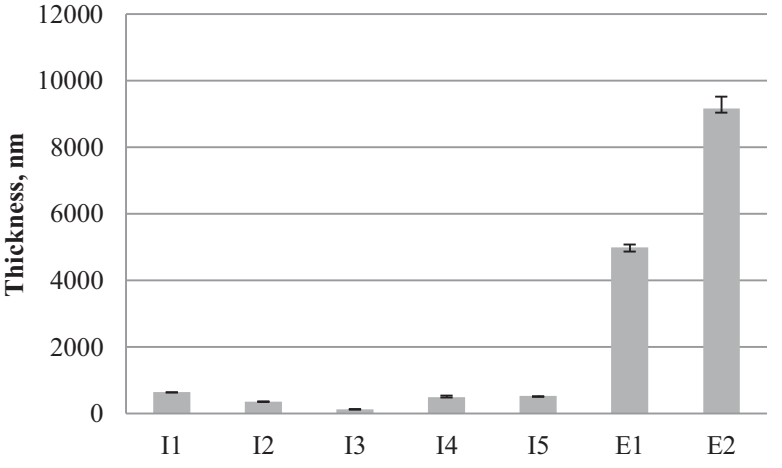

Figure 4. Thickness of the silver layers on the copper foils

Silver layer thicknesswasreduced by contacting with the solder, presumably the silver solved into the solder matrix, as it is visibly in the optical microscope images of the electroplated sample E2 (Figure5 and Figure6).

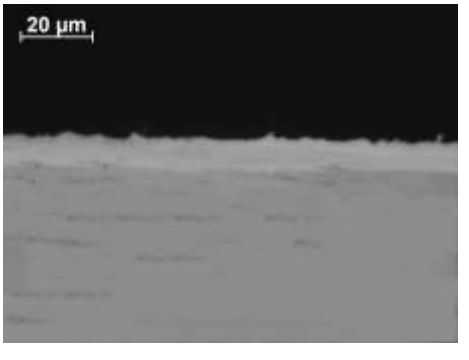

Figure 5. Sample E2 before soldering

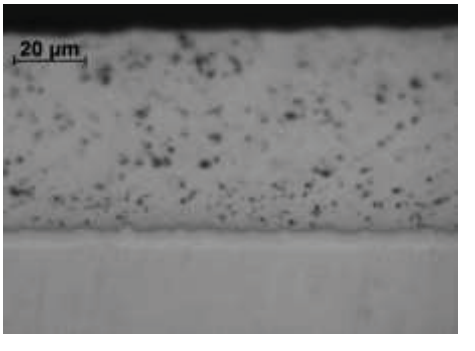

Figure 6. Sample E2 with solder drop

A significant portion of the silver layer was dissolved into the solder drop. A point scale was created geometrically with bulk analysis on these sections. The main elements were measured quantitatively in two points as shown in Figures 7–8 and Tables 2–3, where one can see that the Ag-content of the parts of silver coating closest to the solder has decreased. Some tin diffused into the silver layer (Point 1), but other elements showed no significant traceable diffusion.Very thin Ag_3Sn (Point 2 in Table 2) intermetallic layer (below 1 μm) could be detected by using scanning electron microscope (Figure 7). Furthermore hexagonal structures and holes were found in the solder joint.

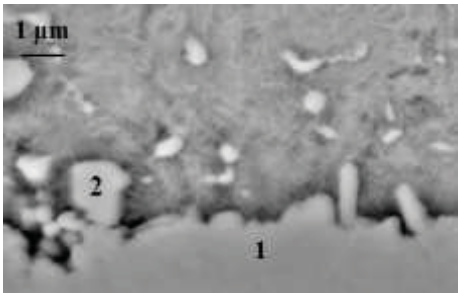

Figure 7. SEM image of the solder joint between the matt silver electroplated copper substrate and the solder (Sample E2)

Element	Point 1	Point 2
Bi	0.67	0.63
Ag	**94.70**	**66.55**
Sn	1.66	**31.25**
Sb	–	0.17
Ni	0.92	–
Cu	2.05	1.40

Table 2. Chemical composition in at.% of points 1 and 2 shown in Figure 7

Different phases were observed in the cross-section SEM images of thesoldered samples.An example is presented below in Figure 8 which shows the cross-section of the soldered glossy silver electroplated copper (sample E2).The microstructure of the solder drop consists of supposedly $(Cu,Ni)_6Sn_5$ (Point 3) and Ag_3Sn (Point 4) IMC phases beside the β-Sn solid solution (Point 2). These intermetallics are located sporadically in the β-tin matrix. The chemical composition of the phases analysed by EDS are summarized in Table 3. It should be noted that the size of the detection area is about 2 µm, thus these concentrations are not exact for those phases that are less than 2 µm.

The silver layer (Point 1) contains tin, nickel and a small amount of bismuth, which comes from the solder matrix, and a little copper is also detected, which may derive from the solder or from the bulk material of the copper substrate. No other contaminants were detected on the surfaces in any significant or appreciable amount.

The *contact angles* of solder joints on silver plated copper substrates are shown in Figure 9. The measurements were performed in 3 replicates. The contact angle of solder joint on matt silver electroplated sample (E2) was so small that it could not be measured with this method. The Sterling type silver plating solutions provided the weakest wetting between the solder joint and the substrate with using the given flux.

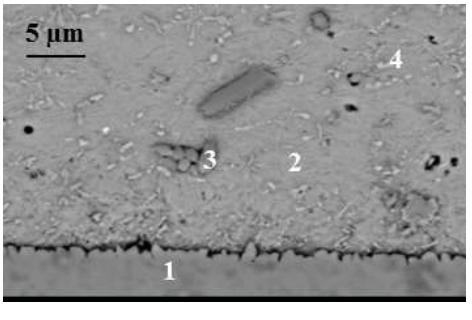

Figure 8. SEM image of the microstructure of the solder joint (sample E2)

Element	Analysed point			
	1	2	3	4
Bi	0.39	**2.27**	0.30	2.18
Ag	**93.01**	0.19	0.28	**7.60**
Sn	3.33	**92.78**	**47.99**	**86.88**
Sb	–	**3.05**	1.15	1.88
Ni	1.01	0.63	**12.85**	–
Cu	2.26	1.08	**37.43**	1.46

Table 3. Chemical composition in at.% of the phases marked on cross-section SEM image shown in Figure 8

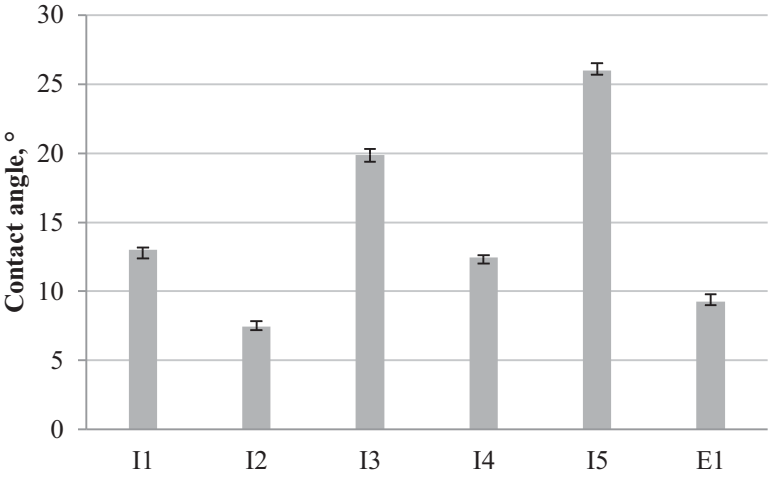

Figure 9. Contact angles of the silver plated samples

The cyanide-free, Argentomerse type solution and the two other immersion silver platedsamples exhibited much better wetting properties than the cyanide ones. The best results were obtained for the matt silver electroplated copper foil, where the solder drop was so flat that it was not measurable and respectively could not be determined. The good wettability of the matt electroplated surface was followed by the immersion silver plated sample with ammonium-thiosulfate, then the shiny, electroplated foil.

Summary

The quality andthe thickness of 7 types of silver layers – producedby five typical immersion plating methods and two electroplating procedures – on copper substrateswere evaluated, and the wetting behaviour of a six component (Sn-3.8Ag-0.7Cu-3Bi-1.4-Sb-0.15Ni) lead-free solder was measured on these particular surfaces. Besides, the microstructure and composition of different parts of the solder drop were examined and several phases were detected. The intermetallic compound layerbetween the substrate and the solder drop was investigated on the cross-sections of the samples. Elementary diffusion and the formed phaseswere studied.Thin silver layers were analysed by GD-OES and SEM-EDS, and the latter method was also used to analyse and evaluate the grade of soldering on the surfaces.

Based on the results, it can be stated that the best wetting was occurred at the matt silver electroplated surface, which was followed by the glossy electroplated substrate. The greatest contact angle was measured for the immersion plated copper using cyanide. Different compound phases were observed in the solder matrix (supposedly $(Cu,Ni)_6Sn_5$ and Ag_3Sn). Each of the thin immersion silver layers were totally dissolved into the solder drop. The electroplatedsilver layers were thick enough to enable the measurement of the dissolved part of Ag. Approximately 5 μm of initial thickness of Ag have been diffused into the solder drop.

Acknowledgement

The research work presented in this paper based on the results achieved within the TÁMOP-4.2.1.B-10/2/KONV-2010-0001 project and carried out as part of the TÁMOP-4.2.2.A-11/1/KONV-2012-0019 project in the framework of the New Széchenyi Plan. The realization of this project is supported by the European Union, and co-financed by the European Social Fund.
Furthermore the authors would like to express their thanks to Árpád Kovács for the SEM images and the EDX analysis.

References

[1] GYENES, A.–PÁZMÁN, J.–GÁCSI, Z.: Effects of nickel on the formation of intermetallic compounds in lead-free solder. *Anyagm. Tud.,* 38 (1), 2013, 93–102.
[2] GERGELY, G.–MOLNÁR, A.–GÁCSI, Z.: The role of Pb impurity in SAC solder alloy. *Material Science Forum,* Vol. 752, 2013, 42–47.
[3] CHEN, B. L.–LI, G. Y.: Influence of Sb on IMC growth in Sn-Ag-Cu-Sb Pb-free solder joints in reflow process. *Thin Sol. Films,* 462–463, 2004, 395–401.
[4] ZENG, K.–TU, K. N.: Six cases of reliability study of Pb-free solder joints in electronic packaging technology. *Materials Science and Engineering,* R 38, 2002, 55–105.
[5] LI, G. Y.–SHY, X. Q.: Effects of bismuth on growth of intermetallic compounds in Sn-Ag-Cu Pb-free solder joints. *Trans. Nonf. Met. Soc. China,* 16, 2006, 739–743.
[6] MIRIC, A. Z.: New developments in high-temperature, high-performance lead-free solder alloys. *Proceedings of the SMTA International Conference,* Orlando, FL, 24–28 October, 2010.
[7] STEEN, H.–TOLENO, B.: *Development of a lead-free alloy for high-reliability, high-temperature applications.* http://www.hlinstruments.com/RoHS_articles. (2010)
[8] LALL, P.–SHANTARAM, S.–SUHLING, J.–LOCKER, D.: Mechanical deformation behavior of SAC305 at high strain rates.Thermal and Thermomechanical Phenomena in Electronic Systems (ITherm). *13th IEEE Intersociety Conference,* San Diego, CA, 1037–1051, 2012.
[9] *ASM Handbook, Volume 3: Alloy phase diagrams.* ASM International, 1992.
[10] KATTNER, U. R.: Phase diagrams for Lead-free solder alloys. *Journal of the Minerals. Metals and Materials Society,* 54, 2002, 45–51.
[11] NOGITA, K.: Stabilisation of Cu_6Sn_5 by Ni in Sn-0.7Cu-0,05Ni lead-free solder alloys. *Intermetallics,* 18, 2010, 145–149.

Materials Science and Engineering, Volume 40, No. 1 (2015) pp. 96–104.

ELECTROKINETIC STUDY OF IMPACT OF LAPONITE PLATELETS ON STABILIZATION OF CARBON NANOTUBES IN AQUEOUS SUSPENSIONS

MARYNA MANILO[1]–NIKOLAI LEBOVKA[2]–SÁNDOR BÁRÁNY[3]

To characterize the electric double layers of multi-walled carbon nanotubes, laponite platelets and their hybrid particles, the electrophoretic potential was measured as a function of pH and concentration of electrolytes (KCl, $CaCl_2$ and $AlCl_3$). Nanoparticles under study have negative zeta potential value in the whole studied pH interval (2–12). An increase in pH from 2 to 12 resulted in substantial increase of the absolute (negative) values of the zeta potential of nanotubes due to dissociation of surface hydroxyl and carbonyl groups, which was identified by infra-red spectroscopy. The observed attraction between similarly charged carbon nanotubes and laponite particles was explained by highly heterogeneous distribution of negatively charged functional groups on the surface of nanotubes and difference in zeta potential of nanotubes and laponite particles.
Keywords: carbon nanotubes, laponite platelets, zeta potential, aggregation, pH, electrolytes

Introduction

Carbon nanotubes (CNTs) are promising materials for preparation of CNT-laden nanofluids [1], carbon-based catalysts [2], adsorbents for waste water treatment [3], highly selective nano- [4] and biosensors [5] and many other attractive materials with extraordinary mechanical, thermal and optical properties. Numerous applications of CNTs require their good dispersability in the media and stability of the properties. The problem is that CNTs show high tendency to aggregation due to strong van der Waals interactions in the most of solvents [6]. High hydrophobicity of CNTs may be also an important factor of aggregation in water and hydrophilic solvents [7].

Dispersability of CNTs in aqueous suspensions can be enhanced by surface treatment (for example, oxidation [8]), adsorption of polymers or surfactants and addition of other types of nanoparticles [9]. Aggregation behaviour of CNTs in the presence of surfactants [10], polymers or electrolytes [11] and at different pH values of the system [12] was studied. Addition of electrolytes to the suspension (e.g. with Na^+, K^+, Ca^{2+}counterions) results in suppressing the electrostatic repulsion between individual CNTs and inducing their aggregation [11]. The aggregation kinetics of CNTs at different pH values, the effect of concentration of electrolytes and humic acid (HA) was evaluated [12]. The presence of HA enhanced the stability of CNTs, that was dependent on the type of electrolyte added. Similar effects were observed for CNTs with sodium dodecylbenzene sulfonate as a dispersing agent [11]. The correlations between electrokinetic potential of multi-walled CNTs, dispersability in different solvents (water, ethanol and hexane), stability of CNT suspensions, surface energy, and oxygen content of CNTs, modified by functionalization,

[1] National Academy of Sciences of Ukraine, F. D. Ovcharenko Institute of Biocolloidal Chemistry
Kyiv 030142, Ukraine
assol_M@i.ua
[2] National Academy of Sciences of Ukraine, F. D. Ovcharenko Institute of Biocolloidal Chemistry
Kyiv 030142, Ukraine
[3] University of Miskolc, Institute of Chemistry
Miskolc-Egyetemváros 3515, Hungary

were discussed [13]. It was speculated that CNT dispersability in a liquid is affected by the hydrophilic character of a considerable part of theCNT surface, which is reflected by the electrokinetic potential value. Recently, the electrokinetic behaviour of multi-walled CNTs and oxidized multi-walled N-doped CNTs was also studied [14]. The electrokinetic behaviour of CNTs was similar to that observed for inorganic colloid particles. A correlation between sedimentation stability and electrosurface properties of CNTs was observed [14].

Recently, it was shown that addition of charged laponite clay platelets significantly improved the dispersability of CNTs in aqueous suspensions [9] and prevented their aggregation. However, the nature of interactions between CNTs and laponite platelets is still unclear. The important contribution may be associated with surface/electrosurface properties of CNTs, i.e., chemical nature and concentration of surface functional groups that determine wetting, surface charge density and electrokinetic potential, as well as dispersability of the nanotubes.

The aim of our paper was to elucidate the nature and mechanism of stabilization of CNTs suspensions by laponite platelets and aggregation kinetics of CNTs, laponite and hybrid CNT+laponite nanoparticles in the presence of acid/base and different electrolytes. Also the zeta potential of multi-walled CNTs, laponite and hybrid CNT+laponite nanoparticles as a function of pH and electrolyte concentration was characterized.

1. Experimental Materials and Procedure

Multi-walled carbon nanotubes (CNTs) were produced by CVD method in the presence of Fe-Mo-Al catalyst (Specmash, Kyiv, Ukraine) and purified as described in [15]. CNTs are composed of concentric shells with inter-shell distance equal to 0.34 nm, their typical outer diameter was 10–20 nm, while their length was 5–10 μm. The specific surface area of CNTs, determined by nitrogen adsorption, was 254 m^2/g. CNTs have several walls within the range of ≈ 6–8 layers and their density varies from 1.6 g/cm^3 to ≈ 1.0 g/cm^3 with increasing the outer diameter from 10 nm to 20 nm [15].

Laponite RD, i.e. RD grade laponite (Rockwood Additives Ltd., UK) is a synthetic clay with chemical formula $Na_{+0.7}[(Si_8Mg_{5.5}Li_{0.3})O_{20}(OH)_4]_{-0.7}$ [16]. Its specific surface area, determined by nitrogen adsorption measurements, is 370 m^2/g and its density is ≈2.53 g/cm^3. Laponite is composed of charged disk-like sheets with thickness ≈1 nm and average diameter ≈ 25–30 nm. Laponite platelets are charged highly heterogeneously in aqueous suspensions: their faces have constant negative charge, while the surface charge of their edges is pH-dependent and it is positive in acidic medium [17]. The negative surface charge of laponite RD, defined as its cation exchange capacity (CEC), was equal to 0.75 meq/g.

For visual characterization of CNTs and CNT+laponite hybrid particles, their transmission electron microscopic (TEM) images were recorded using FEI Technai G2 (200 kV and LaB_6 as a cathode) instrument. Aqueous suspensions of nanoparticles were sonicated during 2 min in Elmasonic S10 H (Elma, Hans Schmidbauer GmbH & Co. KG) device. One drop of suspension was put on Lacey carbon and was dried in open air.

The electrokinetic potential, ζ, was determined using ZetaSizer NS (Malvern, UK) device. Determination of the electrophoretic mobility is based on the Doppler-effect.The program used in this instrument converts the electrophoretic mobility of particles into electrokinetic potential using the classical Smoluchowsky formula. This procedure is acceptable for our systems with relatively big particles/long threads and thin double layers, i.e. forwhich the contribution of the electrical double layer polarization to the electrosurface

phenomena can be neglected. The values of ζ indicated below typically represent an average from three-five individual measurements.Before measurements, the suspensions of CNTs and laponite in distilled water were sonicated during 30 min at 35 kHz in the ultrasonic bath (Tesla, Czech Republic). Then hydrochloric acid or sodium hydroxide was used for adjustment of pH values and KCl, $CaCl_2$ and $AlCl_3$ were used as electrolytes.

The preliminary investigations showed the presence of some changes in ζ-potential after preparation of suspensions. However, these dependencies got stabilized after 60 min, the constant values of ζ-potential were acquired, and all presented data correspond to the time t = 60 min.

Each experiment was performed, at least, three times in order to determine the mean values and the mean square errors.

2. Experimental Results and Discussion

Figure 1 shows example of high resolution TEM image of a typical CNT (Figure 1*a*) and CNT+laponite hybrid particles (Figure 1*b*). It can be seen that the inner and outer diameters of the presented CNT were ≈ 5 nm and ≈ 10 nm, respectively and the number of walls was 7 (Figure 1*a*). In hybrid CNT+laponite systems the laponite platelets are localized on the surface of individual CNTs (Figure 1*b*).

Preliminary experiments showed that at $X \geq 0.5$ hybrid suspensions were stable against sedimentation. In further electrokinetic experiments the stable hybrid suspensions with optimal ratio of the components, $X = 1$, were used.

Figure 2 shows the pH dependencies of the electrokinetic potential, ζ, of CNTs, laponite platelets and CNT+laponite hybrid nanoparticles in distilled water. All nanoparticles under study were charged negatively in the whole interval of pH values (pH = 2–12). The step-like run of ζ-potential of CNTs versus pH was observed: there was a steep increase of ζ-potential at pH below 4 and above 8, and the ζ-potential was nearly constant ($\zeta \approx -30$ mV) in the interval of pH 4–8. Such behaviour may reflect the changes in the surface charge density and indicate the presence of carbonyl functional groups and phenolic hydroxyls with pK~2–3 and 10, respectively, which is in full correspondence with the data of IR spectroscopy [15].

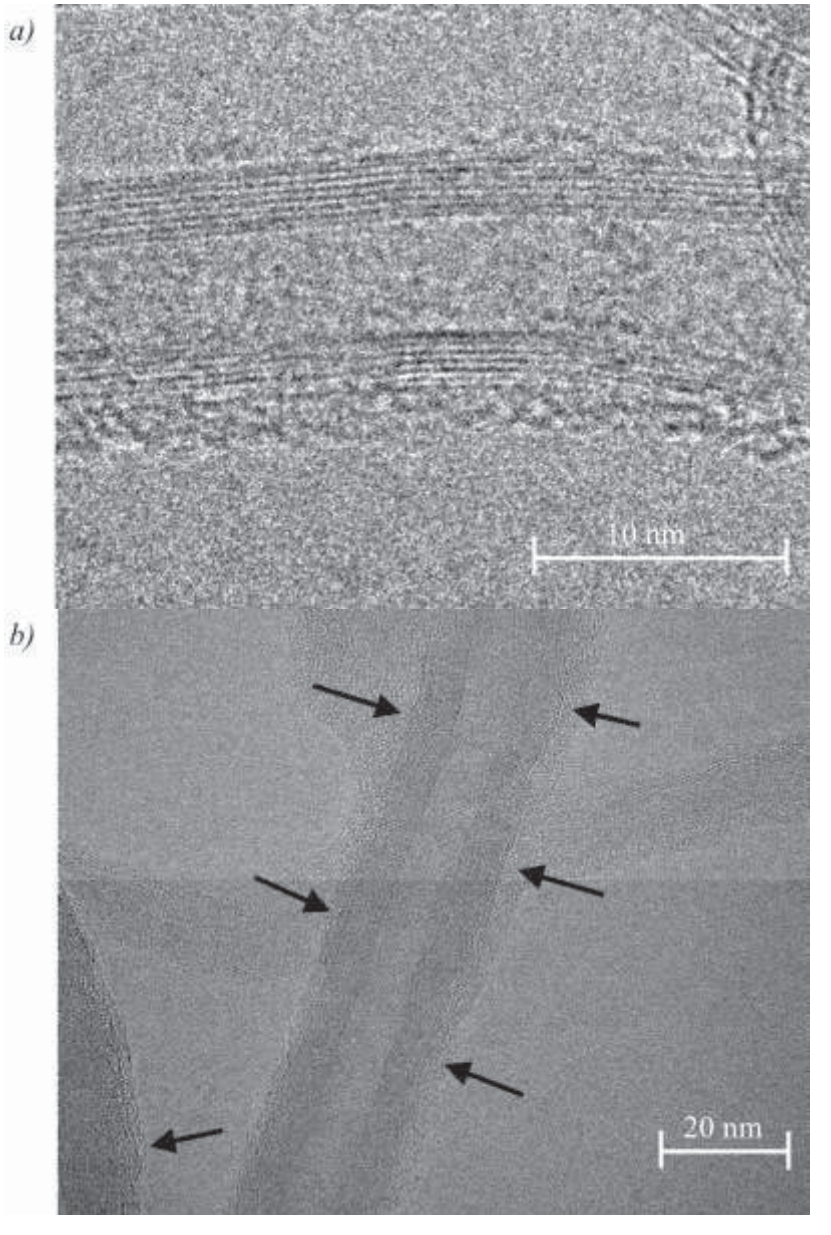

Figure 1. High resolution TEM image of CNT (a) and CNT+laponite hybrid nanoparticles at mass ratio $X = m_L/m_{CNT} = 0.5$ (b). Arrows shows the localization of laponite platelets on the surface of CNTs

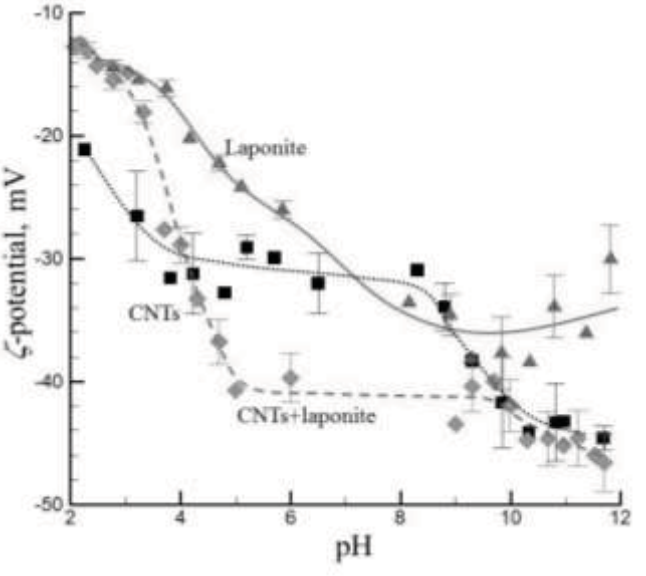

Figure 2. Electrokinetic potential, ζ, of CNTs (C_{CNT} = 0.01% wt), laponite platelets (0.05% wt) and CNT+laponite hybrid nanoparticles (C_{CNT} = 0.01% wt, X = 1) versus pH

The ζ-potential of laponite platelets at pH > 8 reached constant value. The observed changes may be explained by the impact of pH on the positive surface charge at the edges of laponite. These charges are generally screened by the diffuse part of the electric double layer (EDL) of laponite faces and decrease with pH increase and get neutralized at pH > 11 [17].

The behaviour of ζ-potential of CNT+laponite hybrid nanoparticles (X = 1, C_{CNT} = 0.01 wt %) at different pH value looks like that of CNTs suspension, but it has more negative value at pH > 4, and ζ-potential have constant value at the pH interval 5–10 ($\zeta \approx$ –42 mV). At pH > 10 the ζ-potential value of CNTs and CNT+laponite hybrid particles are the same. The observed behaviour of the ζ-potential can reflect immobilization of laponite platelets on the surface of CNTs.

The observed hetero-coagulation and formation of CNT+laponite hybrid particles evidently reflect the presence of attractive interactions between similarly charged species. Many theoretical and experimental works have reported that unusual attractive interactions can exist for similarly and highly charged colloidal particles (see, [18] for a review). The hetero-coagulation between similarly charged CNTs and laponite platelets can be related to highly heterogeneous distribution of the negatively charged functional groups on the surface of CNTs. The laponite platelets can be effectively immobilized on the neutral portion of CNT surface due to strong attractive electrostatic image forces between the charged particles and neutral graphite-like surface. From the other side, such hetero-coagulation can be also resulted from difference in ζ-potential value of laponite and CNT particles [19]. It should be noted that attractive interaction between negatively charged functional groups of CNT and positively charged edges of laponite are also presented.

Addition of KCl to the CNTsuspension gives an initial increase (up to $6.6 \cdot 10^{-3}$mol/dm^{3}KCl concentration) and then a decrease of the ζ-potential value (Figure 3*a*). The

presence of maximum at low ionic strengths of solution has been observed previously in different systems and it may be attributed to the influence of surface conductivity (*i.e.* the EDL polarization) on electrophoresis (see [20] for details).

Addition of a small amount of KCl (< $5\cdot10^{-4}$mol/dm^3) to laponite suspension results in insignificant decrease of the ζ-potential value, whereas increasing concentration of KCl (up to $5\cdot10^{-2}$mol/dm^3) does not change substantially the ζ-potential value of laponite platelets and at high KCl concentrations it turned to be equal to the ζ-potential value of laponite particles in pure laponite suspension (≈ –45 mV). The laponite clay platelets bear considerable negative surface charge (CEC ≈ 0.75 meq/g, ζ ≈ –45 mV), and their surface is strongly hydrated due to formation of H-bonds by water molecules with functional groups and hydrated Na^+-ions on the surface. So, discussing the influence of electrolytes on the ζ-potential of laponite particles several effects should be taken into consideration. Addition of KCl to laponite suspension results in an ion exchange in the EDL, *i.e.* substitution of the surface Na^+-ions by less hydrated, with higher adsorption affinity K^+-ions. It is accompanied by a decrease in hydration of the surface and shift of the shear plane toward the surface, i.e. by an increase of the ζ-potential value. With rising the KCl concentration the compression of the double layer increases, which gives a decrease of the electrokinetic potential. At the same time, an increase in the ionic strength at high electrolyte concentrations leads to destruction, thinning of the hydrate layers; dehydration of the surface results in an increase of the electrophoretic mobility. Such combination of these effects leads to non-conventional shape of the ζ(*C*) curve for KCl shown in Figure 3*a*.

The run of the ζ-potential of CNT+laponite hybrid nanoparticles at addition of KCl electrolyte (Figure 3*a*) is complex. An increase of KCl concentration up to $C_{KCl} < 5\cdot10^{-4}$ M gives a decrease in the ζ-potential value, and at $C_{KCl} > 1.7\cdot10^{-2}$ M increasing ζ-potential values were observed; similar behaviour of ζ-potential was observed for CNTs-containing suspension. At concentration of KCl$C_{KCl} = 5\cdot10^{-4}$ M the ζ-potential increased and stabilized at ≈ –35 mV up to $C_{KCl} = 1.7\cdot10^{-2}$ M.

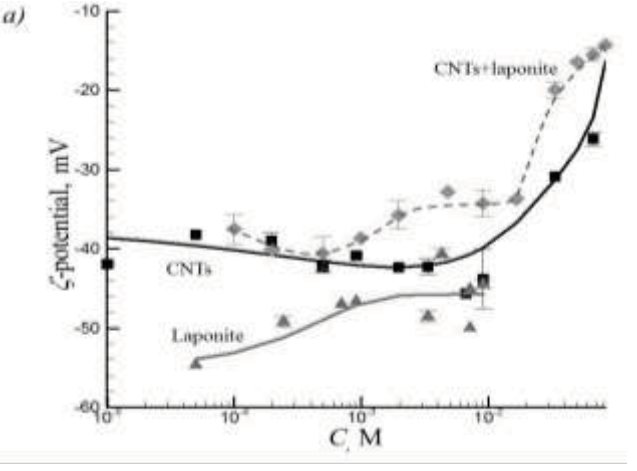

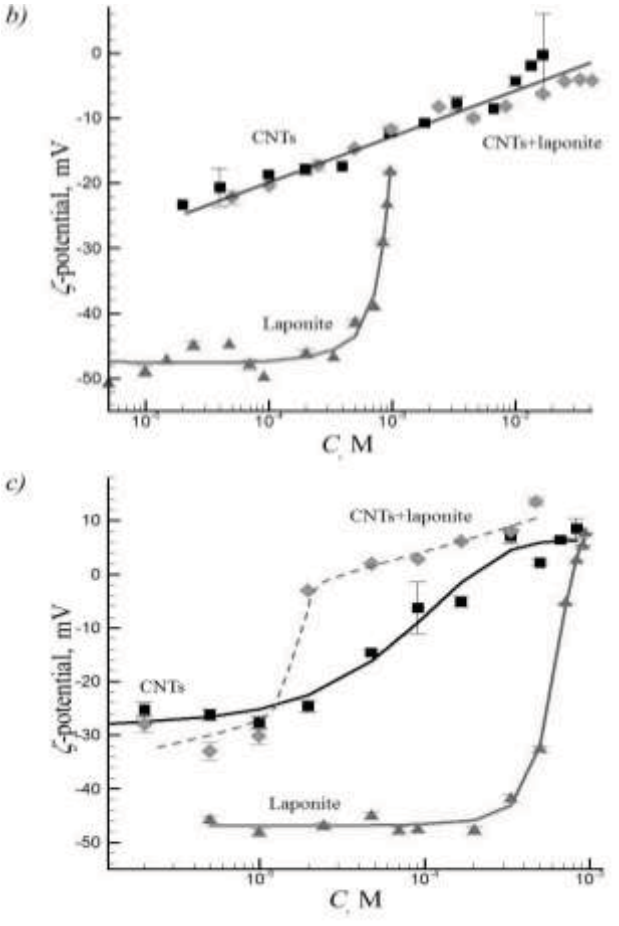

Figure 3. Electrokinetic potential, ζ, of CNTs (C_{CNT} = 0.01% wt), laponite platelets (2.0% wt) and CNT+laponite hybrid nanoparticles (C_{CNT} = 0.01% wt, X = 1) versus concentration of electrolyte, C, of KCl (a), $CaCl_2$ (b) and $AlCl_3$ (c)

Addition of bivalent counter-ions results in considerable decrease of the ζ-potential values (Figure 3*b*) and trivalent counter-ions cause charge reversal of the carbon nanotubes (Figure 3*c*). Such dependencies were obtained for a large number of different disperse systems [20]. Thus, we can state that carbon nanotubes behave in external electric field like typical hydrophobic colloidal systems.

Similarly, there are no substantial changes in the ζ-potential of laponite particles at low ($< 5 \cdot 10^{-3}$mol/dm^3) $CaCl_2$ (Figure 3*b*) or $AlCl_3$ (Figure 3*c*) concentrations in suspension. It can be explained by existence of thick, protective hydrate layers on the surface of particles; a marked effect of adsorption of counterions on the EDL structure, *i.e.*ζ-potential value, is observed at relatively high concentrations of electrolyte, at which surface hydrate layers are partially destroyed and much thinner. Sharp decrease of the ζ-potential value of laponite particles takes place at much higher levels of bi-, and trivalent ions than that typically observed for hydrophobic particles. The rise in concentration of trivalent Al^{3+}-ions results

in substantial decrease of the electrokinetic potential, and then an inversion of its sign, as it is typical for hydrophobic colloids and CNTs themselves.

It is interesting to note that the behaviour of CNT+laponite hybrid nanoparticles while adding electrolytes with bivalent (Figure 3*b*) and trivalent (Figure 3*c*) cations is the same as for the CNTs suspension. This testifies that the effect of adsorbed/adagulated laponite particles on the EDL parameters of CNT+laponite hybrid particles is relatively weak. At the same time the CNTs+laponite suspensions at optimal ratio of the components, $X = 1$, were stable against sedimentation. This evidenced that stabilization of CNTs suspension by laponite nanoparticles is caused mainly by non-electrostatic effects, *e.g.*, steric stabilization, hydrophilization of the surface *etc*.

Thus, there is a marked distinction between the effects of laponite on CNTs in electrolyte solutions in comparison to hydrophobic particles, *i.e.*, no effect on the electrokinetic potential at low concentrations and a steep decrease in the ζ value or its inversion at relatively high (higher than that in hydrophobic colloid [21]) content of the electrolyte. This can be explained by strong hydration of the surface of particles: substantial changes in the electrokinetic potential may take place in the case of partial destruction of the stabilizing hydrate layers.

Conclusions

The electrokinetic potential of carbon nanotubes and laponite as well as carbon nanotubes+laponite hybrid particles was measured as a function of pH and electrolytes concentration. It has been shown that the electrokinetic behaviour of carbon nanotubes resembles that of the lyophobic colloids. An increase in pH from 2 to 12 resulted in substantial increase of the absolute (negative) values of the zeta potential of carbon nanotubes due to dissociation of surface hydroxyl and carbonyl groups, which was identified by infra-red (IR) spectroscopy. The observed attraction between similarly charged colloidal particles of carbon nanotubes and laponite can be explained by the highly heterogeneous distribution of negatively charged functional groups on the surface of carbon nanotubes and difference in zeta potential of nanotubes and laponite particles.

Acknowledgement

This research was (partially) carried out in the framework of the cooperation agreement between the Hungarian Academy of Sciences and National Academy of Sciences of Ukraine. Authors thank Peter Pekker for help with HRTEM images.

References

[1] MURSHED, S. M. S.–CASTRO, C.A.N. de: Superior thermal features of carbon nanotubes-based nanofluids – A review. *Renew. Sustain. Energy Rev.,* 37, 2014, 155–167.

[2] CHEN, J.–ZHU, Z. H.–MA, Q.–LI, L:–RUDOLPH, V.–LU, G. Q.: Effects of pre-treatment in air microwave plasma on structur of CNTs and activity of Ru/CNTs catalysts for ammonia decomposition. *Catal. Today,* 148, 2009, 97–102.

[3] LIU, X.–WANG, M.–ZHANG, S.–PAN, B.: Application potential of carbon nanotubes in water treatment: A review. *J. Environ. Sci.,* 25, 2013, 1263–1280.

[4] WANG, Q.–ARASH, B.: A review on applications of carbon nanotubes and graphenes as nano-resonator sensors. *Comput. Mater. Sci.,* 82, 2014, 350–360.

[5] WANG, Y.–WANG, X.–WU, B.–ZHAO, Z.–YIN, F.–LI, S. et al.: Dispersion of single-walled carbon nanotubes in poly(diallyldimethylammonium chloride) for preparation of a glucose biosensor. *Sensors Actuators B,* 130, 2008, 809–815.

[6] BERGIN, S. D.–SUN, Z.–STREICH, P.–HAMILTON, J.–COLEMAN, J. N.: New solvents for nanotubes: Approaching the dispersibility of surfactants. *J. Phys. Chem. C,* 114, 2010, 231–237.

[7] KHARISSOVA, O. V.–KHARISOV, B. I.–CASAS ORTIZ, E. G. de: Dispersion of carbon nanotubes in water and non-aqueous solvents. *RSC Adv.,* 3, 2013, 24812–24852.

[8] MINGHUA, L:–HUANG, C. P.: Stability of oxidized single-walled carbon nanotubes in the presence of simple electrolytes and humic acid. *Carbon,* 48, 2010, 4527–4534.

[9] LOGINOV, M.–LEBOVKA, N.–VOROBIEV, E.: Laponite assisted dispersion of carbon nanotubes in water. *J. Colloid Interface Sci.,* 365, 2012, 127–136.

[10] LI, C.–SCHAFFER, A.–VEREECKEN, H.–HEGGEN, M.–JI, R.–KLUMPP, E.: Influences of perfluorooctanoic acid on the aggregation of multi-walled carbon nanotubes. *J. Environ. Sci.,* 25(3), 2013, 466–472.

[11] JU, L.–ZHANG, W.–WANG, X.–HU, J.–ZHANG, Y.: Aggregation kinetics of SDBS-dispersed carbon nanotubes in different aqueous suspensions. *Colloids Surfaces A Physicochem. Eng. Asp.,* 409, 2012, 159–166.

[12] SALECH, N. B.–PFEFFERLE, L. D.–MELECH, M. C.: Aggregation Kinetics of Multiwalled Carbon Nanotubes in Aquatic Systems: Measurements and Environmental Implications. *Environ. Sci. Technol.,* 42, 2008, 7963–7969.

[13] MA, P. C.–SIDDIQUI, N. A.–MADER, E.–KIM, J. K.: Correlation between electrokinetic potential, dispersibility, surface chemistry and energy of carbon nanotubes. *Compos. Sci. A. Techn.,* 71, 2011, 1644–1651.

[14] VANYOREK, L.–MÉSZÁROS, R.–BÁRÁNY, S.: Surface and electrosurface characterization of surface oxidized multi-walled N-doped carbon nanotubes. *Colloids Surfaces A Physicochem. Eng. Asp.,* 448, 2014, 140–146.

[15] MANILO, M.–LEBOVKA, N.–BÁRÁNY, S.: Characterization of the electric double layers of multi-walled carbon nanotubes, laponite and nanotube+laponite hybrids in aqueous suspensions. *Colloids Surfaces A Physicochem. Eng. Asp.,* 462, 2014, 211–216.

[16] THOMPSON, D. W.–BUTTERWORTH, J. T.: The nature of laponite and its aqueous dispersions. *J. Colloid Interface Sci.,* 151, 1992, 236–243.

[17] TAWARI, S. L.–KOCH, D. L.–COHEN, C.: Electrical double-layer effects on the Brownian diffusivity and aggregation rate of Laponite clay particles. *J. Colloid Interface Sci.,* 240, 2001, 54–66.

[18] LEBOVKA, N.: Aggregation of charged colloidal particles. In: MÜLLER, M. (Ed.): *Polyelectrolyte Complexes Dispersed Solid State Princ. Appl.* Springer, 2014, 1–40.

[19] DERJAGUIN, B. V.–CHURAEV, N. V.–MULLER, V. M.: *Surface Forces*. Springer Science+Business Media, New York, 1987.

[20] BÁRÁNY, S.: Complex electrosurface investigations of dispersed microphases. *Adv. Colloid A. Interf. Sci.,* 75, 1998, 45–78.

[21] LYKLEMA, J.: *Fundamentals of Interface and Colloid Science, Vol. II*. Academic Press, San Diego, 1995.

Materials Science and Engineering, Volume 40, No. 1 (2015) pp. 105–112.

AGGREGATION IN HYBRID SUSPENSION FILLED BY MIXTURE OF MULTI-WALLED CARBON NANOTUBES AND NANOPLATELETS OF LAPONITE

MARYNA MANILO[1]–NIKOLAI LEBOVKA[2]–SÁNDOR BÁRÁNY[3]

Aggregation in hybrid aqueous suspension filled by mixture of multi-walled carbon nanotubes and nanoplatelets of laponite as a function of the added different type of electrolytes (KCl, $CaCl_2$ and $AlCl_3$) and pH was studied in a flow system. The mass ratio of laponite/carbon nanotubes was varied between 0 and 1. The critical coagulation concentrations for hybrid carbon nanotube + laponite nanoparticles were estimated as $5 \cdot 10^{-3}$ M for KCl, 10^{-3} M for $CaCl_2$ and 10^{-5}M for $AlCl_3$. The ratio between critical coagulation concentrations for different electrolytes was very close to the value typical for aggregation of dispersed particles in the secondary minimum.
Keywords: carbon nanotubes, laponite platelets, aggregation, pH, electrolytes

Introduction

Carbon nanotubes (CNTs) represent great interest due to their unique structural and transporting properties, such as high tensile strength, modulus, electrical and thermal conductivities alongside with low density. CNTs are also suitable for preparation of carbon based catalysts, rechargeable batteries, super capacitors, lightweight electromagnetic shields, automotive parts, adsorbents and composites [1]. The technical application of nanotubes requires usage of highly dispersed and stabilized CNTs, without bundles or large aggregates. Well dispersed suspensions of CNTs are promising materials for preparation of new type of sensors and biosensors, membranes, microelectronic devices etc. Enhancement of the stability of CNT suspensions can be achieved using surface functionalization, adsorption of surfactants/polymers or heteroadagulation with nanoparticles.

For example, it has been shown [2, 3] that oxidative treatment by applying acids, hydrogen peroxide, ozone, *etc.* leads to formation of carboxyl and hydroxyl groups on the CNTs surface. Adsorption of polymers or surfactants helps to overcome attractive forces between the individual CNTs. This results in formation of more stable nanotubes suspensions, enhances de-bundling of CNTs and prevents re-aggregation. Stable dispersions of CNTs as a result of adsorption of poly(diallyldimethylammonium chloride) [4], sodium dodecylbenzene sulfonate [5], poly(ϵ-caprolactone) [6] and other polymers (for example, [7]) were obtained.

Also, adsorption of charged nanoparticles (*e.g.* montmorrilonite [8], laponite [9] or iron oxide [10]) can significantly improve the dispersability of CNTs in different media due to prevention of the nanotubes re-aggregation. Aggregation of CNTs decorated by soil minerals (kaolinite, smectite and shale) in aqueous suspensions at different sodium salt

[1] National Academy of Sciences of Ukraine, F. D. Ovcharenko Institute of Biocolloidal Chemistry
Kyiv 030142, Ukraine
assol_M@i.ua
[2] National Academy of Sciences of Ukraine, F. D. Ovcharenko Institute of Biocolloidal Chemistry
Kyiv 030142, Ukraine
[3]University of Miskolc, Institute of Chemistry
Miskolc-Egyetemváros 3515, Hungary

concentrations was investigated [11]. It was established that increasing ionic strength of the solution induced aggregation of CNT+mineral complexes, and the aggregation tendency correlated with the hydrophobic character/surface potential of soil particles.

The aim of our paper was to elucidate the mechanism of stabilization of CNTs suspensions by laponite platelets and aggregation kinetics in a flow system of hybrid CNT+laponite nanoparticles as well as CNTs and laponite in the presence of acid/base and different electrolytes.

1. Experimental Materials and Procedure

Multi-walled carbon nanotubes (CNTs) were produced by CVD method in the presence of Fe-Mo-Al catalyst and purified as described in [12]. Their structure and properties are described in [13].

Laponite, RD grade (Rockwood Additives Ltd., UK) is a synthetic clay with chemical formula $Na_{+0.7}[(Si_8Mg_{5.5}Li_{0.3})O_{20}(OH)_4]_{-0.7}$. It is composed of highly heterogeneously charged disk-like sheets with thickness ≈ 1 nm and average diameter ≈ 25–30 nm (see in detail our previous paper [13]).

All stock suspensions were prepared by using distilled water (pH~6.8). The effect of pH and concentration of electrolytes on the degree of aggregation of CNT+laponite nanoparticles at different mass ratios of laponite/CNT X was studied.

The aggregation experiments were performed using Photometric Dispersion Analyzer PDA 2000 (Rank Brothers Ltd, UK). CNT stock suspensions (C_{CNT} = 0.003 wt%) with/without decoration by laponite clay disks were sonicated during 5 min by using Heilscher Ultrasound Technology (amplitude was 20%). The principle of the PDA 2000 operation is described in [14, 15]. As a measure of aggregation the PDA 2000 R value has been used. R value permits quantification of aggregation or disaggregation of the nanoparticles in suspension and it represents the degree of aggregation of colloidal particles.

The preliminary experiments have shown that relatively stable suspensions of CNTs (not settling within several hours) can be obtained at stirring rate of 150 min^{-1} and CNTs content in suspension (C_{CNT}) in the range between 0.003 and 0.005 wt%. The PDA ratio, R, at these values of G and C_{CNT} can be well measured being within the measuring limits of the device. As a control, the aggregation behavior of 0.003 wt% stock suspension of CNTs and 2.0 wt% laponite suspension was measured.

ZetaSizer NS (Malvern, UK) was used for measurements of the size of laponite platelets. The instrument is suitable for determination of size distribution function $F(R)$ in the range of 0.3 nm–10 μm. Measurements of $F(R)$ are based on application of non-invasive back scatter technology.

2. Experimental Results and Discussion

Figure 1 shows the time dependence of the R in hybrid CNT+laponite suspensions at different mass ratio $X = m_L/m_{CNT}$. It is seen that the $R(t)$ dependencies are different while changing the CNT+laponite mass ratio. In "pure" CNTs suspension (X = 0) the value of R reached the maximum (≈ 10) and big quickly sedimenting aggregates were formed during the first two-three minutes of the process. At X = 0.2 the run of $R(t)$ plots was similar to that observed at X = 0, but the size of aggregates was smaller. At X = 0.5 relatively stable big aggregates were formed. The R value became constant after 5 minutes of aggregation and no sedimentation was observed. At X = 1 the value of R went through a maximum (R ≈ 3)

at $t \approx 12$ minutes of aggregation and the smallest size of aggregates was observed. These aggregates maintained high stability even after 20 min of aggregation. An appearance of a maximum on $R(t)$ curves for hybrid CNT+laponite particles can be attributed to formation of aggregates with different sizes [12]. The obtained data show that CNT particles covered with laponite platelets have higher aggregation stability and smaller size of aggregates compared to "pure" nanotubes suspension.

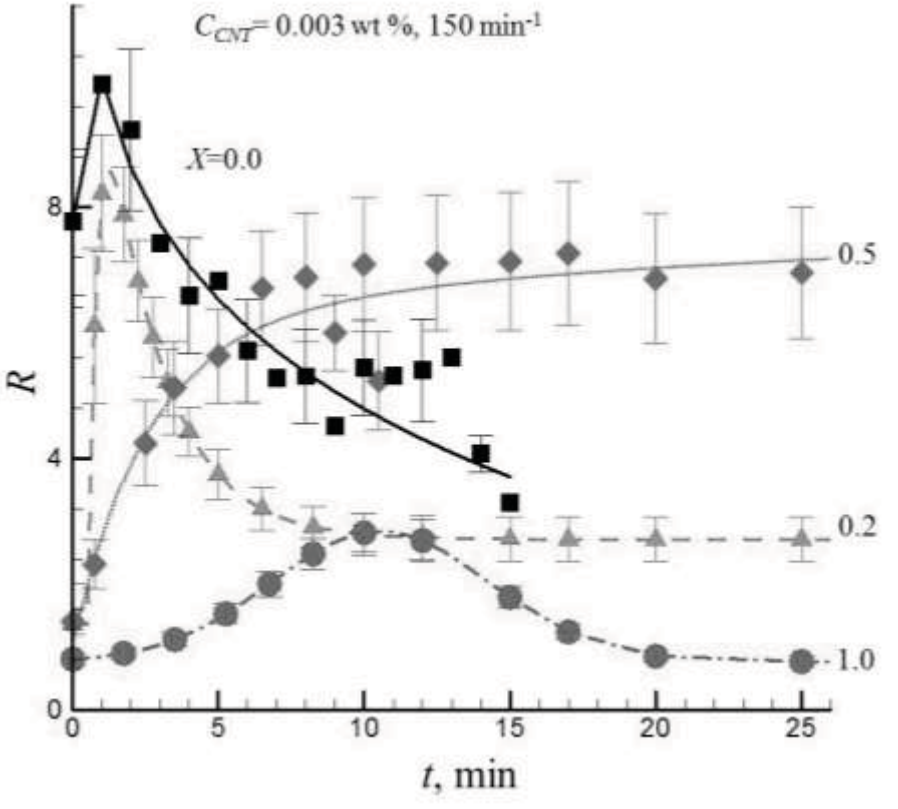

Figure 1. PDA ratio, R, versus the time of stirring, t, in hybrid aqueous CNTs+laponite suspensions at different mass ratio of laponite and CNTs, $X = m_L/m_{CNT}$. The stirring rate, G, was 150 min^{-1}, concentration of CNTs, C_{CNT}, was 0.003 wt% (pH 6.0)

Figure 2. illustrates the pH-dependence of the PDA ratio R in hybrid CNT+laponite suspensions as well as of that for CNTs and laponite at time $t = 10$ min.

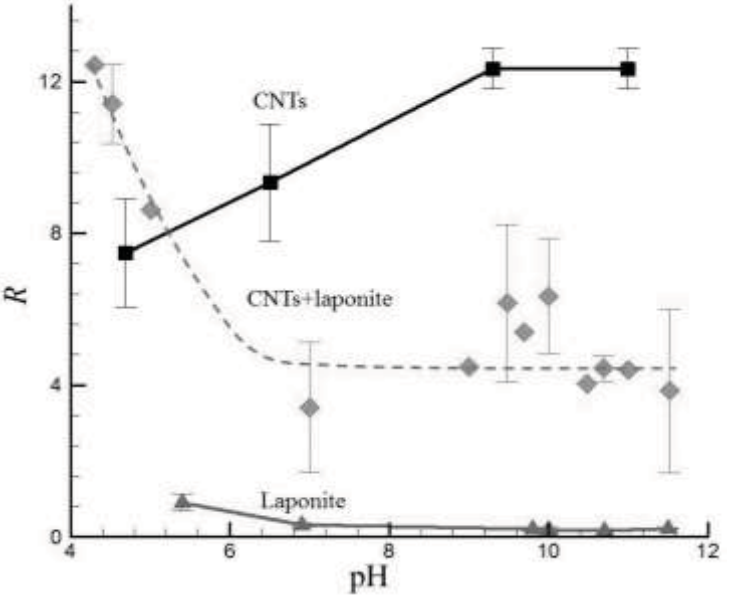

Figure 2. pH-dependence of the PDA ratio R in hybrid CNTs+laponite suspensions (C_{CNT} = 0.003 w%, X = 1.0) as well as CNTs (C_{CNT} = 0.003 wt%) and laponite (C_L = 2.0 wt%) at time t = 10 min

At acidic conditions (pH < 7.0) the *R* value of CNT+laponite hybrid nanoparticles decreases as pH increases. This can be explained by increasing the surface group dissociation, which results in an increase of repulsive forces between the CNT+laponite hybrid nanoparticles. It should be stressed that in the pH interval studied, the zeta potential of CNT+laponite hybrid nanoparticles preserves relatively high, roughly constant value (~–33 mV at pH 4.3 and ~–40 mV at pH 6.0). At pH ≥ 7.0 CNT+laponite hybrid nanoparticles have relatively stable *R* value. This can be explained by buffer properties of laponite and enhancement of aggregation stability of CNTs after adsorption of laponite platelets. An appearance of a maximum on *R*(*pH*) dependencies at pH = 9.0–11.0 may reflect both the increase of the CNT+laponite surface charge density that enhances the suspension stability and the suppression of the electrical double layer which decreasing the aggregative stability of the suspension.

The aggregation behavior of CNT+laponite nanoparticles is similar to that for laponite (but have a maximum at pH = 9.0–11.0), while aggregation of CNTs increases as pH increasing. It should be noted that the stability of CNTs suspension is very sensitive to the pH value of the suspension with maximum aggregation at basic conditions. Such effect can be explained by existence of functional (phenolic hydroxyl) groups on theCNTs surface [12], which deprotonation enhanced aggregation.

Lowering the pH value of laponite suspension to 4.9 resulted in a slight increase of *R* (from 0.22 to 0.62), *i.e.* in a weak aggregation. A further decrease of pH did not change the degree of aggregation of the laponite suspension while increasing the pH (up to 12) has no influence on aggregation, because of increasing pH value resulted in the decrease of the positive charge density on the edge of laponite (and its neutralization at pH 11.0). It was shown [16] that in the pH interval 3.0–10.0, the pH value does not play role in the laponite

dissolution. At pH > 10.0, the dissolution of laponite was observed only at low concentrations (1.0 and 1.7 wt%), while for laponite suspension of high concentration (2.8 wt%) no dissolution was observed.

Figure 3 shows the dependence of the PDA ratio *R* vs electrolyte concentration in hybrid CNT+laponite suspensions as well as CNTs and laponite at fixed time.

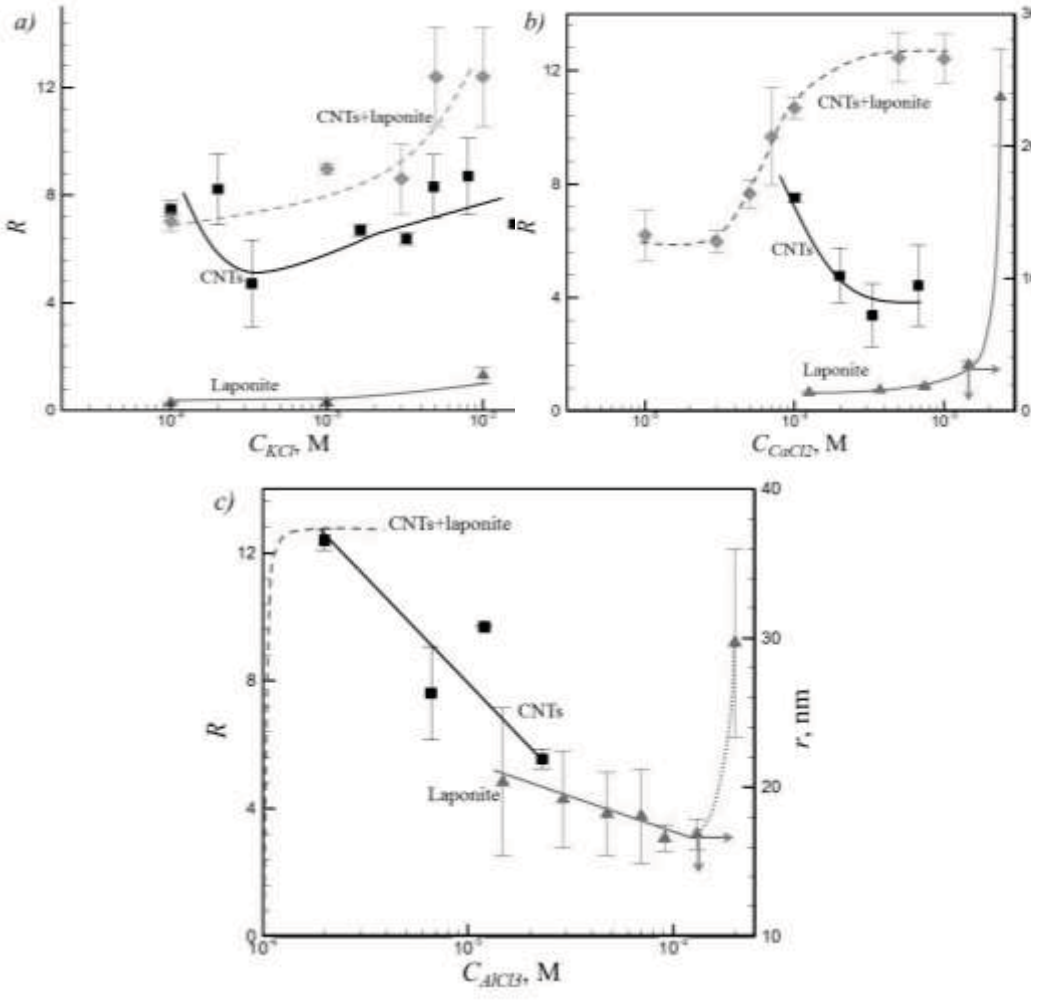

Figure 3. R values in hybrid CNT+laponite suspensions (C_{CNT} = 0.003 wt%, X = 1.0), CNTs (C_{CNT} = 0.003 wt%) and laponite (C_L = 2.0 wt%) vs electrolyte concentration, C, of KCl (a), $CaCl_2$ (b) and $AlCl_3$ (c) at fixed time t = 10 min. For laponite thedependence of radii of nanoparticles vs concentration of $CaCl_2$ (b) and $AlCl_3$ (c) is shown

An increase of the KCl concentration (Figure 3*a*) resulted in decrease of the aggregation stability in hybrid CNT+laponite suspensions which is reflected in rising *R* values and reached the maximum *R* value (≈ 12) at $C_{KCl} = 5 \cdot 10^{-3}$ M. A further rise in the KCl concentration up to 10^{-2} M did not change the *R* value substantially. This means that the

concentration of order of ≈ $5 \cdot 10^{-3}$ M KCl can be considered as a critical coagulation concentration (*CCC*) for fast coagulation.

For 2 wt% laponite suspension, the *CCC* of KCl was 10^{-2} M, *i.e*. it was higher than that for the CNT+laponite hybrid particles. This indicates that covering the CNT surface by laponite platelets does not result in appearance of properties of the "pure" laponite as it is often observed during heteroadagulation of small and big particles or adsorption of polyelectrolytes [17, 18]. This consideration is supported by the fact that the electrokinetic potential of laponite platelets (~-48 mV) and CNT+laponite complex (~–33 mV) are different [12].

Figures 3*b* and 3*c* show that the behavior of the PDA ratio *R* in hybrid CNT+laponite suspensions at different concentration of $CaCl_2$ and $AlCl_3$ are similar. From these data the *CCC* in the CNT+laponite hybrid suspensions were estimated as ≈ 10^{-3} M and ≈ 10^{-5} M for electrolytes with di- and trivalent counterions. It is important to note that the CCC values for KCl (CCC_1) and $CaCl_2$ (CCC_2) electrolytes differ only by 5 times. It is much smaller than the ratio $CCC_1/CCC_2 = 64$ that follows from prediction of the DLVO theory for concentration coagulation of small particles in the primary minimum (Schulze–Hardy rule). It is known that for coagulation of big particles in the secondary minimum the product $CCCz^{2.5\text{-}3.5}$ is constant approximately, where *z* is the valence of counterions [19]. Our experimental estimation $CCC_1/CCC_2 \approx 5$ is very close to the $CCCz^{2.5} = 5.66$ criterion. It evidenced the presence of aggregation of CNT+laponite hybrid particles in the secondary minimum.

It is important to note that CNT+laponite nanoparticles were not stable in the presence of even a very small amount of Al^{3+} ions (10^{-5}–10^{-4} M) (Figure 3*c*). This can be explained by complex formation between laponite platelets via Al^{3+} bridging. Also neutralization coagulation of CNT+laponite complexes can be supposed. This assumption is supported by the fact that zeta potential of the complex at 10^{-5} M Al^{3+} was nearly zero (≥ –3 mV). It is worthwhile to mention here that the term "coagulation concentration" of trivalent ions at concentrations 10^{-5}–10^{-4} M loses its sense because at these conditions typically the whole added amount of the reagent is adsorbed by dispersed particles and the equilibrium concentration of trivalent ions in the solution is zero [20]. This is also applies to adsorption of Al^{3+} ions by CNT+laponite hybrid particles.

Investigations of the aggregation stability of CNTs show that the degree of aggregation of nanotubes decreases with increasing concentration of electrolytes. This can be attributed to different effects: suppression of the EDL, *i.e.* concentration coagulation by 1-1 and, in part, by 2–1 electrolytes, reduction of the surface charge and potential by trivalent electrolytes ("neutralization" coagulation). Also chemical interactions between the functional groups on the CNTs surface and the multivalent ions, specifically, Ca^{2+} and Al^{3+} should be taken into account. Adsorption of multivalent ions can lead to difference in the experimentally measured critical coagulation concentration ratio and that predicted by the Schulze–Hardy rule [21, 22].

Addition of electrolytes to laponite suspension results in a reduction of the thickness of the electrical double layer of particles and formation of the stable gel structure due to changing the orientation of clay particles from edge-to-face to face-to-face. Addition of Al^{3+} can also enhance aggregation of laponite nanoparticles by formation of a precipitate.

Conclusions

Aqueous suspensions of CNTs exhibit low aggregation stability because of strong van der Waals and hydrophobic attractive forces between individual nanotubes. We have shown that relatively stable suspensions of CNTs (not settling within several hours) can be obtained after intensive sonication and using stirring (by magnetic stirrer) with rate of 150 min^{-1} at nanotubes content of 0.003–0.005 wt%. Also it has been shown that addition of laponite in amount of higher than 50% mass fraction of CNT produces stable aqueous suspensions. The CNT+laponite hybrid particles can be coagulated by addition of electrolytes or base/acid reagents. An increase of pH value decreases the degree of aggregation of particles. This is explained by an increase of dissociation of the surface groups, *i.e.* by an increase of repulsive forces between the CNT+laponite hybrid particles. A maximum on aggregation curves versus pH can be reflect an increase of the CNT+laponite surface charge density (that enhances the stability of the suspension) and suppression of the electrical double layer (which decreases the suspension stability).

From the dependencies of the PDA ratio R (*i.e.* degree of aggregation) in hybrid CNT+laponite suspensions (C_{NT} = 0.003 wt%, X = 1.0) at different amount of electrolytes, the critical coagulation concentrations for KCl ($CCC_1 = 5 \cdot 10^{-3}$ M), $CaCl_2$ ($CCC_2 = 10^{-3}$ M) and $AlCl_3$ ($CCC_3 = 10^{-5}$ M) were estimated. The ratio of $CCC_1/CCC_2 \approx 5$ is very close to the $CCC2^{2.5} = 5.66$ criterion. It is evidence that the aggregation of CNT+laponite hybrid particles occurs in the secondary minimum.

Acknowledgement

This research was (partially) carried out in the framework of the cooperation agreement between the Hungarian Academy of Sciences and National Academy of Sciences of Ukraine.

References

[1] VOLDER, M.F.L. De –TAWFICK, S. H.–BAUGHMAN, R. H.–HART, A. J.: Carbon nanotubes: Present and future commercial applications. *Science,* 339, 2013 535–553.

[2] TASIS, D.–TAGMATARCHIS, N.–BIANCO, A.–PRATO, M.: Chemistry of carbon nanotubes. *Chem. Rev.,* 106(3), 2006, 1105–1136.

[3] BIKIARIS. D.–VASSILIOU, A.–CHRISSAFIS, K.–PARASKEVOPOULOS, K. M.: Effect of acid treated multi-walled carbon nanotubes on the mechanical , permeability , thermal properties and thermo-oxidative stability of isotactic polypropylene. *Polym. Degrad. Stab.,* 93, 2008, 952–967.

[4] WANG, Y.–WANG, X.–WU, B.–ZHAO, Z.–YIN, F.–LI, S. et al.: Dispersion of single-walled carbon nanotubes in poly(diallyldimethylammonium chloride) for preparation of a glucose biosensor. *Sensors Actuators B Chem.,* 130, 2008, 809–815.

[5] BERGIN, S. D.–NICOLOSI, V.–CATHCART, H.–LOTYA, M.–RICKARD, D.–SUN, Z. et al.: Large Populations of Individual Nanotubes in Surfactant-Based Dispersions without the Need for Ultracentrifugation. *J. Phys. Chem. C,* 112, 2008, 972–977.

[6] MITCHELL, C. A.–KRISHNAMOORTI, R.: Dispersion of Single-Walled Carbon Nanotubes in Poly(ϵ-caprolactone). *Macromolecules,* 40, 2007, 1538–1545.

[7] GOH, P. S.–NG, B. C.–ISMAIL, A. F.–AZIZ, M.–SANIP, S. M.: Surfactant dispersed multi-walled carbon nanotube/polyetherimide nanocomposite membrane. *Solid State Sci.,* 12, 2010, 2155–2162.

[8] WANG, Z.–MENG, X.–LI, J.–DU, X.–LI, S.–JIANG, Z. et al.: A simple method for preparing carbon nanotubes/clay hybrids in water. *J. Phys. Chem. C,* 113, 2009, 8058–8064.

[9] LOGINOV, M.–LEBOVKA, N.–VOROBIEV, E.: Laponite assisted dispersion of carbon nanotubes in water. *J. Colloid Interface Sci.,* 365, 2012, 127–136.

[10] GONG, J.-J.–WANG, Bin–ZENG, G.-M.–YANG, C.-P.–NIU, C.-G.–NIU, Q.-Y. et al.: Removal of cationic dyes from aqueous solution using magnetic multi-wall carbon nanotube nanocomposite as adsorbent. *J. Hazard. Mater.,* 164, 2009, 1517–1522.

[11] ZHANG, L:–PETERSEN, E. J.–ZHANG, W.–CHEN, Y.–CABRERA, M.–HUANG, Q.: Interactions of 14C-labeled multi-walled carbon nanotubes with soil minerals in water. *Environ. Pollut*., 166, 2012, 75–81.

[12] MANILO, M.–LEBOVKA, N.–BÁRÁNY, S.: Characterization of the electric double layers of multi-walled carbon nanotubes, laponite and nanotube; laponite hybrids in aqueous suspensions. *Colloids Surfaces A Physicochem. Eng. Asp.,* 462, 2014, 211–216.

[13] MANILO, M.–LEBOVKA, N.–BÁRÁNY, S.: Electrokinetic study of impact of laponite platelets on stabilization of carbon nanotubes in aqueous suspensions. *Mater. Sci. Eng.,* 2015, *In press*.

[14] GREGORY, J.: Turbidity fluctuations in flowing suspensions. *J. Colloid Interface Sci.,* 105 (2), 1985, 357–371.

[15] BÁRÁNY, S.–GREGORY, J.: Flocculation of kaolin suspension by cationic polyelectrolites. *Colloid J*., 58 (1), 1996, 13–18.

[16] JATAV, S.–JOSHI, Y. M.: Chemical stability of Laponite in aqueous media. *Appl. Clay Sci.,* 97–98, 2014, 72–77.

[17] BARAN, A. A.–GLOBA, L. I.: Interaction of microorganisms with dispersed particles. In: Ucl, L. (Ed.): *Proc. Intern. Conf. Colloids Aquatic Environ.* 1992, 89–93.

[18] BARAN, A. A.–PLATONOV, B. E.: Electrosurface characteristics of polymer containing dispersed systems. *Uspekhi Khimii (Russian Chem. Rev.),* 50, 1981, 161–191.

[19] DERJAGIN, B. V.: *The theory of stability of colloids and thin films.* Plenum Press, NY, 1989.

[20] BARANY, S.: Complex electrosurface investigations of dispersed microphases. *Adv. Colloid A. Interf. Sci.,* 75, 1998, 45–78.

[21] MINGHUA, L.–HUANG, C. P.: Stability of oxidized single-walled carbon nanotubes in the presence of simple electrolytes and humic acid. *Carbon,* 48, 2010, 4527–4534.

[22] SANO, M.–OKAMURA, J.–SHINKAI, S.: Colloidal Nature of Single-Walled Carbon Nanotubes in Electrolyte Solution: The Schulze–Hardy Rule. *Langmuir*, 17, 2001, 7172–7173.

Materials Science and Engineering, Volume 40, No. 1 (2015) pp. 113–125.

EFFECTS OF DIFFERENT FUEL TYPES ON THE OPERATIONAL PARAMETERS OF A BIOMASS BOILER

CSABA PÓLISKA[1]–PÉTER KÓKAI[2]–BERNADETT CSORDÁS[3]

Modern district heating systems represent an attractive alternative for the local population in accommodating their demand for thermal energy. In case thermal energy is generated in biomass combustion units (biomass boilers), it contributes to the reduction of pollutant emission associated with the burning of fossil fuels.

In this study, a wood chip boiler of 3MW net capacity is examined, the heating performance of which dropped drastically due to the depositions formed on the internal chamotte lining. Our aim was to investigate the exact reasons that lead to continuous slag formation and growth during operation. We were looking for correlations between the various fuels combusted, the operational parameters of the boiler and the slags formed.

After determining the combustion parameters of the fuels used, samples were prepared of the fuel ashes and the slags to examine the softening characteristics. The structure and composition of the ash samples were analysedby scanning electron microscopy. Based on the results, conclusions were drawn and potential measures have been proposed.

Keyworlds: biomass boiler, wood chips, slag

1. Introduction

The optimal way to provide buildings with heating and domestic hot water is a central question for many countries in the world. While pointing out the “best fit” andmost appropriate energy systems is still a hotly debated issue, there is a general consensuson the point that fossil fuel combustion should bedrastically cut. Some go as far as designing systems based up to 100% on renewable fuels [1]. Various approaches promote the construction of low- or zero-energy buildings, while others advocate the efficient utilization of renewable energy resources and waste heat generated as the by-product of various industrial activities. The latter solution inevitably involves the transmission of centrally produced thermal energy to end-users via district heating systems. District heating systems (DHS) are based on a central heating plant, which provides the adjacent buildings with thermal energy and domestic hot water [2]. Using advanced high-efficiency biomass boilers, the primary energy consumption of the district can be considerably reduced, while a higher level of energy efficiency can be achieved. These benefits compensate for the environmental risks associated with the operation of such boilers [3], 4].

The use of hydrocarbons, more specifically of natural gas is predominant in the energy structure of Hungary. Gas plays a significant role in heat production, mainly in the domestic sector which is up to 90% dependent on this fuel type. Most district heating plants

[1] University of Miskolc, Department of CombustionTechnology and ThermalEnergy,
Miskolc-Egyetemváros 3515, Hungary
tuzcsaba@uni-miskolc.hu
[2] MiskolciHőszolgáltatásiKft.
Miskolc 3534, Hungary
kokai.peter@miho.hu
[3] University of Miskolc, Department of CombustionTechnology and ThermalEnergy,
Miskolc-Egyetemváros 3515, Hungary
bernadett.csordas.p@gmail.com

(> 80%) operate on import gas, whereas Hungary has no effect whats oever on market trends and price fluctuations. In order to reduce the country's import dependency and exposure torising fuel price, it is critical that fully fossil-based thermal energy production be at least partially converted to renewable-based supply systems. One potential route is to involve biomass as fuel in district heating. Biomass-based district heating systems are being operated successfully all over Europe, and a growing number of Hungarian towns are planning to implement similar networks [5], 6, 7, 8]. It is important to emphasize that – along withthe reduction of fossil fuel dependency – the utilization of biomass sources creates new workplaces locally, promoting social and economic progress within the given community [9].

MIHŐ short for MiskolciHőszolgáltatóKft. (Miskolc District Heating Supplier LLC) is a public service provider, operating the second biggest district heating system in Hungary and providing heat to about 32,000 households and 1,200 public institutions.

Until recently, district heating had been exclusively covered from natural gas in Miskolc. The installation of a new heating system based on depot gas fuel in the Hejőcsaba housing area in 2008, marked a small step towards a more diversified supply system (of hardly more than 0.1%). In 2009, the local policy-makers decided on the substitution of gas-based thermal energy with alternative fuels. The first milestone on this road was a green-field investment, namely the construction of a 3 MW capacity boiler based on woodchip combustion in the Kenderföld district of Miskolc.

1.1. The biomass boiler of the 'Kenderföld' heating plant

The biomass combustion unit of the 'Kenderföld' heating plant is a Binder RRK 2500-3000/6 type woodchip boiler, equipped with a grate shaker and a multicyclone flue gas filter.The boiler block consists of three distinctive parts: the foundation ring, the combustion chamber and the heat exchanger. The foundation holds the grate, accommodates the primary air fan and other units like hydraulic rams. The combustion chamber is located on top of the foundation ring and its internal space is divided by a vault. The topmost part of the boiler block contains horizontally installed heat exchangers, where heat exchange from the flue gas is actually realized.

Transportation augers transmit the fuel first to the feeding screws, then in the Stoker screw, from which the fuel is fed into the furnace. Feed-in is actually realized on surface of the grate. The Stoker screw is located in a tube equipped with temperature sensors (the control units prevent the fire from spreading in case of burn-back). Actual combustion takes place on inclined multiple section reciprocating grates, that are operated by a hydraulic apparatus. The moving grates and the feeding augers ensure continuous fuel transport. Through the nozzles between the grate layers, primary air is blown in two portions from below. Ash is removed from the boiler and transported to the storage place by an ash auger located at the end of the grates. NiCrNi K-type thermocouples are placed within the two chambers to measure the temperature of the combustion unit. In the lower chamber, a temperature of approximately 600–650 °C is achieved, which allows for partial combustion and gasification of the fuel. The softening of various minerals already begins at this temperature.

Once the fuel is burned off in the lower chamber, the produced gases got into the upper chamber whereto air is pumped from the two sides to ensure complete burning. By supplying secondary air, chamber temperature can be raised to 1000–1100 °C. The addition of secondary air and the bottleneck effect caused by the internal vault enhances flow velocity. Part of the mineral content gets melt due to high temperature, and in molten phase

it readily mingles with the ash and fly ash produced from biomass. On leaving the upper chamber and entering the third chamber, this cohesive substance adheres to the wall of the boiler. This can be explained by a drop in flowrate i.e. the fact that the molten substance leaves the narrow upper chamber at high velocity and arrives at a more spacious area, thus losing momentum as flue gas velocity decreases in the wider space. Another factor contributing to slag formation is the mass of the substance constituted by the molten conglomerate. This matter then clashes onto the wall, where it is deposited layer by layer in a dome shape. The deposition grows, gets compacted and acts as an insulation layer on the wall, causing efficiency loss during operation. It also gravely influences the flow parameters of the flue gases. Moreover the slags achieve very high strength when cooled, unavoidably making damage to the chamotte lining during removal.

On leaving the upper chamber, the flue gas flows to the heat exchangers. The thermal energy of the flue gas gets transmitted to the water contained in the boiler system. Efficient heat recovery is actually realized in this section of the boiler; the flow direction of the flue gas is reversed several times with the help of reverse-flow tube configuration. Only the flue gas and the ash transported reaches the third chamber, where no moreslag formation is seen. In this final section, tubes are functioning as heat exchangers, but no point is installed for temperature measurement, therefore, the exact temperature of the flue gas is not known. The temperature of the exiting flue gas is however 150–180 °C. A flue gas fan helps venting the gas out of the chamber by creating vacuum pressure.It also assists in separatingthecombustion products (flyash)in the dust separator cyclone. Should the temperature in the bottom combustion chamber become higher than optimal,part of the flue gas is recirculated into the primary air supply. This helpsreducing the temperature in the lower combustion chamber. If, however, the temperature in the bottom combustion chamber is lower than that required for recirculation, then the clappersat the air inlets shut down and no recirculation into primary airflow takes place.

1.2. Experiences on operation

The boiler was put into operation in December 2011. From January 2012, trial combustions were run and from February 2012, commercial operation started. The start-up phase of the boiler was relatively short and had gone without difficulties, however, problems started to appear during continuous operation, as listed below.

As set out in the preliminary plans, the fuel used in the beginning was urban green waste consisting of bushes and trees from felling, chipped roots and logs and similar contaminanted fibrous substance. This feedstock got stuck at various points of the fuel auger leading to an automatic shut down of the boiler.

Moreover, the net calorific value of these poor quality fuels was far below theexpectations, with an ash and moisture content higher than optimal.Although complete burning took place, the power output hardly reached 1 MW and several problems occuredduring continuous operation.

High ash content,the lack of adjustment inexcess air parameters and inappropriate setting of the automatic control also contributed to a lot of problems during operation. Flue gas temperatures up to 160–200 °C reduced the efficiency of the boiler and the emission of dust particles was sometimes of noticable volume. The continuous deposition of ash and fly ash in the lower and upper chambers were likely due to inadequate fuel quality and overtemperature. Burning on, the slags formed domes and obstructions in the combustion chamber.Instead of the maintenance work scheduled for every 6 weeks, this made weekly shutdownsnecessary, to breakup and remove the deposits. Apart from malfunction of the

unit and its financial impacts, the problem was significant since it caused serious damage to the refractory lining.

The problems that lead to efficiency loss due to deposit formation are summarized as follows:

- The direction and flow velocity of the flue gas flow was modified mostly due to reduced flow cross-section.
- The heat conductivity of the slag deposited on the wall was very poor, thus thermal transmittance of the wall was significantly reduced.
- Strong chemical bonds were established between the deposition and the boiler wall, therefore slag removal resulted in serious damage to the refractory wall.
- Note that apart from causing efficiency loss, the latter problem also reduced boiler life expectancy. The next section primarily focuses on the reasons for slag formation and gives an overview of the applied test methods.

2. Test samples

2.1. Wood chips

Considering a biomass heating plant, one of the most important economic factors is the purchase price of fuel. For biomass feedstock (woodchips), thismay vary considerably, depending primarily on fuel quality and transportation distance [10]. Other important parameters are relatively high moisture content and subsequent low heating value, low density and inhomogenous chips size, which may considerably increase transport costs [9], 10, 11].

Due to the above reasons, 5 different types of chips were supplied toand combusted in the Miskolc heating plant over a few month. The chips came from various sources from within an area of 100 kms from Miskolc. The most important features of chips are summmarized in Table 1.

Fuel analyses were carried out according to the ISO standards. For proximate analysis, programmable laboratory furnaces were used (MSZ ISO 1171), for ultimate analysis Carlo Erba EA 1108 type analyzers and for calorific value, a Parr type calorimeter was applied. Biomass ashes were produced using the standard test method.

Table 1

Fuels used in the boiler during the period under study

	Pine	**Hardwood #1**	**Hardwood #2**	**Mixed wood chips**	**Wood residue chips**
Origin	State-owned forest activity	State-owned forest activity	State owned forest activity	Private forest activity	State-owned forest activity
Type	90% pine, 10% hardwood	90% hardwood, 10% other	100% hardwood	Mixed hardwood, softwood, fruit wood, pine	Crown and twig part of the pine, mixed hardwood, and softwood

	Pine	**Hardwood #1**	**Hardwood #2**	**Mixed wood chips**	**Wood residue chips**
Chipper	Knife cutters	Knife cutters	Knife cutters	Knife cutters	Knife cutters
Size	G70-G100	G50-G70	G50	G70-G100	G20-G50
Moisture cont.	< 35%	30–45%	< 35%	< 35%	30–40%
Ash content	< 1%	1%	1%	1–2%	3–5%
Homogeneity	80%	90%	100%	50%	50%
Contaminants content	1%	3–5%	1%	3–5%	10–15%
Firing experience	Excellent, but some unburned content melted into the surface of the upper firing chamber	Good	Excellent	Good, but there were a few problems with the feeding screw	Acceptable, problems in the feeding system and the ash removal system

2.2. Slags

Based on operational experience, one of the most critical phases of the combustion process is slag formation caused byunburnt inorganic particles found in the solid combustion residues of the fuel. Fuels do contain a variety of such components (K, Na, Si, Al, Ca, Mg, etc.) and so does the combustion residues of biomass fuels. Ash depositions involving inorganic elements are tackier, harder and less porous, with a smooth surface, whichmakes their removal quite difficult. Out of the chemical compounds found in the K_2O-CaO-SiO_2 ternary diagram, particularly potassium silicate has an extremely low melting point (at about 700 °C) [14].

The most typical slag types are presented in the images below (Figure 1).The glassy slag is hard, rigid, dense and of a glassy structure, while the porous slag has amuch looser, porous structure.

a) Glassy slag

b) Porous slag

Figure 1. Depositions (from the 'Kenderföld' boiler) with different microstructure and morphology

3. Results and discussion

3.1. Characterization of fuels

Hygroscopic moisture and ash content, chemical composition and calorific values of the fuels used in the period under examination are summarized in Table 2.

Table2

Proximate analysis, ultimate analysis and calorific values of the biomass fuels

Sample	W % m/m	Ash % m/m	C % m/m	H % m/m	N % m/m	O % m/m	S % m/m	GCV* MJ/kg
Pine	8.85	0.36	50.02	6.36	0.02	34.36	0.023	17.88
Hardwood #1	12.64	1.90	46.56	5.28	0.18	33.18	0.253	15.40
Hardwood #2	9.30	1.03	48.76	5.99	0.30	34.56	0.040	17.13
Mixed wood chips	8.17	1.69	47.19	6.13	0.03	36.73	0.053	17.24
Wood residue chips	10.99	4.00	46.25	5.79	0.37	32.61	< 0.01	15.79

**Gross calorific value*

The hygroscopic moisture content of the fuels is ~ 10% m/m.Pine wood has the lowest ash content, whilechipped twigs have the highest. This is obvious, considering the high proportion of bark, logging residues andother kinds of forestry waste gettingcommingled with the latter.Ultimate analysis shows that the percentages of carbon, hydrogen nitrogen and oxigenarecomparable in all samples. All samples are characterized by a very low sulphur content (0.01–0.25%) implying that SOx emissions during combustion are of no concern for these fuels [15]. The tested biomass fuels gave an average heat value of 16.6 MJ/kg. The lowest values were obtained for the two samples where hygroscopic moisture and ash content were above the average.

3.2. Softening characteristics

The softening and melting parameters of the ashes and slags were determined with a Sylab IF 2000G ash fusion analyzer and an IRF 1500 furnace attached to it. The morphological changes of the ash and slag samples were recorded with a digital camera. The instrument allows for the execution of standardized measurements according to CEN/TS 15370-1-2006, ISO 540 1995, ASTM E 953-8(2004), AFNOR M03048, BRITISH1016-70, AS 1038.15, DIN 51730.

Melting features were characterized with the specific temperature points given below:

- Initial Deformation Temperature (IT): the temperature at which the tip of the test sample shows a 5% shrinkage in height as compared to the original height of the test sample,
- Deformation Temperature (DT): the temperature at which the test sample starts to fuse into a hemispherical shape with edges and corners starting to round off,
- Softening temperature (ST): the temperature at which signs of softening (change in surface, rounding of edges) start appearing, the test sample starts blowing up,

- Hemispherical temperature (HT): the temperature at which the shape of the test sample resembles a hemisphere, the hight of the test sample is equal to 1/2 of the width of the base,
- Fluid temperature (FT): the temperature at which the sample height shrinks to 1/3 of the original height, i.e. the sample melts.

The softening parameters of the prepared ash samples and of the as-received depositions are shown in Table 3.

Table 3

Softening parameters of ashes of wood chips and slags (°C)

	Sample	**IT**	**DT**	**ST**	**HT**	**FT**
Wood chips	Pine	1370	1410	–	1530	1535
	Hardwood #1	1353	1463	–	1532	1542
	Hardwood #2	1205	1371	–	1528	1543
	Mixed wood chips	1203	1354	–	1513	1528
	Wood residue chips	1182	1204	1304	1319	1346
Slags	Glassy slag	1152	1216	1228	1233	1255
	Porous slag	1092	1178	1196	1208	1231

The deformation temperatures of ashes of wood chips, with the exception of wood residue chips, were higher than 1200 °C, with HT and IT temperatures well over 1500 °C, just as expected. Wood residue chips started melting at a lower temperature and over 1300 °C they were practically molten. However, considering the fact that the normal operational temperature of the boiler is maximized in 1000 °C, this hardly explains for slag formation.

3.3. Ash and slags characterization using scanning electron microscopy – energy dispersive spectroscopy

The ash and slag samples were experimentally observed to confirm our assumptions based on the fusibility properties. For the characterization of the samples, scanning electron microscopy and energy dispersive spectroscopy (SEM/EDS) analyses were performed. A high resolution Zeiss Evo MA10 scanning electron microscope was used, and samples were coated with a thin gold layer in order to obtain the conductivity needed for SEM observation. This type of sample preparation allowed us to observe the morphology of the agglomerates, and to identify the major elements that may be responsible for the melting effects. The software included in the SEM equipment provided data acquisition for semi-quantitative analysis. In sum, it can be said that the ash composition of the examined wood chips corresponds to literary data [16] 17].

SEM images of the samples taken from ashes of wood chips are presented below (Figure 2), displaying average composition and the composition of marked points specifically (Table 4).

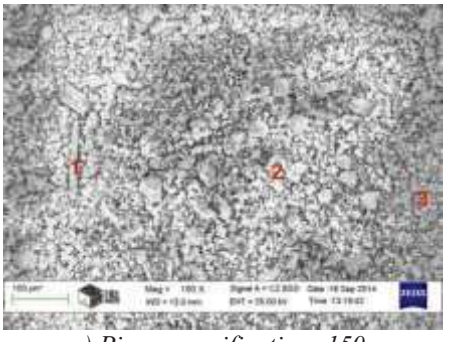

a) Pine, magnification: 150x

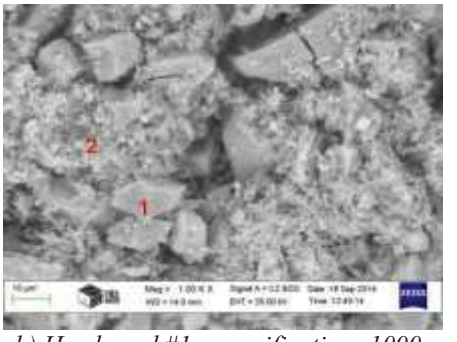

b) Hardwood #1, magnification: 1000x

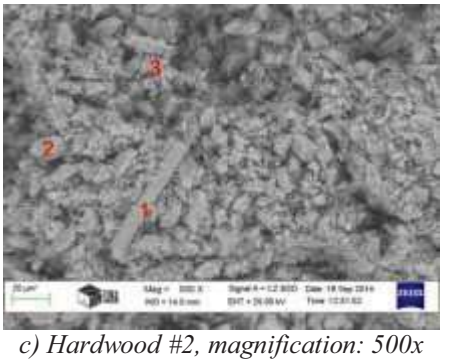

c) Hardwood #2, magnification: 500x

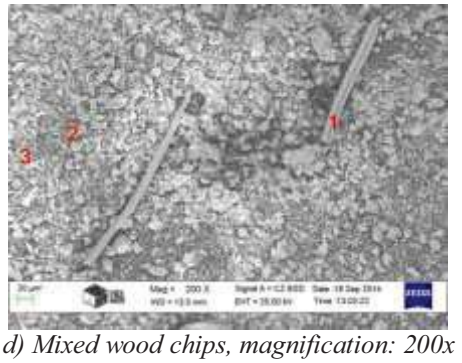

d) Mixed wood chips, magnification: 200x

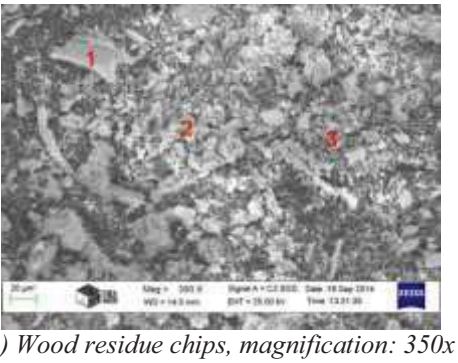

e) Wood residue chips, magnification: 350x

Figure 2. SEM image of ashes of wood chips

Extremely high carbon content can be observed in the high resolution fields (especially for wood residue chips), suggesting that the burning of carbon in the samples was incomplete. On the images presented in Figure 2, unburnt fibrous organic particles are clearly identifiable. The sampled ash is mostly made up of Ca- and Mg-based compounds (most likely oxides), with insignificant amounts of Si, except in the wood residue chips. Remarkable is the range of Ca in the ashes, from 20% m/m in the wood residue chips to more than 47% m/m in the mixed wood chips. Mention should be made of the relatively high K content, which is unevenly distributed as seen in the high resolution fields. More

than 2% m/m S is seen at Point 2 of the Hardwood #2 sample, and 1.28% m/m of S is detectable in the average spectrum.

Table 4

Semi-quantitative analysis of ashes of wood chips

Ashes of wood chips	Elements (% m/m)											
	C	O	Na	Mg	Al	Si	P	S	K	Ca	Mn	Fe
Pine average	**11.27**	**37.08**	**–**	**8.58**	**1.21**	**2.57**	**2.02**	**1.23**	**6.42**	**28.08**	**0.86**	**0.69**
Pine, point 1	33.10	30.35	–	3.20	0.63	0.69	0.87	0.53	24.00	6.01	0.32	0.30
Pine, point 2	5.35	39.36	–	8.78	1.61	4.03	3.21	0.76	5.60	27.52	0.88	1.01
Pine, point 3	3.32	27.31	0.81	14.81	1.15	2.63	7.55	1.34	16.98	21.87	1.10	1.11
Hardwood #1 average	**10.46**	**38.46**	**–**	**2.65**	**1.47**	**3.53**	**1.66**	**0.88**	**7.28**	**30.46**	**2.23**	**0.93**
Hardwood #1, point 1	7.46	34.66	–	0.88	0.76	1.31	0.96	0.46	1.48	50.85	0.66	0.52
Hardwood #1, point 2	4.89	24.16	–	1.57	3.28	33.55	1.86	0.92	12.56	11.9	2.67	2.64
Hardwood #2 average	**15.71**	**39.99**	**–**	**3.05**	**0.77**	**1.22**	**1.49**	**1.28**	**8.70**	**27.77**	**–**	**–**
Hardwood #2, point 1	3.58	30.43	–	0.67	8.84	31.43	0.07	0.00	6.72	18.25	–	–
Hardwood #2, point 2	8.76	40.73	–	2.04	0.53	1.03	0.73	0.59	5.68	39.89	–	–
Hardwood #2, point 3	5.98	29.45	–	2.93	0.69	0.88	1.59	2.13	16.40	39.94	–	–
Mixed wood chips, average	**7.32**	**21.52**	**–**	**2.91**	**0.53**	**1.25**	**3.31**	**1.15**	**14.23**	**47.79**	**–**	**–**
Mixed wood chips, point 1	11.80	39.59	–	2.41	0.47	0.61	0.76	0.48	3.25	40.63	–	–
Mixed wood chips, point 2	11.26	43.35	–	1.43	0.89	0.91	0.99	0.57	1.04	39.56	–	–
Mixed wood chips, point 3	11.24	41.94	–	2.11	0.41	0.59	1.28	0.59	8.89	32.94	–	–
Wood residue chips, average	**21.49**	**36.24**	**0.43**	**2.43**	**1.94**	**6.40**	**1.92**	**0.76**	**6.82**	**20.28**	**–**	**1.29**
Wood residue chips, point 1	12.32	46.48	0.31	5.53	0.35	1.18	1.19	0.59	4.25	27.42	–	0.37
Wood residue chips, point 2	8.33	38.41	0.71	1.50	0.72	1.06	1.49	0.67	2.16	44.60	–	0.35
Wood residue chips, point 3	16.25	33.56	0.81	3.95	3.16	6.75	4.03	0.86	10.08	14.88	–	1.85

Further on, we are presenting the SEM images of slags (Figure 3.) as well as their average composition and the composition of their individual points specifically (Table 5).

a) Glassy slag, magnification: 20x

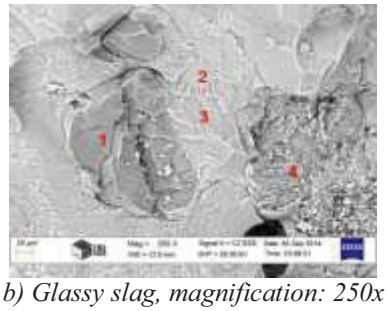

b) Glassy slag, magnification: 250x

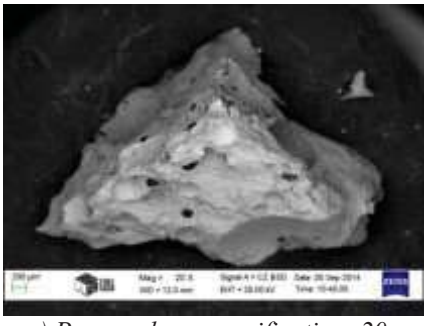

c) Porous slag, magnification: 20x

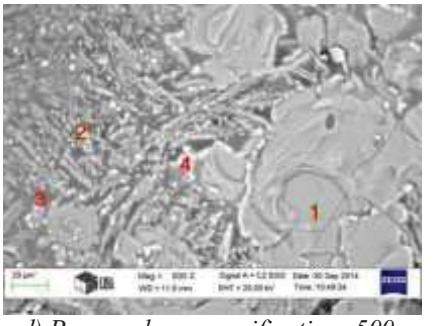

d) Porous slag, magnification: 500x

Figure 3. SEM image of slags

Table 5

Semi-quantitative analysis of slags

Slags	Elements (% m/m)												
	C	O	Na	Mg	Al	Si	P	S	K	Cl	Ca	Mn	Fe
Glassy slag, average	**4.51**	**29.46**	**0.67**	**0.92**	**2.70**	**36.21**	**0.53**	**–**	**4.31**	**18.61**	**0.36**	**1.35**	**0.36**
Glassy slag, point 1	1.35	41.26	0.08	0.11	0.40	56.41	0.00	–	0.07	0.04	0.07	0.13	0.09
Glassy slag, point 2	2.24	30.36	0.72	0.42	3.01	36.30	0.35	–	4.18	21.24	0.17	0.84	0.17
Glassy slag, point 3	2.77	32.98	0.66	1.65	3.04	36.47	0.40	–	4.19	15.98	0.36,	1.24	0.26
Glassy slag, point 4	2.54	42.86	0.00	0.10	0.36	53.63	0.05	–	0.08	0.08	0.09	0.13	0.07
Porous slag, average	**21.04**	**26.78**	**0.62**	**2.00**	**2.87**	**23.70**	**1.04**	**–**	**2.27**	**16.90**	**0.56**	**1.88**	**0.34**
Porous slag, point 1	3.17	23.57	0.04	0.08	0.34	29.59	0.07	–	0.08	42.87	0.05	0.14	0.00
Porous slag, point 2	1.94	22.60	0.28	2.14	2.54	32.68	0.00	–	3.43	29.98	1.72	2.19	0.50
Porous slag, point 3	23.74	29.46	1.13	0.10	6.20	29.91	0.41	–	5.52	1.80	0.07	1.26	0.40
Porous slag, point 4	4.65	19.58	0.82	1.23	1.90	13.87	14.21	–	1.35	39.95	1.06	1.16	0.22

Some C is still observable in the as-received slag samples (from the upper chamber wall), and though present, the amount of K is significantly lower than in the ash samples. The difference in the Si content – several times higher in slags than in the ashes – is critical; as is the reduced Ca and negligible S content. Another important difference can be seen when comparing different slag samples; there is considerably more C and proportionally lower amounts of Si and Ca in the porous slag.

Conclusion

The composition and contamination of the biomass fuel largely affects the amount and characteristics of the slagsdeposited on the boiler wall. When wood chips are used as feedstock,the origin of the wood may be of importance, since soil quality may vary substantially, depending on where the wood is transported from.Site-specific weather conditions, particularly the timing and amount of precipitation, largelyaffect the bioabsorption of mineral components in ligneaous biomass (which is of interest if the fuel is harvested in the rainy season). Resin content – typically high in coniferous species – must also be considered, since resin becomes plastic at high temperatures and adheres well to ash. Moreover, harvested trees easily get contaminated during storage, loading and

transport.The dust, sand or soil particles that, due to environmental effects, get stuck on surface of the woodchips, are fed into the combustion chamber along with the fuel.

In order to restrain ash melts formation and slagging in the biomass heating plant under study, an opening was cut into the vault between the lower and the upper chamber. Thus, primary air was let into the upper chamber, creating a turbulence in the corner of the upper chamber. This helped to prevent the formation of further depositionsand contributed to the elimination of the slags already there. Under the effect of turbulent air, the deposit broke up and dropped(piece by piece) by its tare weight, falling through the hole onto the movig grate which took it away it from the combustion chamber. This operation greatly improved the situation and reduced excess slag formation,although it did not eliminate the causes of slag formation. A further benefit of this technical solution was the ease of removal of slags from the secondary chamber during scheduled maintenance work, since the deposits could be broken up through the hole.

The primary aim of our research was to find out the correlations between slag formation and the fuels used. It is impossible to declare with absolute confidence, which fuel was actually used when the depositions were formed, given the tiny area of the slag samples detected and analysed by electron microscope. The amounts of the respective components, however, are indicative. The examination results have revealed that the softening parameters of the ash and slag samples do not justify ash fusion at normal operational temperature. It can thus be assumed that multi-component eutectics get formed, with a melting point corresponding to the actual temperature values at certain points in the chambers. Due to the boiler structure, no temperature measurement can be conducted in the vicinity of slag formation sites. The large amounts of CaO in the ash and the slags tend to have a fluidizing effect on the compounds present in aluminium silicate systems, such as the chamotte wall of the boiler. None of the numerous ternary eutecticsandternary compounds in the CaO-Al_2O_3-SiO_2three-component system hasa melting point higher than 1400 °C, indeed, the melting point of some eutectics is slightly higher than 1000 °C. Under the effect of CaO, chamotte bricks generally produce low-mullite pure glass slags – exactly like the depositions formed in the ‘Kenderföld’ boiler. Normally, reaction products would quickly flow down the wall due to low viscosity. However in the respective boiler,there was physically no room for that until the opening was cut into the vault, which finally lead to the accumulation of these at the deposition sites and consequently to the dramatic reduction of the cross-section of the flue gas flow. Considering refractory applications of chamotte construction bricks, CaO-Al_2O_3-SiO_2 ternary systems are not recommendedto beused at temperatures higher than 1170 °C. The question then arises: what temperatures actually prevail around the opening in the vault? The answer may lie in the composition of the slags.

The most important difference between the two slag types examined was the difference in the amount of the C content. The question arises: how could so much carbon get into the spongy, porous slag? Presumably, due to specific flow conditions during boiler operation, lighter fractions of the wood chips were transported from the lower into the upper chamber without having undergone complete burning. As it is known from operational experience, “ultra lightweight” fuel fractions are undesireable, for these can easily be carried off by the air draught of the boiler. In our case, the burning of the high-carbon solidsin the upper chamber might have causedsignificant temperature rise, leading to the formation and melting of the above mentioned multi-component eutectics.The process might have been buffered by the presence of alkaline oxides which are known to facilitate the formation of eutectics even with lower melting points. The presence of carbon would explain for porous

slag structure. Whenpart of the C content is burnt, the gaseous components of the combustion products get discharged and leave holes behind in the slag.

A slight lowering in the operating temperature might as well contribute to the prevention of slag formation (slag components are less likely to melt at lower T), with no significant effect on boiler efficiency.This measure has been proposed and implementdrecently, and owing to the opening cut into the vault as well as stable fuel quality, problems with slag formation seem to have been resolved.

For the proper mapping of temperature conditions, the installation of further sensors is recommended that be at least at places where slag formation is critical.

As part of ongoing research, EDS results will be complemented with XRF (X-ray fluorescence) analysis of the slag samples so that we can obtain more precise information on elemental composition and microstructure.

Acknowledgement

This research was carried out in the framework of the Center of Excellence of Sustainable Resource Management at the University of Miskolc.

References

[1] LUND, H.–WERNER, S.–WILTSHIRE, R.–SVENDSEN, S.–THORSEN, J. E.–HVELPLUND, F.–MATHIESEN, B. V.: 4th Generation District Heating (4GDH) Integrating smart thermal grids into future sustainable energy systems. *Energy,* 68, 2014, 1–11.

[2] DINCER, I.–ROSEN, M. A.: *Exergy: energy, environment and sustainable development.* 2nd ed. Elsevier, Oxford, 2012.

[3] GOCHENOUR, C.: *District energy trends, issues, and opportunities: the role of the World Bank.* World Bank Publications; 2001.

[4] DIFS, K.–DANESTIG, M.–TRYGG, L.: Increased use of district heating in industrial processes e impacts on heat load duration. *Appl Energy,* 86, 2009, 2327–2334.

[5] LUND, H.–MÖLLER, B.–MATHIESEN, B. V.–DYRELUND, A.: The role of district heating in future renewable energy systems. *Energy,* 35, 2010, 1381–1390.

[6] PIROUTI, M.–BAGDANAVICIUS, A.–EKANAYAKE, J.–WU, J.–JENKINS, N.: Energy consumption and economic analyses of a district heating network. *Energy,* 57, 2013, 149–159.

[7] LUCIA, L. Di–ERICSSON, K.: Low-carbon district heating in Sweden – Examining a successful energy transition. *Energy Research & Social Science,* 4, 2014, 10–20.

[8] GEBREMEDHIN, A.: Optimal utilisation of heat demand in district heating system – A case study. *Renewable and Sustainable Energy Reviews,* 30, 2014, 230–236.

[9] OPENSHAW, K.: Biomass energy: Employment generation and its contribution to poverty alleviation. *Biomass and Bioenergy,* 34, 2010, 365–378.

[10] AKHTARI, S.–SOWLATI, T.–DAY, K.: Economic feasibility of utilizing forest biomass in district energy systems – A review. *Renewable and Sustainable Energy Reviews,* 33, 2014, 117–127.

[11] ALLEN, J.–BROWNE, M.–HUNTER, A.–BOYD, J.–PALMER, H.: Logistics management and costs of biomass fuel supply. *International Journal of Physical Distribution & Logistics Management,* 28 (6), 1998, 463–477.

[12] DORNBURG, V.–FAAIJ, A. P. C.: Efficiency and economy of wood-fired biomass energy systems in relation to scale regarding heat and power generation using combustion and gasification technologies. *Biomass and Bioenergy,* 21, 2001, 91–108.

[13] CAPUTO, A. C.–PALUMBO, M.–PELAGAGGE, P. M.–SCACCHIA, F.: Economics of biomass energy utilization in combustion and gasification plants: effects of logistic variables. *Biomass and Bioenergy,* 28, 2005, 35–51.

[14] TEIXEIRA, P.–LOPES, H.–GULYURTLU, I.–LAPA, N.–ABELHA, P.: Evaluation of slagging and fouling tendency during biomass co-firing with coal in a fluidized bed. *Biomass and Bioenergy,* 39, 2012, 192–203.

[15] VAMVUKA, D.–KAKARAS, E.: Ash properties and environmental impact of various biomass and coal fuels and their blends. *Fuel Processing Technology,* 92, 2011, 570–581.

[16] VASSILEV, S. V.–BAXTER, D.–ANDERSEN, L. K.–VASSILEVA, C. G.: An overview of the composition and application of biomass ash. Part 1. Phase–mineral and chemical composition and classification. *Fuel,* 105, 2013, 40–76.

[17] VASSILEV, S. V.–BAXTER, D.–ANDERSEN, L. K.–VASSILEVA, C. G.: An overview of the composition and application of biomass ash. Part 2. Potential utilisation, technological and ecological advantages and challenges. *Fuel,* 105, 2013, 19–39.

Secreteriat of the Vice-Rector for Research and International Relations,
University of Miskolc,
Responsible for the Publication: Prof. Dr. Tamás Kékesi
Published by the Miskolc University Press under leadership of Attila Szendi
Responsible for duplication: Works manager: Erzsébet Pásztor
Number of copies printed: 200
Put the Press in 2015
Number of permission: TNRT–2015–219–ME